Dynamics of Nanoparticles in Mesogenic Solvents

by

Daniel A. Abras

A dissertation submitted in partial fulfillment

of the requirements for the degree of

Doctor of Philosophy

(Chemical Engineering)

at the

UNIVERSITY OF WISCONSIN - MADISON

2015

Date of final oral examination: 10/27/2015

The dissertation is approved by the following members of the Final Oral Committee:

Nicholas L. Abbott, Professor, Chemical Engineering
Daniel J. Klingenberg, Professor, Chemical Engineering
Michael D. Graham, Professor, Chemical Engineering
George W. Huber, Professor, Chemical Engineering
Saverio E. Spagnolie, Assistant Professor, Math

Dynamics of Nanoparticles in Mesogenic Solvents

Daniel Abras

under the Supervision of Professor Nicholas L. Abbott

at the University of Wisconsin – Madison

Many physical and chemical phenomena are influenced by the ways in which solvent molecules organize themselves near nanoscopic and microscopic interfaces. Although solvation of interfaces underlies a wide range of equilibrium and dynamic properties of materials, existing methods that permit tuning of solvation generally require either the additional of solutes or changes in temperature. The research presented in this thesis explores the structuring of mesogenic solvents in both a nematic liquid crystalline phase and an isotropic phase around nanoparticles. Nematic liquid crystalline phases possess long-range orientational order which is sensitive to the anchoring conditions of contacting surfaces. The long-range order is lost when heated into the isotropic phase, but can be regained by the application of external fields (*e.g.* electric and magnetic). As a first step towards studying the structure of mesogens around microscopic and nanoscopic surfaces, single-particle tracking was used to measure the hydrodynamic properties of chemically functionalized microparticles and nanoparticles when dispersed in nematic phases and when absorbed to interfaces between a mesogenic oil and an aqueous phase. During these initial measurements, we made the surprising observation that gold nanoparticles exhibited very large hydrodynamic sizes at interfaces of mesogenic oils in their isotropic phases. This result suggested that the meosgen was ordered around the nanoparticles even though the bulk of the oil was in a disordered phase. As a next step, we sought to determine the origins of the surprisingly large hydrodynamic sizes of the gold nanoparticles when dispersed in the isotropic phase of mesogenic solvents. Our results are consistent with the hypothesis that

electric fields associated with optically excited hot electron-hole pairs result in the formation of an ordered solvent corona. Overall, the principles identified in this thesis hint at general methods for achieving control over the structure of solvent around microparticles and nanoparticles dispersed in mesogenic solvents.

Acknowledgements

I would like to acknowledge the people who helped me throughout my many years of graduate school at the University of Wisconsin - Madison. First, I would like to acknowledge my advisor, Professor Nicholas L. Abbott, for guiding me in my PhD thesis work. Professor Abbott is excellent at teaching students how to critically evaluate and present experimental results. I would also like to thank my previous advisors, Professor Juan J. de Pablo and Professor David C. Schwartz. Even though I did not complete this thesis under their direction, the principles I learned for the design and execution of experiments was helpful. I would also like to thank current and former members of the Abbott group and former members of the de Pablo and Schwartz groups. In particular, I would like to recognize Kristy Kounovsky - Shafer, Gus Potamousis, Michael Bechner, Kyubong Jo, De-Wei Yin, Juan Pablo Hernandez-Ortiz, Edward Sambriski, Gary Koenig, Emre Bukusoglu, Reza Abbasi, and Chenxuan Wang. Finally, I would like to thank my family and friends for their support throughout my PhD experience.

Table of Contents

Abstract i

Acknowledgements iii

Table of Contents iv

List of Figures vi

Chapter 1 Introduction and Background Information

1.1 Introduction....1

1.2 Background Information....3

1.3 References....15

Chapter 2 Thesis Overview

Thesis Overview....19

2.1 References....23

Chapter 3 The Mobilities of Micro- and Nano-Particles at Interfaces of Nematic Liquid Crystals

3.1 Abstract....24

3.2 Introduction....25

3.3 Materials and Methods....28

3.4 Results....31

3.5 Discussion....57

3.6 References....59

Chapter 4 Optically-Excited Changes in Nanoparticle Solvation

4.1 Abstract....64

4.2 Introduction....65

4.3 Results....66

4.4 Discussion 87

4.5 Materials and Methods 88

4.6 Additional Measurements of Nanoparticle Mobility 94

4.7 Additional Experimental Considerations Related to Single Particle Tracking of Gold Nanoparticles 99

4.8 Discussion of the Role of Electric Fields Generated by Local Surface Plasmon Resonances on the Hydrodynamic Size of Gold Nanoparticles 101

4.9 Additional Discussion of the Role of Electric Fields Associated with the Separation of Hot Electrons and Holes 109

4.10 References 117

Chapter 5 Influence of Size and Surface Chemistry on the Mobility of Nanoparticles Dispersed in Nematic Liquid Crystals

5.1 Abstract 121

5.2 Introduction 122

5.3 Materials and Methods 127

5.4 Results 142

5.5 Discussion 136

5.6 References 146

Chapter 6 Conclusions and Closing Remarks

Conclusions and Closing Remarks 147

6.1 References 150

Appendix A 151

Appendix B 152

List of Figures

Figure 1 - 1. (a) Schematic illustration of nematic and isotropic phases. When the temperature of a nematic phase is increased above T_{NI}, a phase transition occurs to a disordered isotropic phase. (b) In this thesis, we utilize the mesogens 5CB (T_{NI} = 35˚C) and MBBA (T_{NI} = 42˚C). 4

Figure 1 - 2. Schematic illustration of the (a) dipolar and (b) quadrupolar oscillatory modes of LSPR in a spherical metal particle. The electrons in the conduction band of metal particles (grey) oscillate with respect to the particle in response to an applied electric field of a specific resonant frequency. For gold nanoparticles, the resonant frequencies occur in the visible range of the light spectrum. 6

Figure 1 - 3. Director field profiles for particles dispersed in LCs with surfaces which give rise to strong perpendicular anchoring (hedgehog defect) (a), weak perpendicular anchoring (Saturn ring defect) (b), and planar anchoring (boojum defect) of the LC.....10

Figure 1 - 4. Relative orientations of the LC director and the shear direction that define the Miesowicz viscosities: (a) ν_c, (b) ν_a, and (c) ν_b. 12

Figure 3 - 1. Polarized light micrographs of DMOAP-functionalized silica particles (diameters of 2.3 ± 0.2 μm) at a nematic 5CB–aqueous interface. The aqueous phase contained 0.1 M sodium perchlorate, which causes planar anchoring of 5CB at the aqueous interface. Note that the bottom substrate is functionalized with DMOAP, which causes homeotropic anchoring of the LC and thus facilitates imaging of the defect. The homeotropic anchoring gives rise to hedgehog defects that appear brighter than the surrounding medium in brightfield micrographs due to a uniform tilt angle of the LC director below the defect. (a) Crossed polars and (b) bright-field imaging of a particle with a hyperbolic hedgehog defect. The orientations of the analyzer (A) and polarizer (P) are shown. (c) Schematic illustration of top and (d) side view of the LC director for a particle with a hyperbolic hedgehog defect at the aqueous–LC interface, as shown in A and B. (e) Polarized light micrograph (crossed polars) of a particle at the aqueous–LC interface that when dispersed in bulk LC produced a Saturn ring defect. 32

Figure 3 - 2. Mean squared displacement (MSD) of a single DMOAP-functionalized particle (diameter of 2.3 ± 0.2 μm) at a 5CB–aqueous interface, plotted as a function of time, at either (a) 40 °C or (b) 26 °C. At 26 °C, the nematic LC was anchored parallel to the aqueous interface. A particle trajectory is shown as an inset in each plot. Solid lines indicate a least squares fit to the MSD data. 35

Figure 3 - 3. Diffusion coefficients for DMOAP-functionalized silica particles (diameters of 2.3 ± 0.2 μm), measured at either 26°C or 40°C, at a 5CB–aqueous interface with planar anchoring. Results are reported for diffusion along the far-field director (*x*-axis) and perpendicular to the far-field director (*y*-axis). (a) Data for particles that exhibited hyperbolic hedgehog defects in bulk 5CB. (b) Data for particles that exhibited Saturn ring defects in bulk 5CB. The black, horizontal lines indicate values of diffusion coefficients of 2.3 μm particles in

bulk 5CB, as calculated either using apparent viscosities reported by Stark and coworkers at 26°C (54) or an experimentally measured apparent viscosity of 22 mPa.s at 40°C. 38

Figure 3 - 4. Influence of particle size on the apparent viscosity of either gold nanoparticles (141 ± 11 nm in diameter) or silica microparticles (2.3 ± 0.2 μm in diameter) at a 5CB–aqueous interface with planar anchoring of the LC. The gold particles were functionalized with mixed monolayers of alkanethiols and the silica particles were functionalized with DMOAP (see text for details). 40

Figure 3 - 5. Influence of chemical functionality of gold nanoparticles on bulk and interfacial diffusion. The nanoparticles were functionalized with either a mixed monolayer of decanethiol and hexadecanethiol (C10/C16), or a monolayer formed from decanethiol (C10). The vertical bars indicate interfacial diffusion coefficients. The horizontal lines indicate diffusion coefficients measured in bulk 5CB, as reported by Koenig *et al.* 49

Figure 3 - 6. Comparison of bulk or interfacial apparent viscosities of gold nanoparticles (diameters of 169 ± 12 nm and 141 ± 11 nm, respectively) functionalized with mixed or single component monolayers. The interfacial diffusion coefficients were measured at a nematic 5CB–aqueous interface with homeotropic anchoring (at 26°C). The bulk diffusion coefficients from Koenig *et al.* were measured for displacements perpendicular to the far-field director (at 26°C).53

Figure 4 - 1. Schematic illustration of experimental setup. (a) Scanning electron micrographs of gold nanoparticles with diameters of 164±11nm or (b) 85±7 nm. (c) Normalized histogram of diameters of 400 nanoparticles with average sizes of either (solid line) 164±11 nm or (dotted line) 85±7 nm. Molecular structures of oils used in this study: (d) 5CB and (e) MBBA. Schematic illustration of monolayers formed on the surfaces of gold nanoparticles from (f) C10SH and C16SH or (g) C10SH. (h) and (i) show schematic illustrations of the illumination of gold nanoparticles. At a temperature 1˚C above the T_{NI}, when illuminated with a 650±20 nm light source (h), the gold nanoparticles diffuse with a hydrodynamic size approximately equal to their physical size. When illuminated with a 450±20 nm light (i), the gold particles diffuse with a hydrodynamic size that is 40 nm larger than their physical size. 67

Figure 4 - 2. Measurements of hydrodynamic sizes of gold nanoparticles. (a) Representative trajectories of single gold nanoparticles (gold core diameter of 164±11 nm; surfaces functionalized with a mixed monolayer of decanethiol and hexadecane thiol) tracked at either (blue) 36˚C (1˚C above T_{NI}) or (red) 44˚C (9˚C above T_{NI}) over a duration of 180 s. (b) Mean squared displacement (MSD) versus time delay for trajectories shown in (a). A linear least-squares fit (solid line) to the data is shown. (c) The difference between the hydrodynamic diameter, d, and physical diameter, d_0, of gold nanoparticles (d_0 = 164±11 nm) functionalized with a mixed component thiol monolayer (black) or a single component thiol monolayer (grey) at various temperatures above the bulk nematic-to-isotropic phase transition temperature of 5CB (T_{NI} = 35˚C). Hydrodynamic diameter measurements were obtained using 40-50 particle trajectories from 3 independent samples. Data show mean ± s.e.m. Lines are drawn to guide the eye. 68

Figure 4 - 3. Difference between the hydrodynamic diameter, d, and physical diameter, d_0, of gold nanoparticles with (a) d_0 = 164±11 nm and (b) d_0 = 85±7 nm, when illuminated with either a blue, green, or red light source, as represented by the color of the bars at various temperatures above the bulk clearing temperature of 5CB, T_{NI} (35˚C). Hydrodynamic diameters were measured using 40-50 particle trajectories obtained from 3 independent samples. Data show mean ± s.e.m. 70

Figure 4 - 4: Calculations and measurements of the optical properties of gold nanoparticles. (a) The calculated extinction (solid line) and absorption (dashed) efficiencies of (black) 164 nm and (grey) 85 nm diameter gold particles in a medium of refractive index 1.39, the isotropic refractive index of 5CB at the bulk clearing temperature. The blue, green, and red bars indicate the range of wavelengths of light transmitted though the bandpass filters used in our experiments. The width of the line represents the FWHM of the distribution of light transmitted by the filter. The calculated efficiency of excitation of hot electrons (dotted) by light is also plotted (See Section 4.9). (b) The measured extinction efficiency of (black) 164±11 nm-diameter and (grey) 85±7 nm-diameter gold nanoparticles with a mixed component thiol monolayer obtained. The extinction efficiency was calculated from optical density measurements performed in 95% 5CB - 5% ethanol using the method described by Fernig *et al.* (18). Optical density measurements are the average of 2 independent samples. (c-e) Cross-section of the electric field enhancement (E/E_i) at the resonance frequencies indicated by the arrows in (a). The light source is incident from the top of the image and is polarized in the plane of the page. The scale bar is 40 nm. The black circles are superimposed to indicate the location of the particle. (f-h) Electric field enhancement as a function of distance from the particle surface drawn perpendicular to the surface for the calculations shown in c-e, respectively. The black line indicates a trace that passes though the point of maximum electric field enhancement at the particle surface and is indicated by the black trace in c-e. The grey line passes though the point of minimum electric field enhancement at the particle surface and is indicated by the grey trace in c-e. Optical density measurements are the average of 2 independent samples. 73

Figure 4 - 5. Electric field enhancement near gold nanoparticles at various wavelengths of illumination. (a) Cross-section of local electric field enhancement (E/E_i) for 164 nm diameter gold particles illuminated by light with various wavelengths from 400 nm to 780 nm in a medium with refractive index 1.39. The scale bar is 40 nm. The black circles are superimposed to indicate the location of the particle. The light propagates from the top of each panel and is polarized in the direction of the page. (b) Peak value of the electric field enhancement calculated at the particle surface at various wavelengths from 400 nm to 800 nm. 75

Figure 4 - 6. Electric field enhancement near gold nanoparticles at various wavelengths. (a) Cross-section of local electric field enhancement (E/E_i) for 85 nm diameter gold particles illuminated by light with various wavelengths from 400 nm to 780 nm in a medium with refractive index 1.39. The scale bar is 40 nm. The black circles are superimposed to indicate the location of the particle. The light propagates from the top of each panel and is polarized in the direction of the page. (b) Peak value of the electric field enhancement calculated at the particle surface at various wavelengths from 400 nm to 800 nm. 76

Figure 4 - 7. Difference between the hydrodynamic radius, d, and physical radius, d_0, of 157±8 nm diameter silver nanoparticles illuminated with a blue or red light source as represented by the color of the data points at various temperatures above the bulk clearing temperature of 5CB, T_{NI} (35˚C). Each data point represents an ensemble of 50 particles. The error bar represents the standard error of the measurements. Hydrodynamic size measurements were obtained using 40-50 particle trajectories from 2 independent samples. Data show mean ± s.e.m. 81

Figure 4 - 8. Increase in hydrodynamic diameter ($d-d_0$) induced by the illumination of 164±11 nm gold particles with various intensities of blue light (black squares; left axis). The red line shows the prediction of a simple model for accumulation of hot electrons (right axis). Hydrodynamic size measurements were obtained using 40-50 particle trajectories. Data show mean ± s.e.m. 82

Figure 4 - 9. Influence of optically excited changes in solvation on plasmon resonances of gold nanoparticles (96±37 nm-diameter) functionalized with mixed monolayers supported on a glass surface. (a) Absorbance of a probe beam (P) of light by the gold nanoparticles in contact with isotropic 5CB at 37˚C. (b,c) WoMA of the sample in (a) with (P+E) or without (P) co-illumination of an excitation beam (E) of blue light at (b) 37˚C ($T - T_{NI} = 2$˚C) and (c) 44˚C ($T - T_{NI} = 9$˚C). The WoMA for each sample was measured before (left bar, P), during (center bar, P+E), or after (right bar, P) illumination with the excitation beam. Error bars represent the error in the mean of a Gaussian function fit to the data. 84

Figure 4 - 10. (a) Absorbance of a probe beam (P) of light by the gold nanoparticles in air at 37˚C. The curve is representative of an ensemble of similar measurements used in this study. (b) SEM measurements of the gold nanoparticles used in this study. The scale bar is 100 nm (c) WoMA of the sample in (a) with (P+E) or without (P) co-illumination of an excitation beam (E) of blue light at (b) 37˚C ($T - T_{NI} = 2$˚C) and (c) 44˚C ($T - T_{NI} = 9$˚C). The WoMA for each sample was measured before (left bar, P), during (center bar, P+E), or after (right bar, P) illumination with the excitation beam. Error bars represent the error in the mean of a Gaussian function fit to the data. 85

Figure 4 - 11. A comparison between measurements of the hydrodynamic sizes of 143±7 nm gold nanoparticles in MBBA (purple) and 164±11 nm gold particles in 5CB (yellow) with a mixed thiol monolayer and one degree above T_{NI} of each mesogen. Hydrodynamic size measurements were obtained using 40-50 particle trajectories from 3 independent samples. Data show mean ± s.e.m. 95

Figure 4 - 12. Hydrodynamic diameter (d) minus physical diameter (d_0) of 143±7 nm gold particles in the isotropic phase of *N*-(4-methoxybenzylidene)-4-butylaniline (MBBA) at temperatures relative to the bulk clearing temperature (T_{NI} = 42°C) for particles functionalized with a mixed thiol monolayer and measured with white light illumination. Hydrodynamic size measurements were obtained using 40-50 particle trajectories from 2 independent samples. Data show mean ± s.e.m. 96

Figure 4 - 13. A sphere with diameter d bisected by a plane (dotted line). The two surfaces of the sphere created separated by the plane have opposite surface charge densities ($\pm\sigma_0$). The two

charged surfaces create a dipole moment (**p**) and the electric field due to the charge dipole at some location **r** is **E**(r). 111

Figure 5 - 1. Diagram of various defect structures for micrometer-scaled particles. The far-field director is shown (right). (a) Hedgehog defect for strong, perpendicular anchoring of the liquid crystal at the particle surface. It is dipolar in nature and contains a single point defect. (b) Saturn ring defect for weak, perpendicular anchoring at the particle surface. The structure is quadrupolar in nature and contains a line disclination. (c) Boojum defect for planar anchoring of the liquid crystal at the particle surface. It is quadrupolar in nature and contains two point defects. 123

Figure 5 - 2. Experimental set-up for dark-field microscopy and single-particle tracking in nematic liquid crystals. 130

Figure 5 - 3. SEM micrographs of (a) 85±7 nm, (b) 140±11 nm, and (c) 239±18 nm gold nanoparticles. (d) 380±30 nm silica core gold shell nanoparticles. 133

Figure 5 - 4. (a) Representative mean squared displacements (MSD) of nanoparticles with mean diameters (red) 380±10 nm, (green) 239±18 nm, (blue) 140±11 nm, and (orange) 85±7 nm and single component monolayers with respect to delay time. For Brownian diffusion, the MSD with respect to time step to be linear. (b-e) trajectories corresponding to the MSD shown in (a). The scale bar is 2 μm. 136

Figure 5 - 5. Diffusion coefficient (a) and apparent viscosity (b) for gold nanopaticles with a mixed thiol monolayer (yellow) and single component monolayer (blue), and silica particles with a DMOAP monolayer (green) of various diameters in 5CB.....137

Figure 5 - 6. Apparent viscosity of 143±8 nm gold nanoparticles in nematic 5CB for diffusion perpendicular to the far-field director when illuminated with red (650 nm (FWHM = 40 nm)), green (550 nm (FWHM = 40 nm)), and blue (450 nm (FWHM = 40 nm)) light as indicated by the color of the bar. 144

Chapter 1

Introduction and Background Information

1.1 Introduction

This thesis furthers the understanding of the interactions between chemically functionalized surfaces of nanoparticles and liquid crystals (LC). In particular this thesis demonstrates principles for tuning LC ordering near nanoparticle surfaces using particle size, chemical functionality, and optically excited electric fields. These topics provide insight into the factors that control nanoparticle mobility and self-assembly in a liquid crystalline medium which may be relevant to a variety of applications, including the creation of materials with tunable optical, electronic, and mechanical properties, and the creation of sensors for the detection of chemical species.

The first study reported in this thesis describes the mobilities of microparticles and nanoparticles at the interfaces between an aqueous phase and nematic or isotropic oils. In this study, we observe an unexpectedly large hydrodynamic size for gold nanoparticles dispersed at the interfaces of a mesogenic solvents in an isotropic phase. The second study included in this thesis expands on our observations of gold nanoparticles in the isotropic phase of mesogenic solvents and reveals principals for optical control of the ordering of isotropic oils near nanoscopic surfaces at temperatures which place the oils near transition temperatures to ordered phases. We demonstrate optical control over the solvent structure near gold nanoparticles through measurements of both the hydrodynamic size and optical resonances. The third study in this thesis investigates the parameters, including the wavelength of an incident illumination, which affect the mobility of gold nanoparticles dispersed in a bulk nematic LC.

The remainder of this chapter presents background information for the body of work presented in this thesis. The background information is organized to three sections. The first section introduces liquid crystals and their anisotropic rheological and dielectric properties. The second section presents a brief introduction to metal nanoparticles, and in particular describes the optical properties of gold nanoparticles. The third section presents an overview of studies of particles dispersed in liquid crystals.

1.2 Background Information

Liquid Crystals

Liquid crystals are a phase of matter with properties of both a crystalline solid and an isotropic liquid. This thesis deals with nematic LCs which possess orientational order however flows like a liquid. A schematic illustration of nematic phases is provided in Figure 1-1a. The orientational order of nematic LCs is characterized by two parameters, a director and an order parameter. The director describes the average orientation of the individual molecules. The order parameter describes the average deviation of the orientation of the long axis of the individual molecules and the director. The order parameter of an isotropic medium is zero. In the experiments described by this thesis, we use the mesogens 4-pentyl-4'-cyanobiphenyl (5CB) and n-(4-methoxybenzylidene)-4-butylaniline (MBBA) (Figure 1-1b). In the bulk, 5CB and MBBA form a nematic phase from an isotropic phase when cooled below 35˚C and 42˚C (1, 2).

The experiments described in this thesis provide insights into LC ordering near the surfaces of metal nanoparticles through measurements of mobility and optical properties. Unlike microscale particles, the structure of the LC near nanoparticles cannot be directly imaged. LCs have anisotropic dielectric (3, 4) and rheological (5, 6) properties, so the refractive index and viscosity experienced by a particle dispersed in a LC depend on both the director and order parameter near the particle surface. The orientational order of LCs has previously been shown to depend on the chemical functionality of surfaces (7-11). In this thesis we investigate the effects of particle size, composition, and surface chemical functionality on the near surface orientational order of LCs.

The anisotropic dielectric properties of LCs also provide a means to actively and reversibly control the order parameter and director field. Previous studies have shown that the

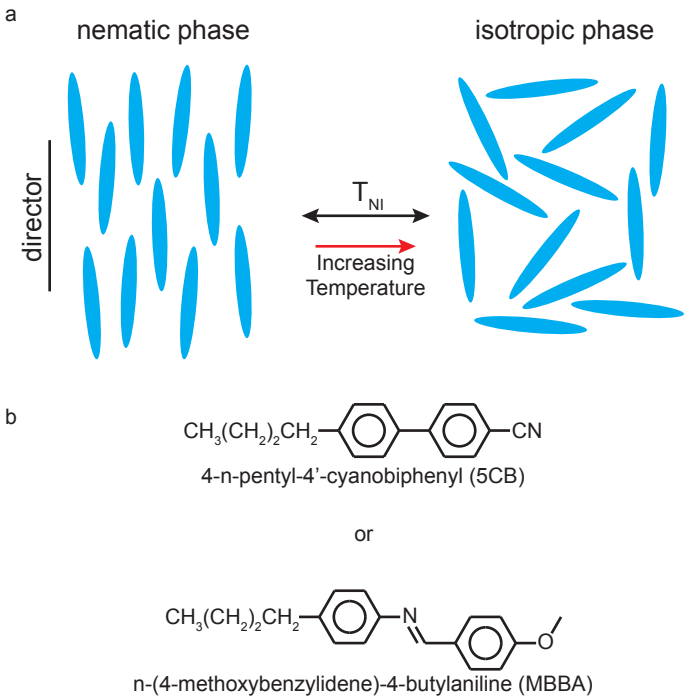


Figure 1 - 1. (a) Schematic illustration of nematic and isotropic phases. When the temperature of a nematic phase is increased above T_{NI}, a phase transition occurs to a disordered isotropic phase. (b) In this thesis, we utilize the mesogens 5CB (T_{NI} = 35˚C) and MBBA (T_{NI} = 42˚C).

director of LCs can be altered using electric (12) and magnetic fields (13, 14). The individual molecules of an LC will align with respect to the direction of the applied electric or magnetic field. Other studies have demonstrated that mesogens can form a nematic or para-nematic phase in response to an applied electric field at temperatures which place the medium in an isotropic state (15). In Chapter 4, we will discuss methods to optically generate electric fields in metal nanoparticles dispersed in an isotropic oil to form an ordered solvent corona.

Gold Nanoparticles

In this thesis, we utilize gold and silver nanoparticles which possess unique optical properties. Gold and silver nanoparticles can exhibit localized surface plasmon resonance (LSPR) when illuminated with certain wavelengths of light (16, 17). LSPR is a standing wave oscillation of the conduction electrons of the metal nanoparticle in response to an electromagnetic field of a specific (resonant) wavelength. Note that as particle size increases, a metal particle begins to exhibit multiple resonant modes. An illustration of the dipolar and quadrupolar modes is provided in Figure 1-2. The excitation of these resonant modes have several important properties which we will consider in this thesis. First, the resonance of the electron oscillation with this particular wavelength of light gives rise to a peak in the measured optical extinction (16, 17). Second, the excitation of an LSPR by light of its resonant wavelength gives rise to an enhancement of the electric field in the vicinity of the particle (18, 19). Third, the decay of an LSPR can proceed by several pathways. One important pathway we consider in this thesis is where the energy associated with LSPR excites a hot electron-hole pair (20, 21). The resonant wavelength of the LSPR of metal nanoparticles and the details of the above mentioned properties all depend on the composition, size, morphology, and surrounding dielectric environment of the nanoparticles (22-27).

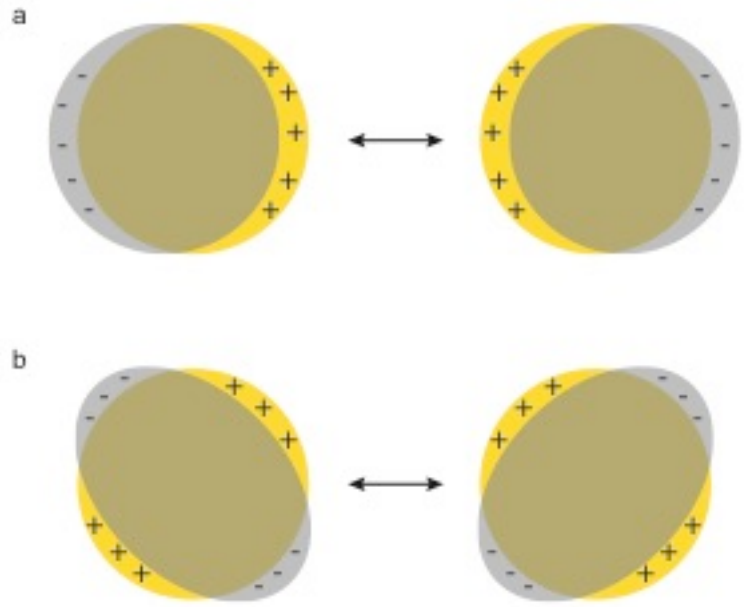


Figure 1 - 2. Schematic illustration of the (a) dipolar and (b) quadrupolar oscillatory modes of LSPR in a spherical metal particle. The electrons in the conduction band of metal particles (grey) oscillate with respect to the particle in response to an applied electric field of a specific resonant frequency. For gold nanoparticles, the resonant frequencies occur in the visible range of the light spectrum.

The measurement of the wavelength of maximum extinction of light is a simple method to probe the local dielectric environment of the nanoparticles. An increase in the refractive index surrounding the metal nanoparticle will give rise to a red shift in the wavelength of maximum absorption of light. The polarizability of the surrounding environment is increased with an increase in the refractive index resulting in a diminished restoring force of the excited electrons and a damping of the resonance. This has been previously shown as a facile method to probe the local structure of liquid crystalline materials near metal nanoparticle surfaces using UV-visible spectroscopy and has been shown to probe several tens of nanometers from the nanoparticle surface (28). In this thesis, we measure the optical density of gold nanoparticles to probe the ordering of the surrounding medium.

The excitation of LSPR will also enhance the electric field in the area surrounding the nanoparticle. The electric field intensity near an isolated nanoparticle when illuminated with light at the resonant wavelength can be up to 100 times (18, 29) the intensity of the incident light and is strongly dependent on nanoparticle size, composition, and morphology (22-27). Field enhancements become weaker as particle size increases (24). For non-spherical particles, the electric field enhancement is greater near the areas of the nanoparticles which exhibit a higher curvature (18, 24, 29). We predict that particles with a roughened surface or facets will have areas of higher field enhancement. When formed into ordered arrays, metal nanoparticles also exhibit large electric field enhancements at so-called hot spots between the nanoparticles (30). The electric field enhancement produced by nanoparticles organized into ordered arrarys has been demonstrated to be sufficiently strong to affect the structure of nematic LC films (31, 32). We consider in this thesis the possibility that the electric fields associated with the LSPR of isolated spherical particles affect the ordering of a surrounding polarizable medium.

The dephasing of LSPR can result in the generation of hot electron-hole pairs (20, 21). The optical excitation of hot elections in metals is not unique to nanoparticles or LSPR. Photons of light of sufficient energy (shorter wavelengths of light are composed of higher energy photons) are able to promote bound valance electrons into an unbound state in the conduction band (16, 17). In the conduction band, the negatively charged electron is free to diffuse within the particle. The excitation of the hot electron creates a positively charged hole whose mobility is much less than the electron (We calculate in Chapter 4 that a hot electron has a mobility 40 times greater than a hole in gold). The energy required to excite a hot electron-hole pair corresponds to the energy difference between the valance band and the conduction band in the metal. For the direct excitation of hot electrons in gold, the energy required is 2.4 eV (517 nm) (16). That is, light with a wavelength of 517 nm or lower will generate hot electron-hole pairs in gold. In contrast for silver, the required energy is 3.9 eV (318 nm) (16), which is in the ultraviolet range. In addition to the direct excitation process, the decay of LSPR will also result in the formation of hot electron-hole pairs. For gold nanoparticles, the decay of LSPR can result in the formation of hot electrons even if the resonant wavelength of light is greater than 517 nm because it is able to excite valence electrons which lie closer in energy to the conduction band (33). In this thesis, we will investigate these optically generated electric fields as a method to manipulate solvent structure around metal nanoparticles.

Particles in Liquid Crystals

When a spherical particle with defined surface anchoring is dispersed in LCs with a defined and uniform director field, the director is deformed to minimize the elastic energy of the LC and results in the formation of defects (34). Defects are regions of the LC where the director field is discontinuous and manifests as an area of local melting of the LC. There are two types of

defects: point defects which are points where the director cannot be determined and line defects which are lines along which the director cannot be determined. Strong homeotropic (perpendicular with respect to the surface) anchoring at the surface of the particle results in a so called hedgehog defect which has dipolar symmetry (Figure 1-3a). Weak homeotropic anchoring at the surface of the particle results in so-called Saturn ring defect (Figure 1-3b) which has quadrupolar symmetry. In contrast, when the chemistry of the surface of the particle gives rise to planar anchoring of the LC, two boojum defects (Figure 1-3c) result which has quadrupolar symmetry. The director configurations listed here can be measured directly on micrometer-sized particles using bright-field microscopy but cannot be viewed directly on nanometer-sized particles. Additional methods must be applied to infer the director configuration around nanoparticles such as measurements of the pairwise interactions and mobility of the particles.

It has previously been demonstrated that these defects which result from the director field around particles lead to attractive pairwise interactions. Defects have a large energy penalty associated with their formation and interact to minimize the free energy of the LC. Previous studies have shown that hedgehog and Saturn ring defects formed in the medium surrounding micrometer-sized particles result in the particles assembling into chains (35-37) and two-dimensional arrays (36). The energy of the interaction between micrometer-sized particles and a hedgehog or Saturn ring defect structure is very strong (~10^3 kT) (38, 39) and results in the irreversible formation of particle assemblies. Nanoparticles with diameters of the order of ~100 nm and functionalized with surfaces which give rise to homeotropic anchoring of the LC however do not arrange into irreversible assemblies because the interaction energy is small (~kT) (40). The interaction energy observed between these nanopararticles contrasts predictions for the pairwise interaction energies of ~10^2 kT for nanoparticles with hedgehog or

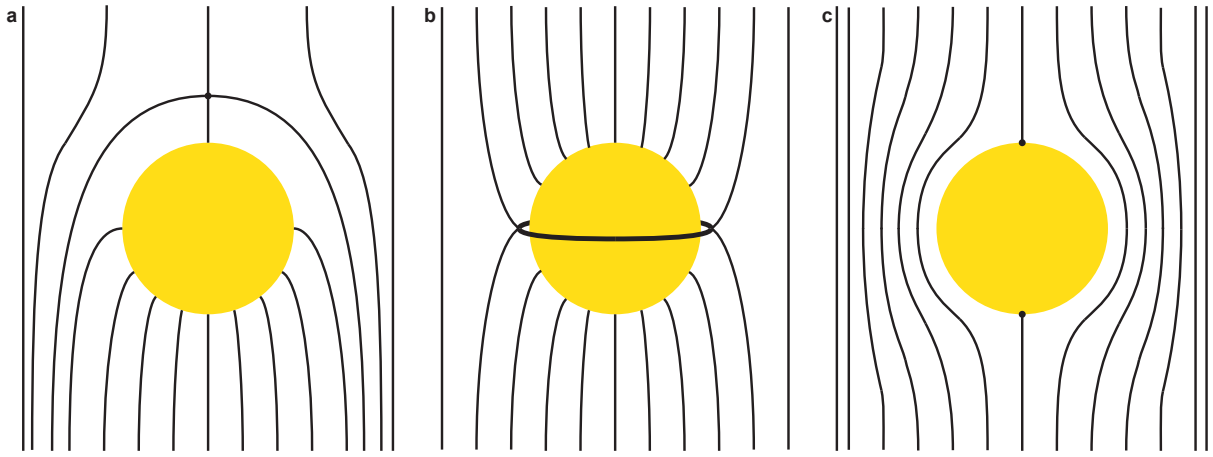


Figure 1 - 3. Director field profiles for particles dispersed in LCs with surfaces which give rise to strong perpendicular anchoring (hedgehog defect) (a), weak perpendicular anchoring (Saturn ring defect) (b), and planar anchoring (boojum defect) of the LC.

Saturn ring defects (38, 39). In contrast to micrometer-sized particles, the director configuration around nanometer-sized particles cannot be directly observed with bright-field microscopy; however, the weak interaction energy between pairs of nanoparticles is evidence that the director configuration around nanometer-sized particles is different from the director configuration around micrometer-sized particles.

Additional evidence which suggests that the director configurations near nanoparticle surfaces is different from the director configurations observed for microparticles can be found from measurements of particle mobility. As mentioned previously, the mobility of micrometer-sized and nanometer-sized particles is impacted by the director configuration around the particles due to the anisotropic rheological properties of the LC molecules. As an example, for 5CB, there are three Miesowicz viscosities: 129.6 mPa.s, 37.4 mPa.s, and 22.9 mPa.s (5). The largest of these viscosities (ν_c) corresponds to a sheer flow with the velocity perpendicular to the director (Figure 1-4a). The intermediate viscosity (ν_a) corresponds to a shear direction perpendicular to a uniform director field. The smallest of these viscosities (ν_b) corresponds to a sheer direction parallel to the director. A in illustration of the relative orientations of the LC director and the shear that thefin Measurements of the mobilities of 169±16 nm diameter gold nanoparticles dispersed in 5CB show that particles have an apparent viscosity of 58.9±7.2 mPa.s when functionalized with a surface which gives rise to perpendicular anchoring of the LC and 39.2±3.1 mPa.s when functionalized with a monolayer which gives rise to planar anchoring of the LC (41). As a comparison, a 1.1 μm diameter silicon oil droplet in 5CB with a Saturn ring defect was measured to have an apparent viscosity of 82.6 mPa.s (42) which is similar to the predicted value of 85.3 mPa.s (5). Based on these results we make two observations: First, the apparent viscosity of the nanoparticles with a surface chemistry which gives rise to homeotropic

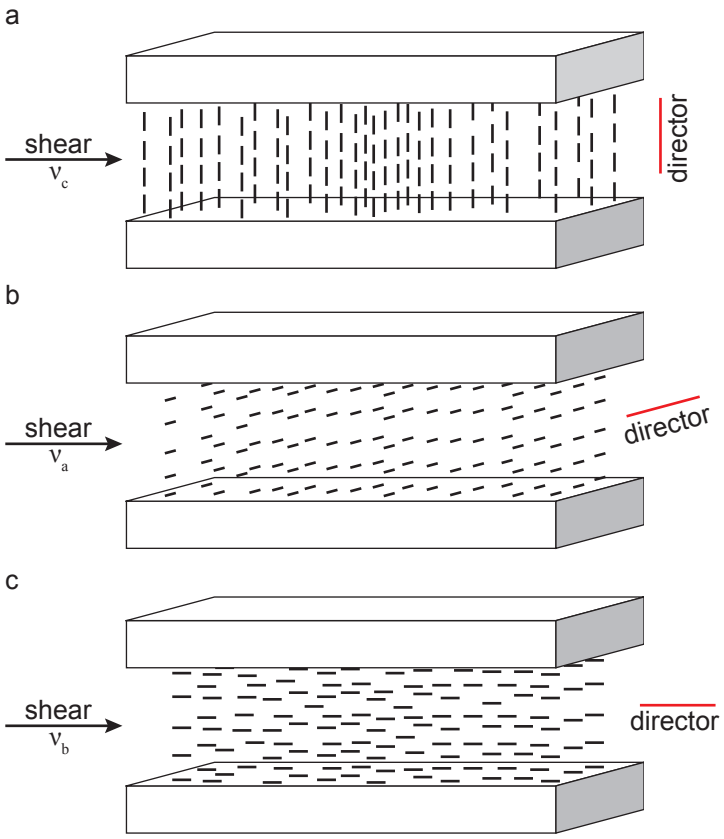


Figure 1 - 4. Relative orientations of the LC director and the shear direction that define the Miesowicz viscosities: (a) ν_c, (b) ν_a, and (c) ν_b.

alignment of the LC is smaller apparent viscosity in 5CB than the microparticles with the Saturn ring defect. This hints at the possibility of a size-dependent change in the near surface order of the LC as the particle size decreases from the microscale to the nanoscale. Second, the surface chemistry of the nanoparticles can change in the ordering of the surrounding LC which shows that the director field of the LC is still distorted by the addition of the nanoparticle. In Chapter 3 and Chapter 5, we will investigate in greater detail the mobilties of microparticles and nanoparticles dispersed in LC.

Finally, we comment that the above studies have also reported that the mobilties of gold nanoparticles dispersed in 5CB after the temperature has increased above the bulk clearing temperature (above 35˚C) are unexpectedly small. Specifically, the hydrodynamic diameter of the gold nanoparticles with the surface chemistry which causes homeotropic anchoring of the LC is 60 nm larger at 40˚C (5˚C above the bulk clearing temperature) than the physical diameter of the particles (41). The authors speculate that the unexpectedly large hydrodynamic size of the particles is due to the presence of an ordered layer of 5CB at the particle surface under conditions which place the bulk of the LC in a disordered isotropic state. The existence of ordered layers of LCs at surfaces in the isotropic phases of liquid crystals have been reported previously (43-45). The presence of a surface-induced nematic wetting layer (prenematic wetting layer) at surfaces in contact with 5CB 1-2˚C above the bulk clearing temperature has been reported, however, the thicknesses of these ordered layers are 2-3 nm (43, 44) which does not account for the large increase in hydrodynamic diameter of gold particles mentioned above. We predict that the nematic coherence length would limit the thickness of a surface-induced prenematic wetting layer and, for 5CB at 40˚C, the nematic coherence length is 4 nm (46). In Chapter 3, we also report the abnormally large hydrodynamic sizes of nanoparticles at aqueous-

5CB interfaces 5˚C above the bulk clearing temperatures. In Chapter 4, we investigate this observation in greater detail and provide evidence that the large hydrodynamic size of the nanoparticles is due to the ordering of the isotropic 5CB by an electric field associated with the presence of optically excited hot electron-hole pairs.

1.3 References

1. Li J, Gauza S, & Wu ST (2004) Temperature effect on liquid crystal refractive indices. *J Appl Phys* 96(1):19-24.

2. Leenhouts F, Vanderwoude F, & Dekker AJ (1976) Twist Elastic-Constant as a Function of Temperature for Nematic Mbba. *Phys Lett A* 58(4):242-244.

3. Horn RG (1978) Refractive-Indexes and Order Parameters of 2 Liquid-Crystals. *J Phys-Paris* 39(1):105-109.

4. Li J, Wen CH, Gauza S, Lu RB, & Wu ST (2005) Refractive Indices of Liquid Crystals for Display Applications. *J Disp Technol* 1(1):51-61.

5. Stark H & Ventzki D (2001) Stokes drag of spherical particles in a nematic environment at low Ericksen numbers. *Phys Rev E* 64(3).

6. Kneppe H & Schneider F (1981) Determination of the Viscosity Coefficients of the Liquid-Crystal Mbba. *Mol Cryst Liq Cryst* 65(1-2):23-37.

7. Drawhorn RA & Abbott NL (1995) Anchoring of Nematic Liquid-Crystals on Self-Assembled Monolayers Formed from Alkanethiols on Semitransparent Films of Gold. *J Phys Chem-Us* 99(45):16511-16515.

8. Shah RR & Abbott NL (2001) Coupling of the orientations of liquid crystals to electrical double layers formed by the dissociation of surface-immobilized salts. *J Phys Chem B* 105(21):4936-4950.

9. Miller WJ, Abbott NL, Paul JD, & Prentiss MG (1996) Planar anchoring of nematic 4-n-pentyl-4'-cyanobiphenyl on self-assembled monolayers formed from alkanethiols on gold. *Appl Phys Lett* 69(13):1852-1854.

10. Gupta VK & Abbott NL (1996) Uniform anchoring of nematic liquid crystals on self-assembled monolayers formed from alkanethiols on obliquely deposited films of gold. *Langmuir* 12(10):2587-2593.

11. Gupta VK & Abbott NL (1997) Design of surfaces for patterned alignment of liquid crystals on planar and curved substrates. *Science* 276(5318):1533-1536.

12. Berezin PD, Kompanet.In, Nikitin VV, & Pikin SA (1973) Orienting Effect of an Electric-Field on Nematic Liquid-Crystals. *Zh Eksp Teor Fiz+* 64(2):599-607.

13. Chandrasekhar S (1992) *Liquid crystals* (Cambridge University Press, Cambridge England ; New York, NY, USA) 2nd Ed pp xv, 460 p.

14. Wang M, He L, Zorba S, & Yin Y (2014) Magnetically actuated liquid crystals. *Nano Lett* 14(7):3966-3971.

15. Lelidis I & Durand G (1993) Electric-Field-Induced Isotropic-Nematic Phase-Transition. *Phys Rev E* 48(5):3822-3824.

16. Kreibig U & Vollmer M (1995) *Optical properties of metal clusters* (Springer, Berlin ; New York) pp xx, 532 p.

17. Bohren CF & Huffman DR (1983) *Absorption and scattering of light by small particles* (Wiley, New York) pp xiv, 530 p.

18. Hao E & Schatz GC (2004) Electromagnetic fields around silver nanoparticles and dimers. *J Chem Phys* 120(1):357-366.

19. Foteinopoulou S, Vigneron JP, & Vandenbem C (2007) Optical near-field excitations on plasmonic nanoparticle-based structures. *Opt Express* 15(7):4253-4267.

20. Linic S, Christopher P, & Ingram DB (2011) Plasmonic-metal nanostructures for efficient conversion of solar to chemical energy. *Nat Mater* 10(12):911-921.

21. Mukherjee S*, et al.* (2013) Hot Electrons Do the Impossible: Plasmon-Induced Dissociation of H-2 on Au. *Nano Lett* 13(1):240-247.

22. McFarland AD & Van Duyne RP (2003) Single silver nanoparticles as real-time optical sensors with zeptomole sensitivity. *Nano Lett* 3(8):1057-1062.

23. Haes AJ*, et al.* (2005) Plasmonic materials for surface-enhanced sensing and spectroscopy. *Mrs Bull* 30(5):368-375.

24. Kelly KL, Coronado E, Zhao LL, & Schatz GC (2003) The optical properties of metal nanoparticles: The influence of size, shape, and dielectric environment. *J Phys Chem B* 107(3):668-677.

25. Miller MM & Lazarides AA (2005) Sensitivity of metal nanoparticle surface plasmon resonance to the dielectric environment. *J Phys Chem B* 109(46):21556-21565.

26. Mock JJ, Barbic M, Smith DR, Schultz DA, & Schultz S (2002) Shape effects in plasmon resonance of individual colloidal silver nanoparticles. *J Chem Phys* 116(15):6755-6759.

27. Haynes CL, McFarland AD, Smith MT, Hulteen JC, & Van Duyne RP (2002) Angle-resolved nanosphere lithography: Manipulation of nanoparticle size, shape, and interparticle spacing. *J Phys Chem B* 106(8):1898-1902.

28. Koenig GM, Gettelfinger BT, de Pablo JJ, & Abbott NL (2008) Using localized surface plasmon resonances to probe the nanoscopic origins of adsorbate-driven ordering transitions of liquid crystals in contact with chemically functionalized gold nanodots. *Nano Lett* 8(8):2362-2368.

29. Sarid D & Challener WA (2010) *Modern introduction to surface plasmons : theory, Mathematica modeling, and applications* (Cambridge University Press, Cambridge ; New York) pp xiv, 371 p.

30. Nie S & Emory SR (1997) Probing Single Molecules and Single Nanoparticles by Surface-Enhanced Raman Scattering. *Science* 275(5303):1102-1106.

31. Shan J, Shi W, Liu LY, Shen YR, & Xu L (2012) Optical Control of Surface Anchoring and Reorientation of Liquid Crystals via a Plasmon-Enhanced Local Field. *Phys Rev Lett* 109(14).

32. Quint MT*, et al.* (2015) All-optical switching of nematic liquid crystal films driven by localized surface plasmons. *Opt Express* 23(5):6888-6895.

33. Sundararaman R, Narang P, Jermyn AS, Goddard WA, & Atwater HA (2014) Theoretical predictions for hot-carrier generation from surface plasmon decay. *Nat Commun* 5.

34. Ruhwandl RW & Terentjev EM (1997) Monte Carlo simulation of topological defects in the nematic liquid crystal matrix around a spherical colloid particle. *Phys Rev E* 56(5):5561-5565.

35. Poulin P, Stark H, Lubensky TC, & Weitz DA (1997) Novel colloidal interactions in anisotropic fluids. *Science* 275(5307):1770-1773.

36. Musevic I, Skarabot M, Tkalec U, Ravnik M, & Zumer S (2006) Two-dimensional nematic colloidal crystals self-assembled by topological defects. *Science* 313(5789):954-958.

37. Poulin P & Weitz DA (1998) Inverted and multiple nematic emulsions. *Phys Rev E* 57(1):626-637.

38. Grollau S, Kim EB, Guzman O, Abbott NL, & de Pablo JJ (2003) Monte Carlo simulations and dynamic field theory for suspended particles in liquid crystalline systems. *J Chem Phys* 119(4):2444-2455.

39. Hung FR (2009) Quadrupolar particles in a nematic liquid crystal: Effects of particle size and shape. *Phys Rev E* 79(2).

40. Koenig GM, de Pablo JJ, & Abbott NL (2009) Characterization of the Reversible Interaction of Pairs of Nanoparticles Dispersed in Nematic Liquid Crystals. *Langmuir* 25(23):13318-13321.

41. Koenig GM*, et al.* (2009) Single Nanoparticle Tracking Reveals Influence of Chemical Functionality of Nanoparticles on Local Ordering of Liquid Crystals and Nanoparticle Diffusion Coefficients. *Nano Lett* 9(7):2794-2801.

42. Loudet JC, Hanusse P, & Poulin P (2004) Stokes drag on a sphere in a nematic liquid crystal. *Science* 306(5701):1525-1525.

43. Bottger A, Frenkel D, Vanderiet E, & Zijlstra R (1987) Diffusion of Brownian Particles in the Isotropic-Phase of a Nematic Liquid-Crystal. *Liq Cryst* 2(4):539-547.

44. Kocevar K & Musevic I (2001) Forces in the isotropic phase of a confined nematic liquid crystal 5CB. *Phys Rev E* 64(5).

45. Bracic AB, Kocevar K, Musevic I, & Zumer S (2003) Capillary forces in a confined isotropic-nematic liquid crystal. *Phys Rev E* 68(1).

46. Stark H (2001) Physics of colloidal dispersions in nematic liquid crystals. *Phys Rep* 351(6):387-474.

Chapter 2

Thesis Overview

Chapters 3 and 4 in this thesis were originally written as manuscripts for publication. Chapter 5 has been written in a style matching Chapters 3 and 4 and these three chapters can be read independently. A description of each chapter is provided below.

In Chapter 3, we report experimental measurements using single-particle tracking of the diffusion of microparticles and nanoparticles at liquid crystal-aqueous interfaces, and highlight fundamental differences in the behaviors of the two sizes of particles (1). For the micrometer-sized particles (silica particles with diameters of 2.3 ± 0.2 μm, treated with dimethyloctadecyl[3-(trimethoxysilyl)propyl]ammonium chloride (DMOAP)), we measured the mobilities of the particles to be anisotropic (consistent with the influence of the nematic order of the LC) but higher than that which we predict on the basis of the location of the particles at the interface and bulk diffusion coefficients. Although optical characterization of the particles revealed dipolar topological ordering in bulk LC and at the interface, our results hint that differences in the configurations of the LC about the microparticles lowers the drag on the microparticles in the interfacial environment. We also measured the mobilities of nanoparticles (gold nanoparticles (diameter of 141 ± 11 nm, that were chemically functionalized with either a mixed monolayer of hexadecanethiol and decanethiol or a single component monolayer of decanethiol) at the LC-aqueous interface to differ in significant ways relative to the microparticles. An interesting observation is that the diffusion coefficients of the nanoparticles at the LC-aqueous interface appear to be relatively insensitive to the details of the interfacial environment. Specifically, for displacements in the same direction relative to the far-field director of the LC, identical diffusion

coefficients are measured at the interface and in bulk LC. Furthermore, when the 5CB is heated into the isotropic phase, the diffusion coefficient measured at the interface is indistinguishable to that measured in bulk 5CB. We emphasize that similar observations were not made for microparticles, and that the relative insensitivity of the nanoparticles to interfacial environment appears to be a property of the smaller particles studied in our experiments. A third significant conclusion is that the chemical functionality of the nanoparticles influences their interfacial diffusion at 40˚C, a temperature above the nematic-isotropic transition. Nanoparticles with a mixed organothiol monolayer were determined to have smaller interfacial diffusion coefficients than nanoparticles with single component monolayers. This suggests the presence of residual ordering of 5CB at the particle surface above the bulk phase transition (in the interfacial environment). While prenematic wetting has been reported previously at a number of interfaces (2-4), we estimate the hydrodynamic thickness of the ordered solvent layer to be ~30 nm at a temperature 5˚C above the bulk clearing temperature, a value that is much larger than that previously reported. Overall, our results reveal striking differences between the dynamic behaviors of microparticles and nanoparticles at LC-aqueous interfaces. In particular, the mobilities of the nanoparticles are surprisingly insensitive to the differences between the bulk and interfacial microenvironment when compared to the microparticles. This chapter also identifies several experimental observations related to particle mobilities at LC-aqueous interfaces that remain to be fully understood.

In Chapter 4, we expand on our observation in Chapter 3 of the surprisingly large hydrodynamic sizes of nanoparticles in the isotropic phases of liquid crystalline materials. Specifically, by performing single-particle tracking on gold particles (85 ± 7 nm and 164 ± 11 nm in diameter) with organothiol monolayers dispersed in the isotropic phases of the

mesogenic solvents 5CB and MBBA, we measure optically-induced changes in solvation at temperatures that place the solvent within 5˚C of the nematic-isotropic transition, and to result in increases in hydrodynamic diameters of up to 54±12 nm. By performing a number of experiments to test several hypotheses, including ordering of the solvent by electric fields associated with LSPR and local heating of the solvent, we demonstrate that the optical excitation of electrons within metals can induce a separation of charge and thereby generate interfacial electrical fields that restructure solvent. We show that optically induced solvent restructuring at the interface of nanoparticles can be used to manipulate the diffusion of the nanoparticles. Consistent with the proposed mechanism, the diffusion of the nanoparticles is dependent on the wavelength of illumination of the nanoparticles and on the size of the nanoparticles. In addition, we show that the optically-induced solvent restructuring changes the dielectric environment of metal islands and thus leads to measurable changes in resonant optical properties of the metal islands. Overall, the principles identified in this chapter hint at general methods for achieving control over the solvation of a wide range of materials dispersed in polar solvents.

In Chapter 5, we investigate the size-dependence of microparticle and nanoparticle mobility, observed at LC-aqueous interfaces in Chapter 3, in bulk nematic 5CB. Using single-particle tracking to measure the mobilities of gold nanoparticles (diameters ranging from 85 ± 7 nm to 380 ± 30 nm) functionalized with monolayers of organothiols and, we find that the apparent viscosity of the nanoparticles is significantly smaller from the apparent viscosity of microparticles (diameters of 1.2 ± 0.1 μm) with the same surface anchoring conditions. A particularly interesting observation is that there is no change in apparent viscosity of the nanoparticles over the measured size range. To test the possibility that the observed change in apparent viscosity as particle diameter decreases from the microscale to the nanoscale is due to

differences in the composition or surface chemistry, we measured the apparent viscosities of 391 ± 33 nm silica particles. We show that when functionalized with the same surface chemistry, the silica nanoparticles have a significantly smaller apparent viscosity than the microparticles. In addition, we test for the effects of electric fields generated by the illumination of gold nanoparticles with specific wavelengths of light as observed in Chapter 4, however observe no dependence of the apparent viscosity of gold nanoparticles on the wavelength of illumination of the incident light. However, we do observe that the apparent viscosity of the gold nanoparticles does depend on the chemical functionality in a manner consistent with previous studies (5). Our results indicate a size-dependent change in the local ordering of liquid crystals around particles its diameter decreases from 1.2 ± 0.1 nm to 391 ± 33 nm yet indicate no size-dependence in the local ordering of liquid crystals as the diameter decreases from 391 ± 33 nm to 85 ± 7 nm.

2.1 References

1. Abras D, Pranami G, & Abbott NL (2012) The mobilities of micro- and nano-particles at interfaces of nematic liquid crystals. *Soft Matter* 8(6):2026-2035.

2. Bottger A, Frenkel D, Vanderiet E, & Zijlstra R (1987) Diffusion of Brownian Particles in the Isotropic-Phase of a Nematic Liquid-Crystal. *Liq Cryst* 2(4):539-547.

3. Kocevar K & Musevic I (2001) Forces in the isotropic phase of a confined nematic liquid crystal 5CB. *Phys Rev E* 64(5).

4. Bracic AB, Kocevar K, Musevic I, & Zumer S (2003) Capillary forces in a confined isotropic-nematic liquid crystal. *Phys Rev E* 68(1).

5. Koenig GM*, et al.* (2009) Single Nanoparticle Tracking Reveals Influence of Chemical Functionality of Nanoparticles on Local Ordering of Liquid Crystals and Nanoparticle Diffusion Coefficients. *Nano Lett* 9(7):2794-2801.

Chapter 3

The Mobilities of Micro- and Nano-Particles at Interfaces of Nematic Liquid Crystals

3.1 Abstract

We report the use of single-particle tracking to measure the diffusion coefficients of chemically functionalized micro- and nano-particles at interfaces between aqueous phases and a nematic liquid crystal (LC). For hydrophobic particles with diameters of 2.3 ± 0.2 μm that homeotropically anchors the LC, we measured anisotropic diffusion, qualitatively consistent with the influence of nematic ordering of the LC at the interface on the local rheological environment. Analysis of the magnitudes of the diffusion coefficients reveal that the ordering of the LC about the microparticles is perturbed in the interfacial environment relative to the bulk, leading to low drag on the microparticles at the aqueous-nematic interface. In contrast, for hydrophobic nanoparticles (diameters of 141 ± 11 nm) at the LC-aqueous interface, almost indistinguishable diffusion coefficients were measured at the interface and in bulk LC when the displacements of the nanoparticles in the two environments were in the same directions relative to the far-field director of the LC. These results and others reported in this chapter reveal fundamental differences to exist between the interfacial mobilities of micro- and nanoparticles at LC-aqueous interfaces, and that a relative insensitivity to interfacial environment appears to be a property of the smaller particles studied in our experiments. These findings are discussed in light of past studies of the diffusion of particles at either isotropic liquid interfaces or in bulk LCs.

3.2 Introduction

Past studies have established that solid particles adsorb strongly to the interface between two fluid phases, and that interactions between particles confined to such interfaces can lead to formation of two-dimensional organized assemblies of particles (1-3). This phenomenon has received particular attention in the context of liquid-liquid interfaces, because the particle assemblies can stabilize a dispersion of one liquid in another without requiring the use of molecular surfactants (Pickering emulsions) (4-11). Whereas the studies mentioned above address particles at interfaces between isotropic liquids, this chapter moves to investigate particles at interfaces of liquid crystals (LCs). At LC interfaces, several studies have demonstrated that LC-mediated interactions can lead to spontaneous formation of hexagonal and chain-type organizations of particles (12-16). Of particular relevance to the current study, Koenig *et al*. have shown that dynamic and reconfigurable assemblies of micrometer-sized particles can be created at nematic LC-water interfaces by driving ordering transitions in the LC via adsorption and desorption of water-soluble surfactants from the LC-aqueous interface (15). The rate-determining processes underlying these dynamic ordering transitions, however, remain to be fully elucidated. As a first step towards understanding these dynamics, here we investigate the lateral mobilities of particles adsorbed at LC-aqueous interfaces.

For an interface between two isotropic fluids, the mobility of a particle is influenced by the location of the particle at the interface, which in turn determines the fraction of the surface area of the particle in contact with each fluid (16-24). The interfacial mobility of the particle is, however, not simply the surface-area weighted average of the mobilities of the particle in each bulk phase because (i) the presence of the interface changes the flow around the particle, and (ii) the interface can possess a so-called “interfacial viscosity”. For air-liquid interfaces, the relative

importance of interfacial and bulk liquid viscosity on particle mobility is expressed by the Boussinesq number (B_0)

$$B_0 = \frac{\eta_S P_C}{\eta A_C} \quad (1)$$

where η_S is the interfacial viscosity, P_C is the length of the contact line between the particle and interface, η is a bulk liquid viscosity, and A_C is the surface area of the particle. Because the ratio P_C/A_C increases with a decrease in particle size, the importance of the interfacial viscosity increases with decreasing particle size. At interfaces of isotropic liquids decorated with amphiphiles (21), proteins (22), or oils (20), several measurements of interfacial viscosities have been reported, with values ranging from 0.1 to 10 mPa.s.μm. Here we note that 4-pentyl-4'-cyanobiphenyl (5CB), the mesogen used in the current study, forms stable monolayers at the surface of water (*i.e.*, is amphiphilic) (25, 26), and thus we considered it possible that the mobilities of particles at LC-aqueous interfaces would be impacted by the interfacial viscosity of the near-surface region of the 5CB at the aqueous interface. At LC interfaces, additional complexities are anticipated to arise because the long-range nematic ordering of the LC creates an anisotropic mechanical environment, and because the surface anchoring and flow of the LC around the particles at the interface can potentially impact the local ordering of the LC and thus also the rheological environment.

Our study of colloidal particles at LC interfaces builds from past investigations of the mobility of particles in bulk LCs (27-32). In particular, Poulin and coworkers have investigated the influence of a nematic field on the diffusion of micrometer-sized droplets of isotropic liquid dispersed in a bulk LC (33). The diffusion coefficient of a micrometer-sized droplet with a Saturn-ring defect moving parallel to the far-field director was found to be higher than the diffusion coefficient for motion perpendicular to the director, indicating that the anisotropic

mechanical environment defined by the nematic phase leads to anisotropic motion of the droplets. In addition, recent studies have suggested that the local ordering of mesogens about nanoparticles may be different than that about micrometer-sized particles, and that these differences are reflected in measurements of mobilities of nanoparticles performed in bulk LCs (see below for additional discussion) (32). In this chapter, we investigate how particle diffusion at LC-aqueous interfaces is influenced by the orientational ordering of the LC at the interface. In particular, because nanoparticles adsorbed to the LC-aqueous interface probe the region of the LC closer to the interface than micrometer-sized particles, we sought to characterize size-dependent mobilities of particles at the LC interface. We note that past studies have demonstrated that the ordering of LCs close to interfaces can differ substantially from the far-field orientation (34). Thus, at the outset of this investigation, it seemed possible to us that particles, particularly the nanoparticles as described below, might experience interfacial microenvironments that differ from those predicted based on extrapolation of the far-field ordering of the LC to the interface (35). We also report on the influence of surface-driven ordering transitions at the aqueous-LC interface on the mobilities of particles at these interfaces.

3.3 Materials and Methods

The LC used in our study was 4-pentyl-4'-cyanobiphenyl (5CB), a thermotropic LC that exhibits a nematic phase between 24˚C and 35˚C.27 Silica microparticles (diameter of 2.3 ± 0.2 μm; Bangs Labs, Fishers, IN) were functionalized with dimethyloctadecyl[3-(trimethoxysilyl)propyl]ammonium chloride (DMOAP; Acros, Geel, Belgium). DMOAP reacts to form covalent bonds with surface silanol groups on silica (36, 37) resulting in homeotropic (perpendicular) anchoring of nematic 5CB (see Appendix A for details regarding the synthesis of the particles) (38). Gold nanoparticles (diameter of 141 ± 11 nm; Ted Pella, Inc., Redding, CA) were functionalized with either single-component or mixed monolayers of alkanethiols. As described previously, mixed monolayers formed from decanethiol and hexadecanethiol (5:1, 4 mM total concentration in solution) cause homeotropic anchoring of nematic 5CB whereas a monolayer formed from only decanethiol causes planar anchoring of 5CB (39-41).

The chemically functionalized micro- and nano-particles (as described above) were deposited onto the 5CB-aqueous interface by sedimentation from an overlying aqueous phase. The particles were dispersed in water by sonication and then a droplet (diameter of ~5 mm) of the dispersion was introduced into the aqueous phase overlying a 20 μm-thick film of nematic 5CB stabilized within a gold specimen grid (Electron Microscopy Sciences, Hatfield, PA). The grid was supported on a gold-coated glass microscope slide placed into the bottom of a glass dish (Electron Microscopy Sciences, Hatfield, PA). The glass slide was coated with gold by vapor deposition at an oblique angle of incidence and subsequently functionalized using decanethiol (42, 43). As noted above, a monolayer formed from decanethiol causes planar anchoring of nematic 5CB (39-41). The oblique deposition of gold leads to a uniform azimuthal orientation of the LC. The individual pores of the gold specimen grid were 280 μm x 280 μm,

which is large compared to the diameters of the particles used in our experiments. The dish was filled with 5 mL of either aqueous 0.1 M sodium perchlorate, which causes planar anchoring of the 5CB at the LC-aqueous interface, or 8 M sodium perchlorate, which causes perpendicular anchoring of 5CB at the LC-aqueous interface. In all experiments reported in this chapter, the area fraction of particles on the interface was sufficiently low (~10^{-6}-10^{-2}) that interparticle interactions did not influence the diffusion of the particles (44). We also note that we measured the nematic-to-isotropic transition temperature of the 5CB following equilibration against aqueous solutions containing up to 8 M sodium perchlorate, and we measured no change in the clearing temperature. From this result, we conclude that any salts or water that partitions into 5CB are not at sufficient concentrations to substantially change the phase behavior of 5CB.

The silica microparticles were imaged at the LC-aqueous interface using an Olympus BX60 configured for bright-field microscopy. The gold nanoparticles were imaged using an Olympus BX41 configured for dark-field microscopy with a 60x objective (numerical aperture of 0.9) immersed into the aqueous phase. We note that bright-field microscopy cannot resolve particles smaller than approximately 500 nm (the cut-off is dependent on the numerical aperture of the microscope objective) at the 5CB-aqueous interface.

The displacements of the particles at the 5CB-aqueous interface were recorded over a period of 3 minutes, at a frame-grab rate of 30 frames per second, using a monochrome camera (Cohu 4915-2010/0000) with a resolution of 640 x 480 pixels. A detailed description of methods used to analyze particle trajectories can be found elsewhere (45). In brief, the distribution of particle displacements in one dimension can be fit to a Gaussian function with the form

$$P(\delta,\tau) = P_0 e^{-\frac{\delta^2}{\Delta^2(\tau)}} \qquad (2)$$

where P is the probability that the particle will diffuse a distance δ in time τ, and the normalization constant of the distribution is P_o (45). The width of the distribution, 2Δ, was measured in two orthogonal directions within the plane of the interface, defined as being parallel or perpendicular to the bulk director. Below, we refer to these directions as the x-direction and y-direction, respectively. The diffusion coefficient, D, perpendicular or parallel to the bulk director of the particle is related to Δ by $D=\Delta^2/2d\tau$, where d is the dimension of the trajectory.

The majority of experiments reported in this chapter were performed at 26˚C, at which temperature 5CB exhibits a bulk nematic phase. Experiments with isotropic phases of 5CB were performed at 40˚C by using a microscope placed within a temperature-controlled chamber. To assess reproducibility, three independent experiments were conducted for each experimental condition. Variations in the experimental results are shown by error bars which represent the standard error of the measurement.

3.4 Results

Ordering of LCs Around Micrometer-Sized Particles Adsorbed at the LC-Aqueous Interface.

We and others have previously reported on the ordering of nematic 5CB around either microdroplets (46, 47) or silica microparticles (35, 38) (diameter 2.3 ± 0.2 μm) functionalized with DMOAP. When the microparticles were either dispersed in bulk LC or adsorbed at the LC-aqueous interface, the microparticles were observed to generate optical textures in the LC that were consistent with so-called hyperbolic hedgehog defects. Hyperbolic hedgehogs comprise a point defect, which in combination with the particle, define a topological dipole (35, 38, 46, 47). Figure 3-1a and 3-1b show images obtained using crossed polars and brightfield conditions, respectively, of a microparticle that exhibited a dipolar defect at the 5CB-aqueous interface. Schematic illustrations of a director profile that are consistent with the images in Figure 3-1a and 3-1b are shown in Figure 3-1c and 3-1d. We note that for the observations reported in Figure 3-1a and 3-1b, the anchoring of the LC was parallel to the aqueous interface, and thus the axis of the topological dipole defined by the particle and point defect was parallel to the aqueous interface. These results are consistent with strong perpendicular anchoring of the LC at the particle surface (48).

We note, however, that when preparing DMOAP-functionalized microparticles for this study, we observed that some batches of microparticles formed Saturn ring defects (defects with quadrupolar symmetry, and a clearly observed disclination line around the particle) in bulk 5CB (49). Past studies have established that the structure and properties of silane-based monolayers are strongly dependent on details of the experimental conditions (*e.g.*, amount of water in solvents) used to form the monolayers (50). Our results are consistent with batch-to-batch variation in the anchoring energy of 5CB on the DMOAP-treated particles, with particles

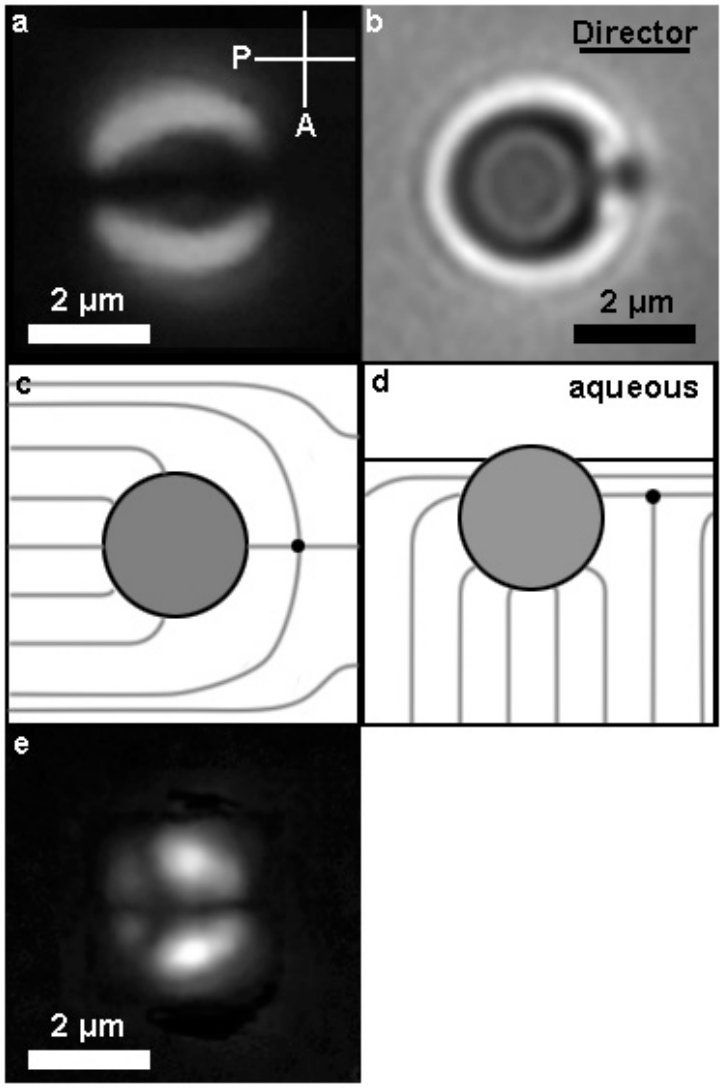


Figure 3 - 1. Polarized light micrographs of DMOAP-functionalized silica particles (diameters of 2.3 ± 0.2 µm) at a nematic 5CB–aqueous interface. The aqueous phase contained 0.1 M sodium perchlorate, which causes planar anchoring of 5CB at the aqueous interface. Note that the bottom substrate is functionalized with DMOAP, which causes homeotropic anchoring of the LC and thus facilitates imaging of the defect. The homeotropic anchoring gives rise to hedgehog defects that appear brighter than the surrounding medium in brightfield micrographs due to a uniform tilt angle of the LC director below the defect. (a) Crossed polars and (b) bright-field imaging of a particle with a hyperbolic hedgehog defect. The orientations of the analyzer (A) and polarizer (P) are shown. (c) Schematic illustration of top and (d) side view of the LC director for a particle with a hyperbolic hedgehog defect at the aqueous–LC interface, as shown in A and B. (e) Polarized light micrograph (crossed polars) of a particle at the aqueous–LC interface that when dispersed in bulk LC produced a Saturn ring defect.

with low anchoring energies giving rise to the observation of quadrupolar defects in the LC (and, as noted above, batches of particles with high anchoring energies giving rise to dipolar defects). We note that variation in the concentration of DMOAP in the initial reaction mixture during particle functionalization can lead to the formation of multilayers which can affect the anchoring energy of the LC at the particle surface. The microparticles that generated Saturn ring defects in the bulk LC, when adsorbed at the aqueous-LC interface, exhibited optical signatures (Figure 3-1e) that were clearly different from the particles shown in Figure 3-1a and 3-1b. Our attempts to interpret the optical textures generated by these particles at the LC-aqueous interface did not, however, lead to an unambiguous conclusion regarding the director configuration. We note that a computational study by Andrienko and coworkers has predicted that adsorption of a particle with a Saturn ring defect to a nematic-isotropic interface will lead to a line disclination in the LC that terminates at the nematic-isotropic interface (51). Our observations between crossed polars (Figure 3-1e), however, are not consistent with the symmetry of the director configuration predicted by Andrienko *et al.* (51). Here we emphasize that each batch of DMOAP-treated particles that we prepared for the experiments reported in this chapter exhibited *either* hyperbolic hedgehog defects or Saturn ring defects in bulk LC. We did not observe any batches of particles to produce a mixture of the two types of defects. For the experiments reported below, after the synthesis of each batch of microparticles, we characterized the particles in bulk 5CB to determine the type of defect induced in the LC. We compare measurements of the interfacial mobilities of both types of microparticles, but we focus our detailed analysis on particles with dipolar defects.

Diffusion Coefficients of DMOAP-Treated Particles at the Nematic 5CB-Aqueous Interface

Prior to performing measurements with nematic 5CB, to confirm that our experimental methods yielded unbiased measurements of the diffusion of particles at an isotropic oil-aqueous interface (see Appendix B for experimental protocols that were required to achieve reproducible measurements), we measured the mean-squared-displacement (MSD) of DMOAP-treated microparticles as a function of the time with 5CB heated into the isotropic phase. For Brownian motion at a purely viscous interface, the MSD should be linear with respect to the time, and a best-fit straight line should pass through the origin. We considered an individual trajectory as arising from unbiased Brownian particle diffusion at the interface if a straight line could be fit to the MSD with 95% certainty using a χ^2 goodness-of-fit test. As an example, Figure 3-2a shows the MSD for a DMOAP-functionalized microparticle diffusing at the interface of the 5CB heated to 40˚C (isotropic phase). Inspection of Figure 3-2a shows that the MSD of the microparticle at the interface of isotropic 5CB increases linearly with time (*i.e.*, purely viscous environment), and that it is indistinguishable when measured in orthogonal directions on the interface. The linearity of the MSD as a function of time was observed to extend to measurements performed over 3 minutes. From these measurements, we calculated the diffusion coefficients of the microparticles in the two orthogonal directions within the plane of the interface to be 0.0130 ± 0.0003 $\mu m^2/s$ and 0.0136 ± 0.0003 $\mu m^2/s$. We return below to provide an interpretation of the magnitude of these diffusion coefficients.

Our initial measurements at the *nematic* 5CB-aqueous interface were performed to determine if diffusion of the DMOAP-functionalized particles at the LC interface was anisotropic. For these measurements, the aqueous phase contained 0.1 M sodium perchlorate which, as noted above, gives rise to far-field anchoring of the LC that is parallel to the aqueous

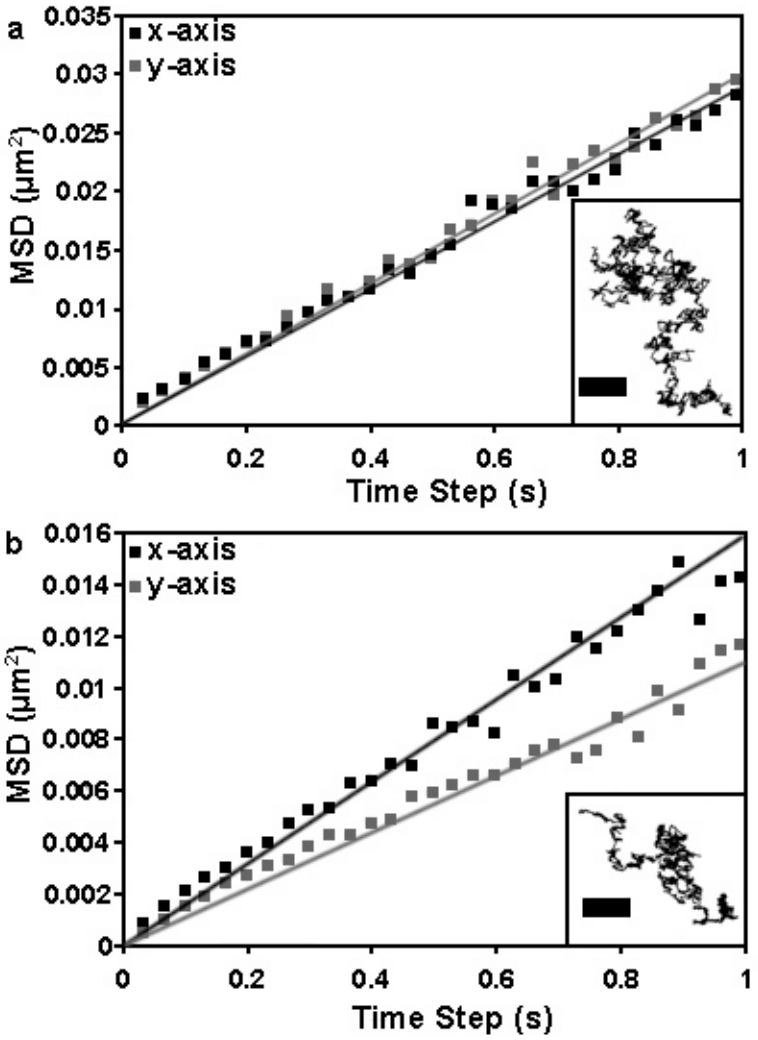


Figure 3 - 2. Mean squared displacement (MSD) of a single DMOAP-functionalized particle (diameter of 2.3 ± 0.2 μm) at a 5CB–aqueous interface, plotted as a function of time, at either (a) 40 °C or (b) 26 °C. At 26 °C, the nematic LC was anchored parallel to the aqueous interface. A particle trajectory is shown as an inset in each plot. Solid lines indicate a least squares fit to the MSD data.

interface. Similar to the case of isotropic 5CB (Figure 3-2a), we measured the MSD of the particles at the nematic interface to increase as a linear function of time (for directions parallel and perpendicular to the far-field director), consistent with a purely viscous interfacial environment (Figure 3-2b). In contrast to isotropic 5CB, however, the measurements performed at the nematic interface (with DMOAP-functionalized microparticles that generated hyperbolic hedgehog defects in bulk LC, see above) did reveal anisotropic mobilities. As quantified in Figure 3-3a, the diffusion coefficient of the microparticle in the x-direction along the interface (where, as noted above, the x-direction is parallel to the far-field director) is larger than along the y-direction. Because the mobility of the microparticles measured at 40˚C (isotropic phase) was not anisotropic (Figure 3-2a), we conclude that the anisotropy in the diffusion coefficients of the microparticles measured at 26°C is due to the nematic ordering of the 5CB phase. The observation of anisotropic diffusion is qualitatively similar to past measurements of the diffusion of micrometer-sized droplets of oil in LC (see below) (33), and consistent with contact between the interface-bound microparticles in our experiments and the nematic LC.

To interpret the above-reported measurements of the diffusion coefficients of the microparticles at the LC-aqueous interface, we calculated the apparent viscosities (ν_{app}) experienced by the microparticles (with hyperbolic hedgehog defects) by using the Stokes-Einstein equation,

$$D = \frac{kT}{6\pi\upsilon_{app}R} \quad (3)$$

where D is the diffusion coefficient, k is the Boltzmann constant, T is the absolute temperature, and R is the radius of the particle. At 26˚C, we calculated the apparent viscosity experienced by the particles to be 25.8 ± 0.5 mPa.s for displacements in the x-direction and 34.9 ± 0.6 mPa.s for displacements in the y-direction. When heated to 40˚C, the apparent viscosity of the particles at

the interface decreased to 14.7 ± 0.3 mPa.s. We make two comments regarding these apparent viscosities. First, we note that the apparent viscosities experienced by the microparticles at the LC-aqueous interface fall between the two smaller Miesowicz shear viscosities of bulk 5CB (129.6 mPa.s, 37.4 mPa.s, 22.9 mPa.s) (52). They are also much larger than the viscosity of water at 26˚C (0.87 mPa.s), as measured with an Ubbelohde viscometer. The latter statement also holds true for 5CB in the isotropic phase (the viscosity of bulk isotropic 5CB at 40˚C is 22 mPa.s) (53), and leads us below to neglect the role of viscous drag from the aqueous phase in our analysis of the mobility of the particles at the aqueous-LC interface. Second, we compare our measurement to the past studies of Stark and coworkers, who calculated the apparent viscosities of solid particles with hyperbolic hedgehog defects in *bulk* 5CB to be 52.5 mPa.s for diffusion in the x-direction (parallel to far-field director) and 86.4 mPa.s for diffusion in the y-direction (52). We note that these predicted values are significantly larger than our measurements for particles at the nematic 5CB-aqueous interface, as reported above (25.8 ± 0.5 mPa.s and 34.9 ± 0.6 mPa.s; see Figure 3-3 for a comparison of the related diffusion coefficients). This difference is qualitatively consistent with only partial penetration of the microparticles into the LC phase at the aqueous-LC interface. In addition, we note that the anisotropy of the diffusion coefficients, as characterized by the *ratio* of diffusion coefficients measured perpendicular versus parallel to the far-field director, is found to be substantially lower at the LC-aqueous interface (1.35 ± 0.04) as compared to bulk 5CB (1.64, as reported by Stark and coworkers).

To determine the location of the microparticles at the 5CB-aqueous interface, and thus the fraction of the surface area of each microparticle in contact with either the LC or the aqueous phase, we measured the contact angles of 5CB under 0.1 M aqueous sodium perchlorate on DMOAP-coated silica surfaces. Here we note that Petkov *et al.* reported good agreement

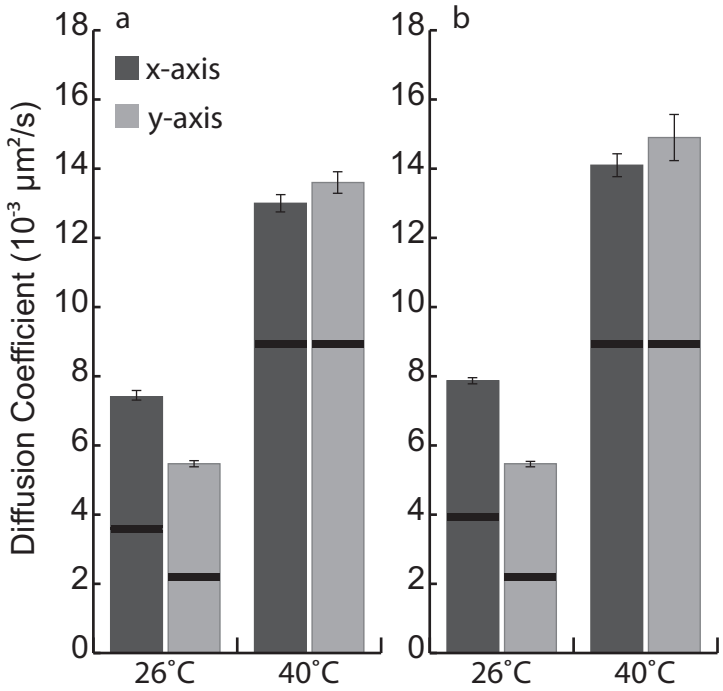


Figure 3 - 3. Diffusion coefficients for DMOAP-functionalized silica particles (diameters of 2.3 ± 0.2 μm), measured at either 26°C or 40°C, at a 5CB–aqueous interface with planar anchoring. Results are reported for diffusion along the far-field director (*x*-axis) and perpendicular to the far-field director (*y*-axis). (a) Data for particles that exhibited hyperbolic hedgehog defects in bulk 5CB. (b) Data for particles that exhibited Saturn ring defects in bulk 5CB. The black, horizontal lines indicate values of diffusion coefficients of 2.3 μm particles in bulk 5CB, as calculated either using apparent viscosities reported by Stark and coworkers at 26°C (54) or an experimentally measured apparent viscosity of 22 mPa.s at 40°C.

the locations of microparticles at air-water interfaces calculated from contact angles and those directly measured (19, 35). For DMOAP-coated silica surfaces, we measured the contact angle of 5CB under aqueous solution at 26˚C and 40˚C to be 38˚ ± 3˚, independent of temperature (and thus phase of the 5CB) within the precision of our measurements. This result indicates that the DMOAP-coated particles are located substantially on the 5CB side of the interface (as shown in Figure 3-1d).

To further verify our conclusion regarding the location of the microparticles at the 5CB-aqueous interface, we used the above-determined location of the microparticles and the values of bulk aqueous and isotropic 5CB viscosities to calculate the apparent viscosity experienced by the DMOAP-coated microparticles. In brief, for the surface of an isotropic liquid, Leal and Brenner proposed the use of a modified form of the Einstein relation to describe particle diffusion, namely

$$D = \frac{kT}{f 6\pi \upsilon R} \qquad (4)$$

where *f*, the drag coefficient, accounts for the effect of the interface on the geometry of the fluid path and ν is the viscosity experienced by the particle in the bulk liquid (17). The drag coefficient in Eq. (4) can be calculated from a constitutive relationship reported by Danov and coworkers (which includes the effects of interfacial viscosity) (18, 19). As noted above, because the viscosity of the aqueous phase is much lower than isotropic 5CB, the above-described analysis can be applied to microparticles at isotropic 5CB-aqueous interfaces. For a particle at the 5CB-aqueous interface at 40˚C, we calculated a drag coefficient of f = 0.68 and thus the apparent viscosity experienced by the DMOAP-coated microparticles (where $\nu_{app} = f\nu$ and, as noted above, the viscosity of bulk isotropic 5CB at 40˚C is 22 mPa.s) (53) to be 15.0 mPa.s. This value is in close agreement with the experimental values reported in Figure 3-4 (14.7 ± 0.3 mPa.s).

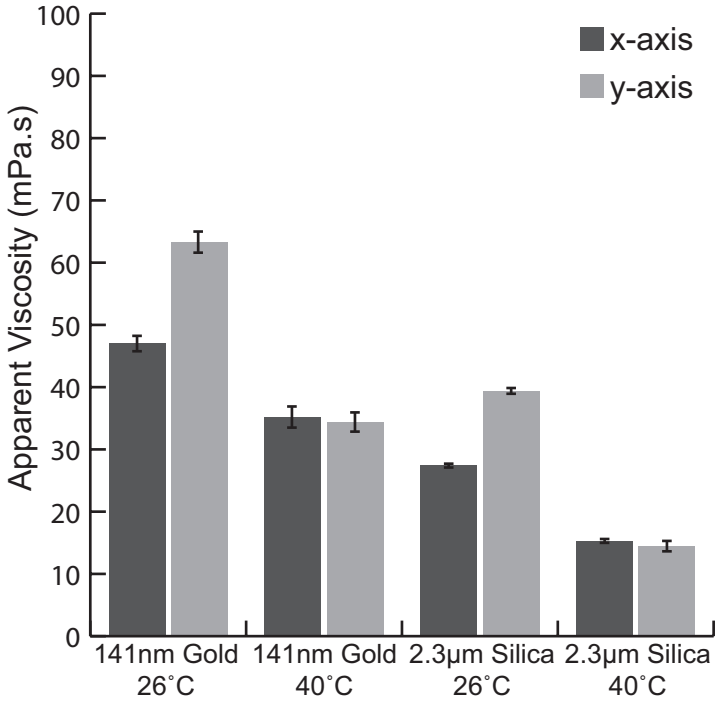


Figure 3 - 4. Influence of particle size on the apparent viscosity of either gold nanoparticles (141 ± 11 nm in diameter) or silica microparticles (2.3 ± 0.2 μm in diameter) at a 5CB–aqueous interface with planar anchoring of the LC. The gold particles were functionalized with mixed monolayers of alkanethiols and the silica particles were functionalized with DMOAP (see text for details).

In summary, for isotropic 5CB, our experimental measurements of the mobilities of DMOAP-coated particles at the 5CB-aqueous interface are found to be in close agreement with values calculated from bulk viscosities and the location of the microparticles at the interface.

Building from the above conclusions regarding the behaviors of the microparticles at the isotropic 5CB-aqueous interface, we next considered the microparticles at the *nematic* 5CB-aqueous interface. Specifically, by using the bulk apparent viscosities calculated by Stark *et al.* for microparticles diffusing parallel and perpendicular to the far field director (52), and our experimental measurements of the apparent viscosities experienced by the particles at the aqueous-LC interface (Figure 3-4), we calculated (using Eq. 4) the drag coefficients of the DMOAP-coated microparticles at the nematic 5CB-aqueous interface to be 0.49 ± 0.01 and 0.40 ± 0.01 for diffusion in the x- and y-directions, respectively. These values of the drag coefficient are significantly lower than those measured (and calculated) at the isotropic 5CB-aqueous interface (see above). We considered several factors that we thought might underlie the low drag coefficient measured at the LC interface. First, we considered that the elastic energy associated with distortion of the LC about the particle in contact with the nematic phase might change the location of the microparticle at the interface. We calculate, however, that the contribution of interfacial tension to the adsorption energy of the microparticles at the aqueous-5CB interface is at least $\sim 10^7$ kT, and thus much larger than the energetic effects associated with elastic deformation of the LC about the microparticles (10^3 kT to 10^4 kT, estimated as KR, where K is the one constant approximation of the elastic constant of the LC) (35, 54). The latter effect can thus be neglected in calculating the location of the microparticles at the interface. Therefore, a change in position of the particles at the interface due to elastic forces mediated by the LC is unlikely to underlie the low drag coefficient measured (relative to the isotropic phase) at the

interface of the LC. Next we considered it possible that nematic ordering of the 5CB may lead to an interfacial viscosity that measurably impacts the microparticle drag. Inclusion of the effects of an interfacial viscosity, however, would only serve to increase the calculated apparent viscosity experienced by the particles at the interface (and thus increase the difference between the calculated and experimental mobilities). Finally, we considered that the low drag coefficient may reflect an ordering of LC about the microparticles that is changed (relative to a particle in bulk LC) by the presence of the LC-aqueous interface. Here we note that the apparent viscosities experienced by the microparticles are larger than the lowest of the Miezowitz viscosities (22.9 mPa.s), and thus this latter explanation appears the most likely of the above three to underlie our experimental observations.

Overall, our measurements indicate that microparticles at aqueous interfaces of LCs experience anisotropic rheological environments, and that transfer of microparticles from the bulk LC to the aqueous-LC interface changes the diffusion coefficients of the microparticles. In particular, the apparent viscosities experienced by the microparticles at the interface are substantially lower than those in the bulk LC, and the drag coefficients evaluated for particles on the LC interface suggests that the configurations of the LC around particles near the aqueous-LC interface are biased to those that minimize the drag on the particle (relative to the bulk). *We emphasize these behaviours here because they are in striking contrast to those of nanoparticles that we address in the following sections.*

Before concluding this section, however, we also briefly comment that we measured the diffusion coefficients of batches of the DMOAP-treated microparticles that exhibited the optical textures at the LC-aqueous interface shown in Figure 3-1e. Although the ordering of the LC is optically distinct for the particles shown in Figure 3-1e versus Figures 3-1a and 3-1b, we

measured the diffusion coefficient of the two classes of particles to be indistinguishable (Figure 3-3b). Past calculations of particles in bulk 5CB by Stark *et al.* have predicted that particles with quadrupolar and dipolar defects experience similar apparent viscosities (52). Our observation that microparticles with dipolar and quadrupolar defects in bulk LC, when transferred to the interface, exhibit similar mobilities also indicates that the two types of particles experience similar apparent viscosities at the LC interface.

Effect of Particle Size on Mobility at the LC-Aqueous Interface

Past studies of particles dispersed in bulk 5CB have concluded that the local ordering of LCs around nanoscopic particles (*i.e.* particles with diameters of ~100 nm or smaller) is likely different from that of microparticles (15). The experimental evidence for size-dependent ordering is based on measurements of (i) interparticle interactions (55) and (ii) particle mobility in bulk LC (32). Of particular relevance to this chapter, the apparent viscosity experienced by 169 ± 2 nm gold particles (functionalized with a mixed monolayer of organothiols) diffusing perpendicular to the far-field director has been reported as 58.9 ± 1.1 mPa.s (32), smaller than the value calculated by Stark *et al.* for microparticles (86.4 mPa.s for a micrometer-sized particle with a hyperbolic hedgehog defect, and 85.3 mPa.s for a microparticle with a Saturn ring defect) (52). The low apparent viscosity experienced by the 169 ± 12 nm gold particles supports the proposition that the local ordering of the LC near nanoparticles is different from that near the microparticles (32).

To provide insight into the influence of the size of colloidal particles on their mobility at LC interfaces, we measured the diffusion coefficients of chemically functionalized gold nanoparticles (diameters of 141 ± 11 nm) at the 5CB-aqueous interface and compared the measurements to those of microparticles (as reported above). Similar to the experiments

performed with microparticles, 0.1 M sodium perchlorate was added to the aqueous phase to achieve planar anchoring of the 5CB at the aqueous interface. The gold nanoparticles were functionalized with mixed monolayers formed from decanethiol and hexadecanethiol, creating homeotropic anchoring at the nematic 5CB-nanoparticle interface (39-41). We find that the diffusion coefficients of the gold nanoparticles at the nematic 5CB-aqueous interface are higher than those of microparticles. The anisotropy in the average diffusion coefficients measured for the nanoparticles and microparticles, however, are indistinguishable at 1.39 ± 0.08 and 1.44 ± 0.03, respectively. Also similar to our experiments with microparticles, the anisotropic surface diffusion of the nanoparticles was measured to vanish upon heating of the 5CB to 40˚C. This result supports our conclusion that the origin of the anisotropic diffusion of the nanoparticles at the aqueous interface of the 5CB is also the nematic ordering of the 5CB.

To provide insight into the above observations, we calculated the apparent viscosities experienced by the nanoparticles diffusing at the interface of the LC and compared them to the equivalent quantity for the microparticles (Figure 3-4). These measurements reveal the surprising result that the nanoparticles at the interface of 5CB experience a substantially larger apparent viscosity as compared to the microparticles. The apparent viscosities experienced by the nanoparticles were 43.9 ± 1.2 mPa.s and 59.1 ± 1.7 mPa.s for diffusion in the x- and y-directions, respectively. In contrast, we measured the microparticles to experience apparent viscosities of 24.3 ± 0.3 mPa.s in the x-direction and 34.9 ± 0.5 mPa.s in the y-direction (see Figure 3-4). Below we discuss the possible origins of these differences in the apparent viscosities experienced by the microparticles and nanoparticles at the interface of the LC.

First, we considered it possible that the differences in apparent viscosities experienced by the nanoparticles and microparticles simply reflected differences in the relative locations of the

particles at the LC interface (*e.g.*, a smaller fraction of the surface area of the nanoparticles may contact the aqueous phase, as compared to the microparticles). To investigate this possibility, we measured the contact angle of 5CB under 0.1 M aqueous sodium perchlorate on a gold surface functionalized with the mixed organothiol monolayer. The measured value of the contact angle (27˚ ± 4˚, the error bars representing the range of values between an expanding and receding droplet of 5CB) was found to be similar for isotropic and nematic 5CB and used to calculate the drag coefficient of the gold nanoparticles at the isotropic 5CB interface. The drag coefficient was calculated to be $f = 0.72$, a value that is slightly higher than for the microparticles ($f = 0.68$, see above). This difference in drag coefficient leads to a calculated difference of ~3.5 mPa.s in the apparent viscosity experienced by the micro- and nano-particles at the interface of isotropic 5CB, a value that is much smaller than the difference of 21.9 ± 2.0 mPa.s measured in our experiments (see Figure 3-4). Although this calculation is performed for the interface of isotropic 5CB, it does suggest that small differences in the locations of the nanoparticles and microparticles at the LC-aqueous interface appear unlikely to explain the large differences measured in apparent viscosities experienced by the micro- and nano-particles at the LC interface.

We also considered the possibility that the above observations could be due to the different surface compositions of the microparticles and nanoparticles which can affect the anchoring energy of 5CB at the particle surface. We measured the diffusion coefficient of 150 ± 2 nm silica particles with a DMOAP monolayer in bulk 5CB. For motion perpendicular to the far-field director, we measured an apparent viscosity of 48.8 ± 7.3 mPa.s which are similar to the result reported by Koenig *et al.* (32) for 169 ± 12 nm gold nanoparticles with a mixed component monolayer of 58.9 ± 1.1 mPa.s. Both results are much less than apparent viscosities reported by Stark *et al.* (52) for particles with Saturn ring defects in bulk 5CB of 85.3 mPa.s. We

conclude that the above observations are not due solely to differences between the surface compositions of the microparticles and the nanoparticles.

While the high apparent viscosity experienced by the nanoparticles at the interface might be an effect of an interfacial viscosity of the nematic 5CB-aqueous interface (see below; an interfacial viscosity of 14.0 ± 0.4 mPa.s.μm can reproduce the experimental measurements of the mobility of the nanoparticles functionalized with the mixed monolayers), here we note the surprising observation that the apparent viscosity experienced by the nanoparticles at the aqueous interface of the 5CB (both at 26°C and 40°C) almost coincides with measurements of the apparent viscosities experienced by nanoparticles in the *bulk* of the LC (when the direction of displacement of the particles relative to the far-field director is the same in the two environments). For example, when the nanoparticles functionalized with the mixed monolayer diffuse perpendicular to the far-field director at the aqueous interface (y-direction), the apparent viscosity experienced by the nanoparticles is 59.1 ± 1.7 mPa.s. In bulk 5CB, the apparent viscosity experienced by similarly sized nanoparticles (diffusing perpendicular to the director) is 58.9 ± 1.1 mPa.s, a value that is not significantly different from the apparent viscosity at the 5CB-aqueous interface (32). While we initially viewed this agreement between apparent viscosities experienced by the nanoparticles in the bulk and interfacial environment to be fortuitous (or erroneous, see below), several additional results described later in this chapter show a similar correlation between the bulk and interfacial mobility of nanoparticles.

We note that we considered the possibility that the above-mentioned correlation between bulk and interfacial diffusion of nanoparticles was an artifact of accidental tracking of nanoparticles that were not, in fact, at the interface of the LC but actually located in the bulk of the LC film. Our experimental observations are, however, inconsistent with this possibility.

Specifically, all of the nanoparticles characterized in our study were observed to diffuse in the same focal plane as the surface of the gold grid (the location of the aqueous-LC interface). The depth of field of the objective used in our experiments was 400 nm, which allowed us to determine that the particles were within 110 nm of the interface. This latter conclusion was based on use of a scratched glass slide that was spin-coated with a 110 nm-thick layer of polystyrene and then decorated with 141 ± 11 nm-diameter gold particles. The particles and the scratches were observed to come into focus separately. Thus, if two objects come into focus simultaneously, as we observed for the particles and the gold grid, they lie less than 110 nm apart (in z-direction). In addition, we comment that for a nanoparticle to be dispersed in the bulk of the LC in our experimental set-up, it would need to pass across the aqueous-LC interface. We estimate that desorption of a nanoparticle from the aqueous-LC interface to involve an energetic penalty of (~10^7 kT), making it very unlikely.

Effect of Chemical Functionality of Nanoparticles on Diffusion at the Aqueous-LC Interface

Past studies of the diffusion of gold nanoparticles functionalized with organothiol monolayers in bulk 5CB have reported that the chemical functionality of the nanoparticles impacts the mobility of the particles. (32). Specifically, for nanoparticles diffusing perpendicular to the far-field director of bulk 5CB, the apparent viscosity experienced by nanoparticles functionalized with mixed monolayers (that cause perpendicular anchoring at macroscopic surfaces) was higher (58.9 ± 1.1 mPa.s) than for nanoparticles functionalized with single-component monolayers (which cause planar anchoring at macroscopic surfaces; 39.2 ± 0.5 mPa.s) (52). These results indicate that the local ordering of 5CB about a gold nanoparticle is influenced by the chemical functionality of the surface of the nanoparticle.

To explore the effects of the chemical functionality of gold nanoparticles on diffusion at aqueous-LC interfaces, we performed measurements with nanoparticles functionalized with the same two types of monolayers used in the above-described past measurements in bulk LC (again with parallel anchoring of the LC at the aqueous interface) (Figure 3-5). For displacements in the x-direction, we measured the diffusion coefficient of the nanoparticles with single component monolayers to be 0.111 ± 0.002 $\mu m^2/s$, and thus significantly higher than for nanoparticles with mixed monolayers (as reported above, 0.0715 ± 0.0020 $\mu m^2/s$). Similar conclusions were reached for diffusion perpendicular to the director (y-direction) at the planar 5CB-aqueous interface (see Figure 3-5). While the differences in the chemical functionality of the nanoparticles can, in principle, lead to changes in their location at the aqueous-LC interface, for the nanoparticles with the two chemical functionalities reported above, we conclude that this effect on mobility is negligible. Specifically, our measurement of the contact angles of 5CB on the mixed organothiol monolayer and the single component organothiol monolayer immersed in an aqueous phase yielded indistinguishable results (see above for values). Thus, we do not believe that differences in the locations of the two types of chemically functionalized nanoparticles at the LC-aqueous interface underlie the above-reported differences in mobility.

We interpret the results described above to indicate that, similar to bulk 5CB, that the diffusion of the nanoparticles at the interface of the LC is influenced by local ordering of the LC that is dependent on the chemical functionality of the nanoparticles. Perhaps more significant, however, is the observation again (see comments above) of almost quantitative agreement between diffusion coefficients of the nanoparticles in the bulk and at the interface of the LC. Thus, we observe the correspondence between bulk and interfacial diffusion for nanoparticles that are functionalized with either the single component or the mixed monolayers. This result

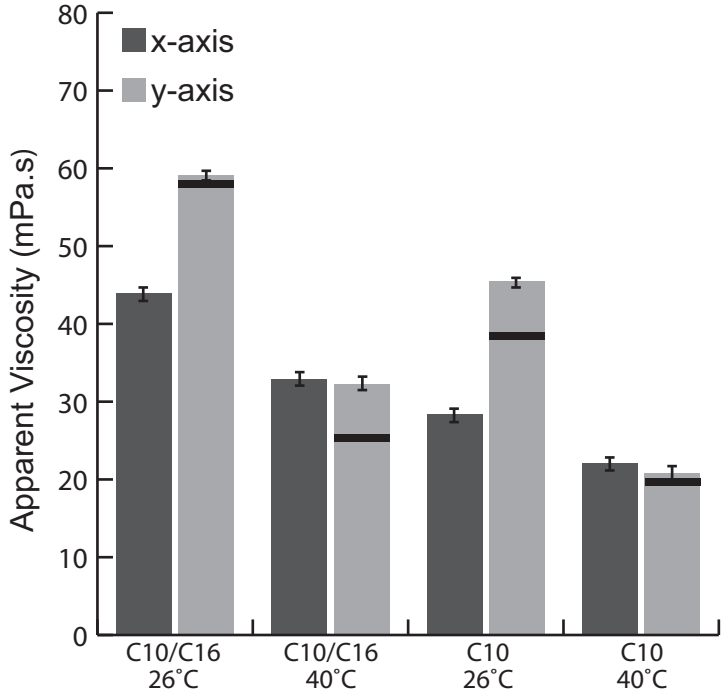


Figure 3 - 5. Influence of chemical functionality of gold nanoparticles on bulk and interfacial diffusion. The nanoparticles were functionalized with either a mixed monolayer of decanethiol and hexadecanethiol (C10/C16), or a monolayer formed from decanethiol (C10). The vertical bars indicate interfacial diffusion coefficients. The horizontal lines indicate diffusion coefficients measured in bulk 5CB, as reported by Koenig *et al.* (32)

suggests that the rheological environment of the nanoparticles in the bulk of the LC and at the interface is similar. This correspondence contrasts to our measurements of interfacial and bulk mobilities for microparticles (Figure 3-3).

As also shown in Figure 3-5, when we heated the system to 40˚C to cause the bulk phase of 5CB to become isotropic, we measured the influence of the chemical functionality of the nanoparticles on their mobility to persist. We make two observations regarding these results. First, the diffusion coefficients of the nanoparticles (diameters of 141 ± 11 nm) with the mixed monolayers reveal that they behave hydrodynamically at the interface as if they were diffusing with a diameter of approximately 200 ± 5 nm (calculated using the viscosity of bulk, isotropic 5CB and the formalism of Danov *et al.*) (18). Although it is possible that the slow diffusion of the nanoparticle with the mixed monolayer at the interface of the isotropic 5CB is caused by the effects of an interfacial viscosity, we note that we would expect an effect of interfacial viscosity on the nanoparticles to be seen with both mixed monolayers and single component monolayers. Our results, as shown in Figure 3-5 do not support this conclusion (see below for additional discussion of this result). Specifically, we calculate the hydrodynamic size of the nanoparticles with the single component monolayer to be 136 ± 5 nm (indistinguishable from the physical size of the nanoparticles: 141 ± 11 nm). Second, similar to the general observations reported above, we note that the diffusion coefficients of the nanoparticles at the interface of the *isotropic* 5CB are largely indistinguishable from the diffusion coefficients measured in the bulk, *isotropic* phase of 5CB (Figure 3-5).

We end this section by noting that several theoretical studies have considered the motion of nanoparticles at isotropic liquid interfaces (23, 24). Song *et al.* have simulated the mobility of nanometer-sized particles at a polydimethylsiloxane-water interface (23). They find that the

mobility of a nanoparticle at the interface is independent of the particle's location on the interface. Our results at the aqueous-5CB interface appear to share some of these general conclusions.

Influence of the Anchoring of the LC at the Aqueous Interface on Nanoparticle Mobility

The results reported above were obtained with 0.1M sodium perchlorate in the aqueous solution, conditions that give rise to parallel anchoring of 5CB at the aqueous interface. In this section, we report the effect of a change in anchoring of the LC *at the aqueous interface* (from parallel to perpendicular) on the particle mobility. Whereas our past studies employed surfactants to induce ordering transitions at the aqueous-LC interface (15, 36), surfactants can also change the contact angle of the two phases on the particle surface, and thus potentially lead to effects that extend beyond a change in surface anchoring at the aqueous interface. For these reasons, in the experiments reported below, we employed aqueous solutions containing high concentrations of sodium perchlorate to achieve homeotropic anchoring of the LC at the aqueous interface. In a future study, we will report a detailed study of the effects of high salt concentrations on the orientational ordering of LCs at aqueous interfaces. For the experiments reported here, it is sufficient to note that the concentration of sodium perchlorate that was used to cause homeotropic anchoring was 8 M, and that such aqueous solutions possess a viscosity that is substantially higher than 0.1 M sodium perchlorate (4.37 mPa.s and 0.867 mPa.s at 26˚C, respectively).

Measurements of the apparent viscosities of nanoparticles (functionalized with either a single component monolayer or mixed monolayer) at the interface of nematic 5CB with perpendicular anchoring are shown in Figure 3-6. For each type of nanoparticle, a single apparent viscosity was measured at 26˚C, independent of the direction of translation of the

nanoparticle across the surface (data not shown). The absence of anisotropy in the measured diffusion coefficients of the nanoparticles at the interface is significant. Whereas the polarized light microscopy performed in transmission mode characterizes the orientational state of the entire LC film, the nanoparticles probe the ordering of the LC near the interface. Our nanoparticle diffusion measurements indicate that the homeotropic ordering of the LC persists from the bulk to within at least ~100 nm from the interface.

A comparison of the results shown Figure 3-6 and Figure 3-5 reveals the impact of the change in the orientation of the LC at the aqueous interface on the mobility of the particles. For nanoparticles with mixed monolayers, we measure the diffusion coefficients of the nanoparticles in the y-direction at the LC-aqueous interface with planar anchoring (see Figure 3-5) to be identical to the diffusion coefficient of the nanoparticles within the plane of the aqueous-LC interface with homeotropic anchoring (calculated from Figure 3-6 to be $0.0505 \pm 0.0011 mm^2/s$). In both cases, the nanoparticles are translating in a direction that is perpendicular to the far-field director. Interestingly, this diffusion coefficient is also indistinguishable from the diffusion coefficients of the nanoparticles measured in bulk 5CB for displacements perpendicular to the director (compare the left two bars in Figure 3-6). These results reinforce the generality of our observations regarding the similar mobilities of nanoparticles at aqueous interfaces of LCs and in bulk LC.

We also measured the apparent viscosity of the nanoparticles at the aqueous (8 M sodium perchlorate)-5CB interface at 40˚C (Figure 3-6). With 5CB in the bulk isotropic phase, we again measured the apparent viscosity experienced by the nanoparticles with the mixed monolayers at the interface to be substantially larger (32.2 ± 1.2 mPa.s) than the nanoparticles with the single component monolayers (22.5 ± 0.5 mPa.s). We make two observations regarding these results.

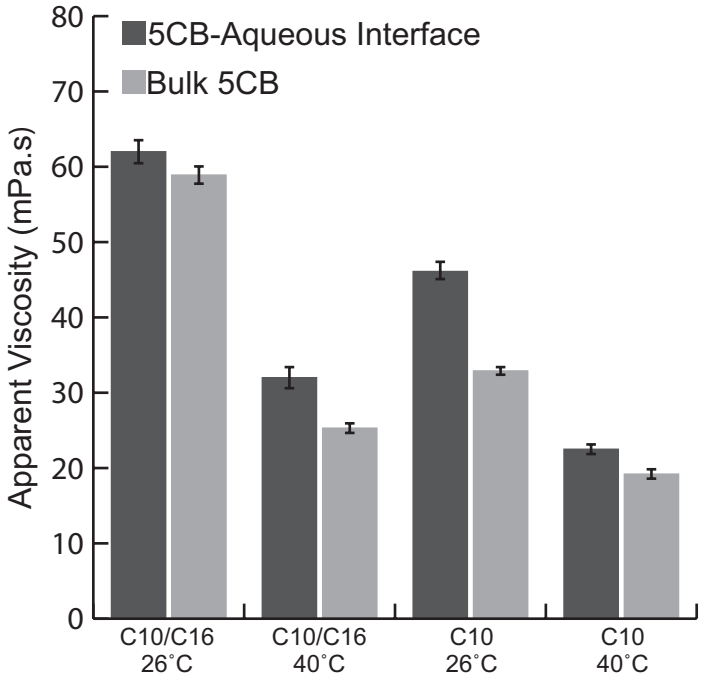


Figure 3 - 6. Comparison of bulk or interfacial apparent viscosities of gold nanoparticles (diameters of 169 ± 12 nm and 141 ± 11 nm, respectively) functionalized with mixed or single component monolayers. The interfacial diffusion coefficients were measured at a nematic 5CB–aqueous interface with homeotropic anchoring (at 26°C). The bulk diffusion coefficients from Koenig *et al.* (32) were measured for displacements perpendicular to the far-field director (at 26°C).

First, the magnitudes of the apparent viscosities in Figure 3-6 are indistinguishable from the values calculated from the data in Figure 3-5, corresponding to 5CB interfaces that exhibited planar anchoring of 5CB prior to heating to 40˚C. This result suggests that there is little residual ordering of the mesogens at *the aqueous interface of 5CB* when the 5CB is in the bulk isotropic state at 40˚C (no evidence of pre-nematic ordering at the aqueous interface) (53). Second, because the difference in physical size of the nanoparticles functionalized with the two types of monolayers is very small (<1 nm), the difference in apparent viscosities experienced by the two types of particles provides further support for our conclusion that there *exists residual ordering of the 5CB at the surface of the nanoparticles with the mixed monolayers*. Although prior observations of prewetting and smectic layering of mesogens at the surfaces of particles heated above the clearing temperature have been reported, these reports indicate that layers of only a few nanometers form at the surface (a thickness that is of the order of the nematic coherence length (53). However, to account for the above-mentioned difference in the diffusion coefficients of the nanoparticles chemically functionalized with the single-component or mixed monolayers at 40˚C, the 141 ± 11 nm diameter nanoparticles when functionalized with the mixed monolayers need to be assigned hydrodynamic diameters of 200 ± 5 nm, implying the presence of a layer of residual ordering of mesogens that is surprisingly large (~30 nm) as compared to previous reports (53). The origins of this large hydrodynamic diameter remain to be fully elucidated, and will be the subject of a future, detailed study. We do note, however, that past measurements of the localized surface plasmon resonances of gold nanoparticles that were chemically functionalized to promote homeotropic anchoring of 5CB also indicate the presence of residual ordering of 5CB at the gold surface at 40˚C (56).

Possible role of interfacial viscosity in experimental measurements at a 5CB-aqueous interface

We considered the possibility that the higher apparent viscosity experienced by the nanoparticles (relative to microparticles) was due to an interfacial viscosity, the effects of which will increase with a decrease in particle size (as discussed in the Introduction). Specifically, if we use the drag coefficient calculated above (f = 0.72), and viscosities experienced by the nanoparticles in bulk 5CB (47.0 ± 10.4 mPa-s and 63.3 ± 13.2 mPa-s in the x-direction and y-direction, respectively), we calculate that an interfacial viscosity of 14.0 ± 2.8 mPa.s.μm can reproduce the experimental measurements of the mobility of the nanoparticles functionalized with the mixed monolayers. A similar analysis for nanoparticles with the single component monolayers leads to the prediction of an interfacial viscosity of 15.7 ± 2.4 mPa.s.μm, a value which is indistinguishable from that inferred from the behavior of nanoparticles functionalized with the mixed monolayers.

Calculation of the adsorption energy of particles at the 5CB-aqueous interface

The relation between adsorption energy and interfacial tension can be determined from the following equation (Eq 8 from ref 35):

$$F' = -\frac{1}{4}\left(1 - h'^2\right) + \frac{1}{2}\cos\theta\,(1 - h') + \frac{1}{2}\tau\sqrt{1 - h'^2} \qquad (5)$$

where $F' = F/\gamma_{12}A_p$ is the reduced free energy. $h' = h/R$ is the reduced position on the interface. A_p is the surface area of the particle, γ_{12} is the interfacial tension between the two liquid phases, R is the particle radius, θ is the three phase contact angle and t is the line tension of the three-phase contact. The interfacial tension between 5CB and pure water has not been measured. Kim *et al.* (57), however, provide a lower bound from a pendent drop measurement (10 dyne/cm). There are no measurements of line tension for a 5CB-aqueous-silica system. Amirfazli *et al.* (58), however, present a review of line tensions for a variety of experimental

conditions. They find that both experimental and theoretical measurements for the line tension range from 10^{-10} N to 10^{-6} N for a variety of oil-aqueous-particle systems with the majority of systems being closer to 10^{-10} N. In this range, the effects of line tension on the location of the particle at the interface are negligible. The particle location at the interface is found by minimizing the free energy. The location is dependent on the three-phase contact angle, $h' = \cos\theta$. Based on an interfacial tension of 10 dyne/cm or greater, we calculate the free energy of adsorption to be at least ~10^7 kT.

3.5 Discussion

In summary, this chapter reports experimental measurements of the mobilities of microparticles and nanoparticles at the LC-aqueous interface, and highlights fundamental differences in the behaviors of the two classes of particles. The main conclusions of the study are three-fold. First, we have measured the mobilities of micrometer-sized particles at aqueous-LC interfaces to be higher than that in the bulk which we can understand on the basis of the location of the particles at the interface and bulk diffusion coefficients. Our results suggest that the ordering of the LC about the microparticle is substantially perturbed in the interfacial environment relative to the bulk, and that these differences in the configurations of the LC about the microparticles lead to low drag coefficients in the interfacial environment.

Second, we have measured the mobilities of nanoparticles at the LC-aqueous interface to differ in significant ways relative to the microparticles. A particularly interesting observation is that the diffusion coefficients of the nanoparticles at the LC-aqueous interface appear to be relatively insensitive to the details of the interfacial environment. Specifically, for displacements in the same direction relative to the far-field director of the LC, identical diffusion coefficients are measured at the interface and in bulk LC. Furthermore, when the 5CB is heated into the isotropic phase, the diffusion coefficients measured at the aqueous interface were indistinguishable from those measured in bulk 5CB. We emphasize that similar behaviors were not seen for microparticles, and that the relative insensitivity of the nanoparticles to the interfacial environment appears to be a property of the smaller particles studied in our experiments. Additional investigations are needed to understand the origins of the unexpected correspondence between surface diffusion and bulk diffusion of the nanoparticles.

A third significant conclusion is that the chemical functionality of the nanoparticles influences their interfacial diffusion at 40˚C, a temperature above the nematic-isotropic transition. Nanoparticles with a mixed organothiol monolayer were determined to have smaller interfacial diffusion coefficients than nanoparticles with single component monolayers. This suggests the presence of residual ordering of 5CB at the particle surface above the bulk phase transition (in the interfacial environment). While prenematic wetting has been reported previously at a number of interfaces, we estimate the hydrodynamic thickness of the prenematic layer to be ~30 ± 6 nm at a temperature 5˚C above the bulk clearing temperature, a value that is surprisingly large compared to the past reports (53).

3.6 References

1. Oettel M & Dietrich S (2008) Colloidal interactions at fluid interfaces. *Langmuir* 24(4):1425-1441.

2. Park BJ*, et al.* (2008) Direct measurements of the effects of salt and surfactant on interaction forces between colloidal particles at water-oil interfaces. *Langmuir* 24(5):1686-1694.

3. Onoda GY (1985) Direct Observation of Two-Dimensional, Dynamical Clustering and Ordering with Colloids. *Phys Rev Lett* 55(2):226-229.

4. Danov KD, Kralchevsky PA, Ananthapadmanabhan KP, & Lips A (2006) Particle-interface interaction across a nonpolar medium in relation to the production of particle-stabilized emulsions. *Langmuir* 22(1):106-115.

5. Lin Y, Skaff H, Emrick T, Dinsmore AD, & Russell TP (2003) Nanoparticle assembly and transport at liquid-liquid interfaces. *Science* 299(5604):226-229.

6. Tarimala S & Dai LL (2004) Structure of microparticles in solid-stabilized emulsions. *Langmuir* 20(9):3492-3494.

7. Kim B, Tripp SL, & Wei A (2001) Self-organization of large gold nanoparticle arrays. *J Am Chem Soc* 123(32):7955-7956.

8. Stein A & Schroden RC (2001) Colloidal crystal templating of three-dimensionally ordered macroporous solids: materials for photonics and beyond. *Curr Opin Solid St M* 5(6):553-564.

9. Velev OD & Kaler EW (2000) Structured porous materials via colloidal crystal templating: From inorganic oxides to metals. *Adv Mater* 12(7):531-534.

10. Meeker SP, Poon WCK, Crain J, & Terentjev EM (2000) Colloid-liquid-crystal composites: An unusual soft solid. *Phys Rev E* 61(6):R6083-R6086.

11. Anderson VJ & Terentjev EM (2001) Cellular solid behaviour of liquid crystal colloids - 2. Mechanical properties. *Eur Phys J E* 4(1):21-28.

12. Nazarenko VG, Nych AB, & Lev BI (2001) Crystal structure in nematic emulsion. *Phys Rev Lett* 87(7).

13. Smalyukh II*, et al.* (2004) Ordered droplet structures at the liquid crystal surface and elastic-capillary colloidal interactions. *Phys Rev Lett* 93(11).

14. Nych AB*, et al.* (2007) Coexistence of two colloidal crystals at the nematic-liquid-crystal-air interface. *Phys Rev Lett* 98(5).

15. Koenig GM, Lin IH, & Abbott NL (2010) Chemoresponsive assemblies of microparticles at liquid crystalline interfaces. *P Natl Acad Sci USA* 107(9):3998-4003.

16. Gharbi MA*, et al.* (2011) Behavior of colloidal particles at a nematic liquid crystal interface. *Soft Matter* 7(4):1467-1471.

17. Brenner H & Leal LG (1982) Conservation and Constitutive-Equations for Adsorbed Species Undergoing Surface-Diffusion and Convection at a Fluid Fluid Interface. *J Colloid Interf Sci* 88(1):136-184.

18. Danov K, Aust R, Durst F, & Lange U (1995) Influence of the Surface Viscosity on the Hydrodynamic Resistance and Surface Diffusivity of a Large Brownian Particle. *J Colloid Interf Sci* 175(1):36-45.

19. Petkov JT*, et al.* (1995) Measurement of the Drag Coefficient of Spherical-Particles Attached to Fluid Interfaces. *J Colloid Interf Sci* 172(1):147-154.

20. Anguelouch A, Leheny RL, & Reich DH (2006) Application of ferromagnetic nanowires to interfacial microrheology. *Appl Phys Lett* 89(11).

21. Sickert M & Rondelez F (2003) Shear viscosity of Langmuir monolayers in the low-density limit. *Phys Rev Lett* 90(12).

22. Lee MH, Reich DH, Stebe KJ, & Leheny RL (2010) Combined Passive and Active Microrheology Study of Protein-Layer Formation at an Air-Water Interface. *Langmuir* 26(4):2650-2658.

23. Song YM, Luo MX, & Dai LL (2010) Understanding Nanoparticle Diffusion and Exploring Interfacial Nanorheology using Molecular Dynamics Simulations. *Langmuir* 26(1):5-9.

24. Dhar P, Prasad V, Weeks ER, Bohlein T, & Fischer TM (2008) Immersion of charged nanoparticles in a salt solution/air interface. *J Phys Chem B* 112(32):9565-9567.

25. Zhang Z, Zheng DS, Guo Y, & Wang HF (2009) Water penetration/accommodation and phase behaviour of the neutral langmuir monolayer at the air/water interface probed with sum frequency generation vibrational spectroscopy (SFG-VS). *Phys Chem Chem Phys* 11(6):991-1002.

26. Delabre U, Richard C, & Cazabat AM (2009) Some specificities of wetting by cyanobiphenyl liquid crystals. *J Phys-Condens Mat* 21(46).

27. Takahashi K, Ichikawa M, & Kimura Y (2008) Direct measurement of force between colloidal particles in a nematic liquid crystal. *J Phys-Condens Mat* 20(7).

28. Skarabot M*, et al.* (2006) Laser trapping of low refractive index colloids in a nematic liquid crystal. *Phys Rev E* 73(2).

29. Chen XM, Hamlington BD, & Shen AQ (2008) Isotropic-to-nematic phase transition in a liquid-crystal droplet. *Langmuir* 24(2):541-546.

30. Kotar J*, et al.* (2006) Interparticle potential and drag coefficient in nematic colloids. *Phys Rev Lett* 96(20).

31. Ognysta U*, et al.* (2008) 2D interactions and binary crystals of dipolar and quadrupolar nematic colloids. *Phys Rev Lett* 100(21).

32. Koenig GM*, et al.* (2009) Single Nanoparticle Tracking Reveals Influence of Chemical Functionality of Nanoparticles on Local Ordering of Liquid Crystals and Nanoparticle Diffusion Coefficients. *Nano Lett* 9(7):2794-2801.

33. Poulin P, Stark H, Lubensky TC, & Weitz DA (1997) Novel colloidal interactions in anisotropic fluids. *Science* 275(5307):1770-1773.

34. Jerome B (1991) Surface Effects and Anchoring in Liquid-Crystals. *Rep Prog Phys* 54(3):391-451.

35. Bresme F & Oettel M (2007) Nanoparticles at fluid interfaces. *J Phys-Condens Mat* 19(41).

36. Brake JM, Daschner MK, Luk YY, & Abbott NL (2003) Biomolecular interactions at phospholipid-decorated surfaces of liquid crystals. *Science* 302(5653):2094-2097.

37. Lin IH, Koenig GM, de Pablo JJ, & Abbott NL (2008) Ordering of Solid Microparticles at Liquid Crystal-Water Interfaces. *J Phys Chem B* 112(51):16552-16558.

38. Musevic I, Skarabot M, Tkalec U, Ravnik M, & Zumer S (2006) Two-dimensional nematic colloidal crystals self-assembled by topological defects. *Science* 313(5789):954-958.

39. Gupta VK & Abbott NL (1997) Design of surfaces for patterned alignment of liquid crystals on planar and curved substrates. *Science* 276(5318):1533-1536.

40. Drawhorn RA & Abbott NL (1995) Anchoring of Nematic Liquid-Crystals on Self-Assembled Monolayers Formed from Alkanethiols on Semitransparent Films of Gold. *J Phys Chem-Us* 99(45):16511-16515.

41. Ruths M, Heuberger M, Scheumann V, Hu JJ, & Knoll W (2001) Confinement-induced film thickness transitions in liquid crystals between two alkanethiol monolayers on gold. *Langmuir* 17(20):6213-6219.

42. Gupta VK & Abbott NL (1996) Uniform anchoring of nematic liquid crystals on self-assembled monolayers formed from alkanethiols on obliquely deposited films of gold. *Langmuir* 12(10):2587-2593.

43. Lowe AM, Bertics PJ, & Abbott NL (2008) Quantitative methods based on twisted nematic liquid crystals for mapping surfaces patterned with bio/chemical functionality relevant to bioanalytical assays. *Anal Chem* 80(8):2637-2645.

44. Peng Y, Chen W, Fischer TM, Weitz DA, & Tong P (2009) Short-time self-diffusion of nearly hard spheres at an oil-water interface. *J Fluid Mech* 618:243-261.

45. Crocker JC & Grier DG (1996) Methods of digital video microscopy for colloidal studies. *J Colloid Interf Sci* 179(1):298-310.

46. Poulin P & Weitz DA (1998) Inverted and multiple nematic emulsions. *Phys Rev E* 57(1):626-637.

47. Loudet JC, Barois P, & Poulin P (2000) Colloidal ordering from phase separation in a liquid-crystalline continuous phase. *Nature* 407(6804):611-613.

48. Stark H (1999) Director field configurations around a spherical particle in a nematic liquid crystal. *Eur Phys J B* 10(2):311-321.

49. Gu YD & Abbott NL (2000) Observation of Saturn-ring defects around solid microspheres in nematic liquid crystals. *Phys Rev Lett* 85(22):4719-4722.

50. Hild R*, et al.* (1998) Formation and characterization of self-assembled monolayers of octadecyltrimethoxysilane on chromium: Application in low-energy electron lithography. *Langmuir* 14(2):342-346.

51. Tasinkevych M & Andrienko D (2010) Colloidal particles in liquid crystal films and at interfaces. *Condens Matter Phys* 13(3).

52. Stark H & Ventzki D (2001) Stokes drag of spherical particles in a nematic environment at low Ericksen numbers. *Phys Rev E* 64(3).

53. Bottger A, Frenkel D, Vanderiet E, & Zijlstra R (1987) Diffusion of Brownian Particles in the Isotropic-Phase of a Nematic Liquid-Crystal. *Liq Cryst* 2(4):539-547.

54. Stark H (2001) Physics of colloidal dispersions in nematic liquid crystals. *Phys Rep* 351(6):387-474.

55. Koenig GM, Jr., de Pablo JJ, & Abbott NL (2009) Characterization of the reversible interaction of pairs of nanoparticles dispersed in nematic liquid crystals. *Langmuir* 25(23):13318-13321.

56. Koenig GM, Gettelfinger BT, de Pablo JJ, & Abbott NL (2008) Using localized surface plasmon resonances to probe the nanoscopic origins of adsorbate-driven ordering transitions of liquid crystals in contact with chemically functionalized gold nanodots. *Nano Lett* 8(8):2362-2368.

57. Kim JW, Kim H, Lee M, & Magda JJ (2004) Interfacial tension of a nematic liquid crystal/water interface with homeotropic surface alignment. *Langmuir* 20(19):8110-8113.

58. Amirfazli A & Neumann AW (2004) Status of the three-phase line tension: a review. *Adv Colloid Interface Sci* 110(3):121-141.

Chapter 4

Optically-Excited Changes in Nanoparticle Solvation

4.1 Abstract

The structuring of solvent molecules near nanoparticles and macroscopic interfaces influences equilibrium and dynamic phenomena that underlie the transport, optical, tribological and catalytic properties of materials. Here we reveal light-induced changes in the solvation of metallic nanoparticles by performing measurements of the hydrodynamic drag experienced by the nanoparticles during motion through a solvent. Specifically, by choosing temperatures that place isotropic solvents within 5˚C of phase transitions to ordered liquid phases, and by tracking the motion of single-nanoparticles undergoing Brownian diffusion, we measure optically-induced changes in solvation of surface-functionalized gold nanoparticles (diameters of 85±7 nm and 164±11 nm) to occur in a wavelength-specific and nanoparticle size-dependent manner, and to result in increases in hydrodynamic diameters of up to 54±12 nm. A range of experiments and calculations designed to test hypotheses regarding the underlying mechanism, including the effects of optical pressure, surface plasmon resonances and hot electrons, support the proposal that an ordered solvent corona is induced by interfacial electric fields generated by optically-induced hot electron-hole pairs. We confirm solvent restructuring induced by hot electron-hole pairs by measuring changes in the surface plasmon resonances of macroscopic gold-covered surfaces. Overall, these results suggest new principles for optical manipulation of the interfacial ordering of solvents.

4.2 Introduction

The central role of solvation in determining the structure and functional properties of natural and synthetic materials has motivated many past efforts aimed at understanding and altering solvation. Typical approaches have involved the addition of salts (1) or non-ionic solutes (2, 3) (e.g., sucrose) to water, or manipulation of the temperature (4) or pressure (5) of aqueous systems. The resulting changes in solvation were evidenced by measurements of transport properties (1, 6) (e.g., hydrodynamic size), changes in macromolecular structure (2, 4), or altered catalytic activities of inorganic nanoparticles (3). More recently, studies of solvation have moved to consider non-aqueous systems (7), and have also employed synchrotron-based x-ray methods (8), non-linear optical methods (9), theory and simulation (10) to characterize solvent structuring at the interfaces of soft and hard materials. Of particular relevance to our study, the hydration of metal interfaces have been shown to be influenced by manipulation of the electrical potential of the metal (8).

In this paper, we go beyond these past studies by reporting the finding that optical excitation of metals can change interfacial solvation. The results hint at the basis of facile methods for achieving reversible and spatially-localized changes in solvation-dependent properties. We focus on ligand-capped gold nanoparticles dispersed in polar organic solvents, but the mechanisms established by our investigation appear generally applicable to other metals and solvents.

4.3 Results

In our initial experiments, we measured the Brownian diffusion of gold nanoparticles with physical diameters (as determined by electron microscopy) of 164±11 nm (Figure 4-1a) or 85±7 nm (Figure 4-1b) dispersed in an isotropic liquid phase of 4-*n*-pentyl-4'-cyanobiphenyl (5CB; Figure 4-1d). We chose to perform our measurements in the isotropic phase of 5CB at temperatures ranging from 36˚C to 44˚C because 5CB forms an ordered liquid phase (a nematic liquid crystal characterized by long-range orientational ordering of the 5CB molecules) below 35°C. By performing measurements within 9˚C of the phase transition, we sought to maximize the effects of changes in interfacial solvent structure on the hydrodynamic sizes of the nanoparticles. The surfaces of the gold nanoparticles used in our experiments were chemically functionalized with either a mixed monolayer formed from hexadecanethiol (C16SH) and decanethiol (C10SH) (Figure 4-1f) or a single-component monolayer formed from C10SH (Figure 4-1g). The monolayers were formed at 50˚C to achieve the thermal stability needed for the experiments reported in this paper (see Methods Section). We used dark-field microscopy to track the motion of individual gold nanoparticles (11). The focal plane of the microscope was located at least 10 μm from either of the confining surfaces of the optical cell to ensure that the mobility of the nanoparticles was not influenced by hydrodynamic interactions with confining surfaces.

Figure 4-2a shows two representative trajectories of gold nanoparticles (diameters of 164±11 nm with surfaces functionalized with the mixed monolayer) measured in 5CB at either 36˚C or 44˚C (1˚ and 9˚C, respectively, above the temperature at which 5CB transformed from an isotropic to nematic phase (T_{NI})). Our initial measurements were performed using white light from a halogen lamp. We used trajectories of the type shown in Figure 4-2a to calculate the

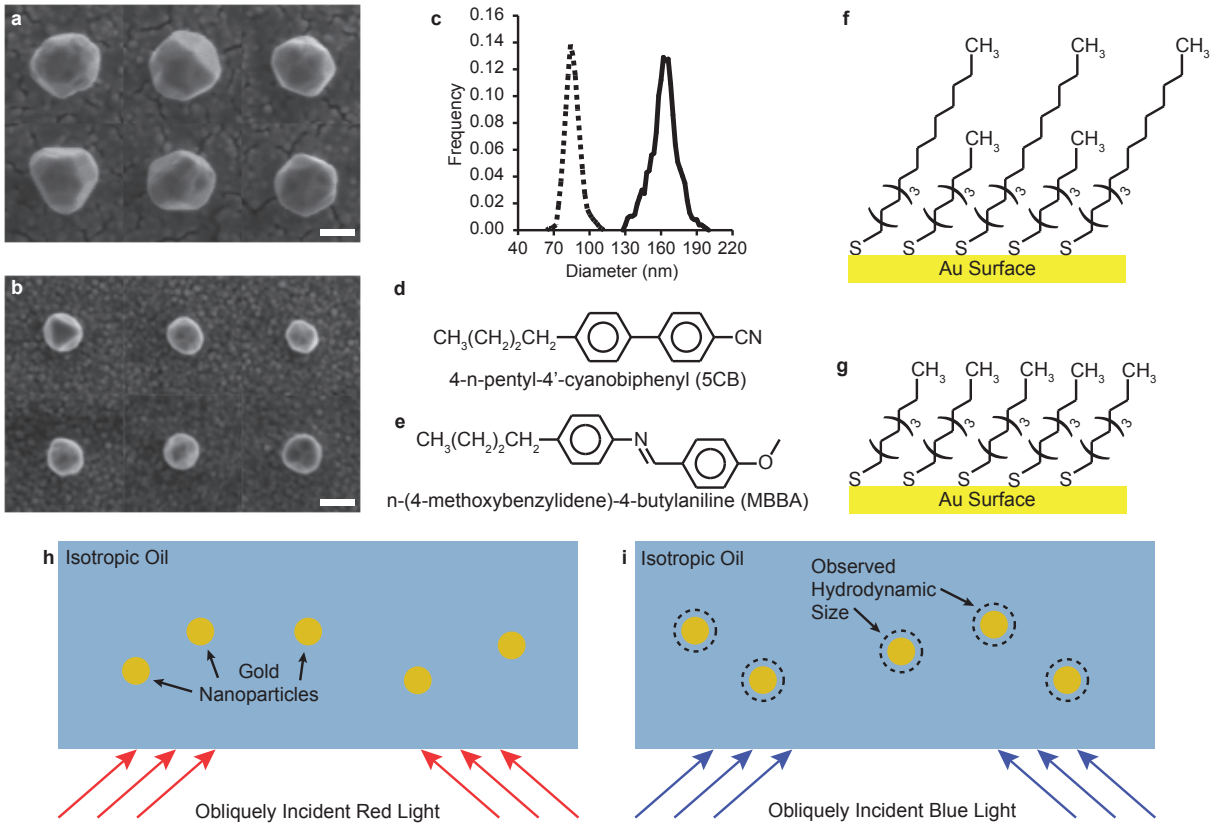


Figure 4 - 1. Schematic illustration of experimental setup. (a) Scanning electron micrographs of gold nanoparticles with diameters of 164±11nm or (b) 85±7 nm. (c) Normalized histogram of diameters of 400 nanoparticles with average sizes of either (solid line) 164±11 nm or (dotted line) 85±7 nm. Molecular structures of oils used in this study: (d) 5CB and (e) MBBA. Schematic illustration of monolayers formed on the surfaces of gold nanoparticles from (f) C10SH and C16SH or (g) C10SH. (h) and (i) show schematic illustrations of the illumination of gold nanoparticles. At a temperature 1˚C above the T_{NI}, when illuminated with a 650±20 nm light source (h), the gold nanoparticles diffuse with a hydrodynamic size approximately equal to their physical size. When illuminated with a 450±20 nm light (i), the gold particles diffuse with a hydrodynamic size that is 40 nm larger than their physical size.

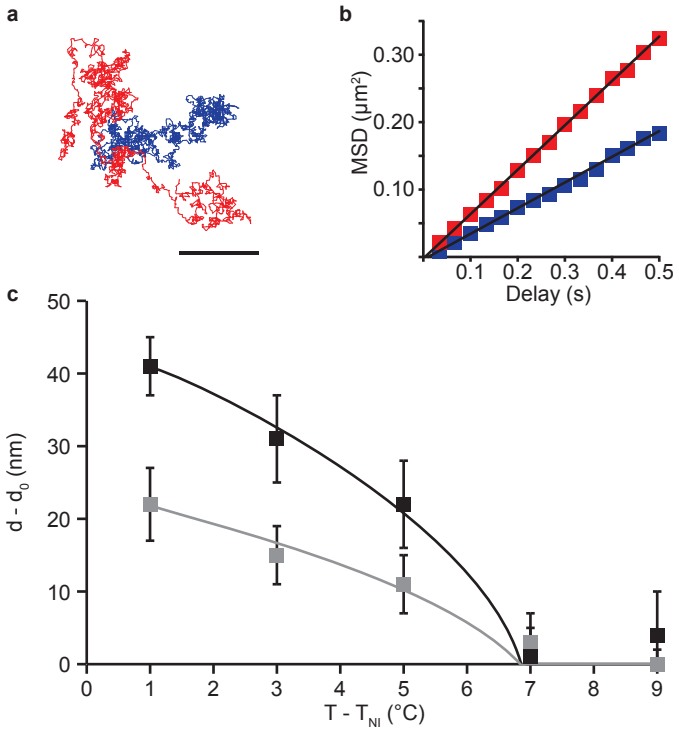


Figure 4 - 2. Measurements of hydrodynamic sizes of gold nanoparticles. (a) Representative trajectories of single gold nanoparticles (gold core diameter of 164±11 nm; surfaces functionalized with a mixed monolayer of decanethiol and hexadecane thiol) tracked at either (blue) 36˚C (1˚C above T_{NI}) or (red) 44˚C (9˚C above T_{NI}) over a duration of 180 s. (b) Mean squared displacement (MSD) versus time delay for trajectories shown in (a). A linear least-squares fit (solid line) to the data is shown. (c) The difference between the hydrodynamic diameter, d, and physical diameter, d_0, of gold nanoparticles (d_0 = 164±11 nm) functionalized with a mixed component thiol monolayer (black) or a single component thiol monolayer (grey) at various temperatures above the bulk nematic-to-isotropic phase transition temperature of 5CB (T_{NI} = 35˚C). Hydrodynamic diameter measurements were obtained using 40-50 particle trajectories from 3 independent samples. Data show mean ± s.e.m. Lines are drawn to guide the eye.

diffusion coefficients of the nanoparticles by determining the mean squared displacement (MSD; Figure 4-2b) for time steps ranging from 0.03 s to 0.5 s. We note that the absence of convection or stage drift was confirmed by measuring the same MSDs in orthogonal directions within the sample. A linear least-square fit was applied to the MSDs as a function of time delay to calculate the diffusion coefficient, D, as $D = MSD/2\tau$, where τ is the delay time between displacement measurements. The hydrodynamic diameter of each nanoparticle, d, was calculated from the diffusion coefficient using the Stokes-Einstein equation ($d = kT/3\pi\eta D$, where k is the Boltzmann constant and η is the viscosity of the bulk solvent) as a function of the temperature of the solvent (Figure 4-2c). Inspection of Figure 4-2c reveals that at 44˚C (9˚C above T_{NI}), the hydrodynamic diameters of the nanoparticles were measured to be indistinguishable from their physical diameters (d_0). As the temperature of the solvent decreased to 36˚C (1˚C above T_{NI}), however, the hydrodynamic diameters of the nanoparticles increased by 41±4 nm. Nanoparticles functionalized with the single-component monolayers (also shown in Figure 4-2c) exhibited an increase in hydrodynamic diameter of 22±5 nm upon cooling from 9˚C to 1˚C above T_{NI}, revealing that the temperature-dependent increase in hydrodynamic size is dependent on the chemical functionality of the nanoparticle surface. We note that the above-described changes in hydrodynamic sizes were found to be reversible over multiple heating or cooling cycles of the system.

To provide insight into the above observations, next we varied the wavelength of light used to illuminate and track the motion of the nanoparticles. For 164±11 nm-diameter gold nanoparticles illuminated with blue light (450 nm, full width at half maximum (FWHM) = 40 nm), we measured the hydrodynamic diameters of the nanoparticles to exceed their physical diameters in a manner that was statistically indistinguishable from that measured using white

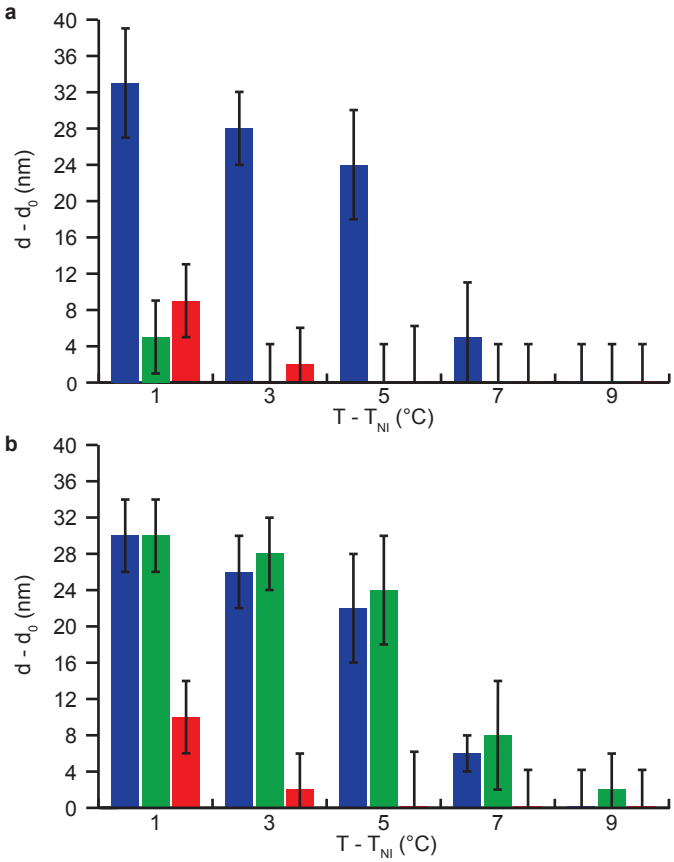


Figure 4 - 3. Difference between the hydrodynamic diameter, d, and physical diameter, d_0, of gold nanoparticles with (a) d_0 = 164±11 nm and (b) d_0 = 85±7 nm, when illuminated with either a blue, green, or red light source, as represented by the color of the bars at various temperatures above the bulk clearing temperature of 5CB, T_{NI} (35˚C). Hydrodynamic diameters were measured using 40-50 particle trajectories obtained from 3 independent samples. Data show mean ± s.e.m.

light (Figure 4-3a). In contrast, when illuminated with red (650 nm, FWHM = 40 nm) or green light (550 nm, FWHM = 40 nm), the hydrodynamic sizes of the nanoparticles were measured to be the same as the physical size at all temperatures except at 36˚C (T - T_{NI} = 1˚C) where a small increase of 9±4 nm was observed. Significantly, and in contrast to the larger gold nanoparticles, we measured the effects of green and blue light to have similar effects on the hydrodynamic diameters of the smaller nanoparticles (e.g. at 1˚C above T_{NI}, the hydrodynamic diameter was ~30 nm greater than the physical diameter) whereas the red light had little effect on the hydrodynamic size. These results, when combined, led us to conclude that illumination was influencing the hydrodynamic sizes of the gold nanoparticles in a manner that was dependent on both the wavelength of illumination and the physical size of the gold core of the nanoparticles. We emphasize again that the effects of illumination shown in Figure 4-3 are reversible (e.g., a change in wavelength of illumination leads to a reversible change in hydrodynamic size).

We measured qualitatively similar effects of illumination on the diffusion of the gold nanoparticles in isotropic phases of n-(4-methoxybenzylidene)-4-butylaniline (MBBA), indicating that the phenomenon is not limited to 5CB (See Section 4.6). We also measured the solvation layer thickness using red light and chemically-functionalized gold nanoparticles to be, within the experimental error of the measurement, indistinguishable from the thicknesses of the prenematic wetting layers measured on the surfaces of silica particles (5±2 nm for the gold nanoparticles and 3 nm for the silica particles) (12, 13). We also performed control experiments using red, green and blue light and silica nanoparticles with diameters of 391±35 nm (functionalized with a monolayer of dimethyloctadecyl[3-trimethoxysilyl)propyl]ammonium chloride (DMOAP)) and found that the wavelength of illumination did not change the hydrodynamic diameters of the silica nanoparticles (see Section 4.6). Overall, these results

support our proposal that the solvation of the gold nanoparticles can be influenced by illumination.

The effects of temperature and illumination described above are reversible and thus not consistent with optically-induced changes in the surface chemistry of the nanoparticles nor thermal desorption of the monolayers (see Section 4.7). In addition, any effects of local heating (14) (due to the absorption of light) would cause a decrease in viscosity of the solvent near the nanoparticles and thus a decrease in hydrodynamic size. This trend is opposite to that measured in our experiments. Gold nanoparticles are known, however, to possess local surface plasmon resonances (LSPR) that couple to specific wavelengths of light to generate interfacial electric fields. We hypothesized that these interfacial fields may influence the ordering of the 5CB solvent around the nanoparticles (15). The resonant wavelength of light that couples to the LSPR of nanoparticles is dependent on the size, shape, and composition of the nanoparticles as well as the dielectric constant of the surrounding medium. Previous studies have suggested that electric fields associated with LSPR generated by assemblies of gold nanoparticles can affect the bulk orientations of nematic liquid crystals (16). We therefore tested the hypothesis that interfacial electric field generated by the LSPR may be sufficient in strength and range to induce 5CB and MBBA into an organized solvent corona about gold nanoparticles.

To test this hypothesis, we calculated the wavelengths of light that excite LSPRs in the nanoparticles and the associated interfacial electric field strengths by using the discrete dipole approximation (DDA) (17) (see Methods Section). To validate our calculation, first we compared the calculated and measured extinction of light by the gold nanoparticles. A comparison of Figure 4-4a to 4-4b reveals the calculations and measurements to be in good agreement, with the 85±7 nm gold nanoparticles exhibiting a single LSPR peak arising from a dipolar resonance

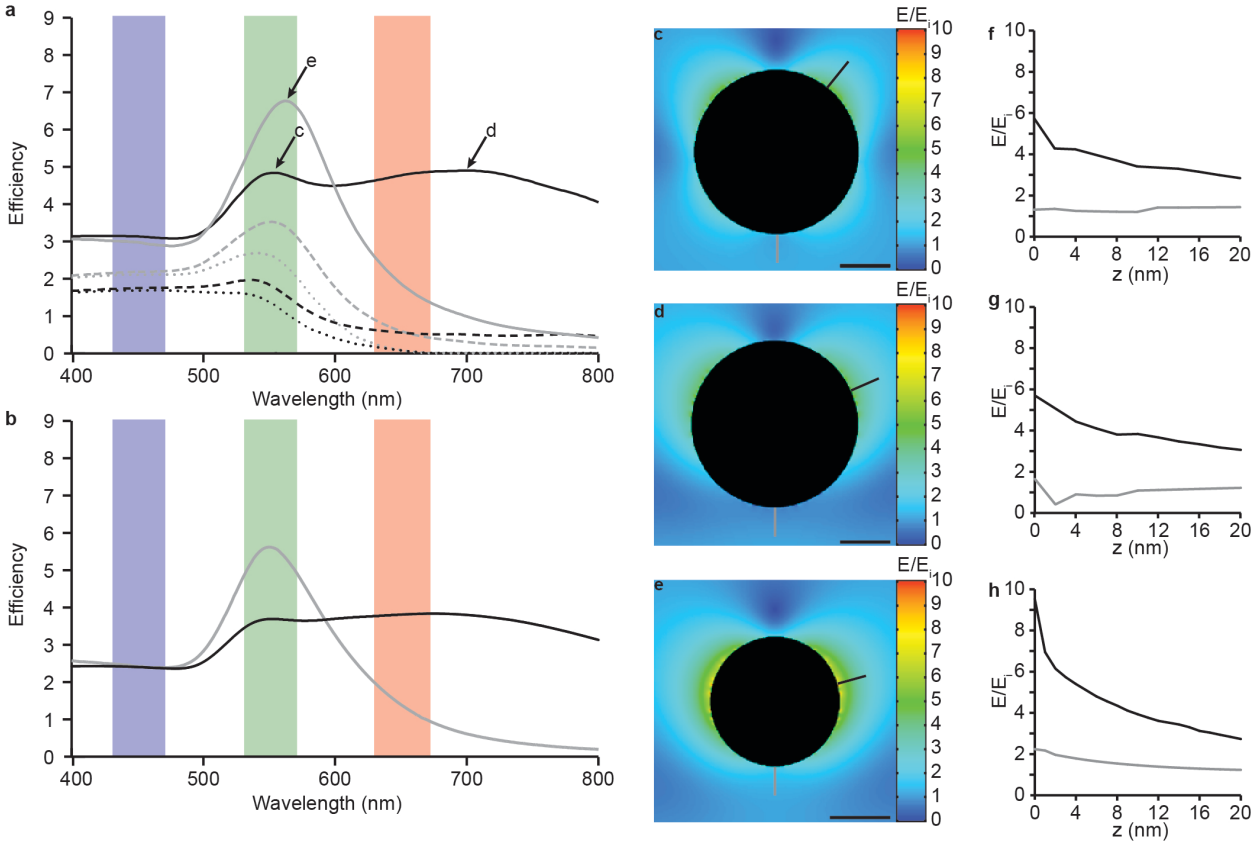


Figure 4 - 4: Calculations and measurements of the optical properties of gold nanoparticles. (a) The calculated extinction (solid line) and absorption (dashed) efficiencies of (black) 164 nm and (grey) 85 nm diameter gold particles in a medium of refractive index 1.39, the isotropic refractive index of 5CB at the bulk clearing temperature. The blue, green, and red bars indicate the range of wavelengths of light transmitted though the bandpass filters used in our experiments. The width of the line represents the FWHM of the distribution of light transmitted by the filter. The calculated efficiency of excitation of hot electrons (dotted) by light is also plotted (See Section 4.9). (b) The measured extinction efficiency of (black) 164±11 nm-diameter and (grey) 85±7 nm-diameter gold nanoparticles with a mixed component thiol monolayer obtained. The extinction efficiency was calculated from optical density measurements performed in 95% 5CB - 5% ethanol using the method described by Fernig *et al.* (18). Optical density measurements are the average of 2 independent samples. (c-e) Cross-section of the electric field enhancement (E/E_i) at the resonance frequencies indicated by the arrows in (a). The light source is incident from the top of the image and is polarized in the plane of the page. The scale bar is 40 nm. The black circles are superimposed to indicate the location of the particle. (f-h) Electric field enhancement as a function of distance from the particle surface drawn perpendicular to the surface for the calculations shown in c-e, respectively. The black line indicates a trace that passes though the point of maximum electric field enhancement at the particle surface and is indicated by the black trace in c-e. The grey line passes though the point of minimum electric field enhancement at the particle surface and is indicated by the grey trace in c-e. Optical density measurements are the average of 2 independent samples.

(experiment 550±1 nm; DDA calculation 564 nm). The 164±11 nm gold nanoparticles, in contrast, exhibit peaks due to both dipolar (experiment 673±1 nm; DDA calculation 700 nm) and quadrupolar resonances (experiment 555±1 nm; DDA calculation 554 nm). We make two observations regarding the results in Figure 4-4. First, inspection of Figure 4-4 reveals the absence of a LSPR (i.e., no interfacial electric field enhancement) when using blue light (light from 400 nm to 520 nm; additional evidence is provided in Figure 4-5 and 4-6). Whereas the measurements in Figure 4-3 clearly show that blue light causes an increase in hydrodynamic size of the nanoparticles. Second, although it initially seemed possible to us that the differential effects of green light on the small (increase in hydrodynamic size of 30±8 nm) and large (no change in hydrodynamic size) nanoparticles were the result of size-dependent differences in the LSPRs of the nanoparticles, we tested this possibility by calculating the electric field enhancement arising from LSPRs (Figure 4-5 to 4-7) at wavelengths ranging from 400 nm to 800 nm. For 164 nm-diameter nanoparticles at 554 nm (green light and the quadrupolar resonance frequency), the maximum local electric field enhancement (E/E_i, where electric field of the incident light source is E_i) is 6. For the 85 nm-diameter nanoparticles at 564 nm, a wavelength of light that launches a dipolar resonance, we observe a maximum field enhancement of 10 at the nanoparticle interface. We used these field enhancements to calculate (see Section 4.8 for details) the effects of the local electric field on solvent order, S(z), using

$$S(z) = \frac{S_0}{\gamma_s+1} e^{-\frac{z}{\xi_N}} + \frac{\gamma_E \xi_N^2 \xi_E^2 E_0^2}{\xi_E^2 - 4\xi_N^2}\left(e^{-2\frac{z}{\xi_E}} - \frac{1}{\gamma_s+1}\left(\frac{2\gamma_s\xi_N}{\xi_E}+1\right)e^{-\frac{z}{\xi_N}}\right) \quad (1)$$

where S(z) is the scalar order parameter of the solvent at distance z from the surface, evaluated as $S(z) = \frac{1}{2}\langle 3\cos^2(\theta) - 1\rangle$, and θ is defined as the angle between the long axis of a particular mesogen and the average direction of the molecular long axes of the ensemble of mesogens. On the right side of Eq. 1, S_0 is the order parameter at z = 0, $\gamma_s = L_1/\xi_N W_s$ where ξ_N is the nematic

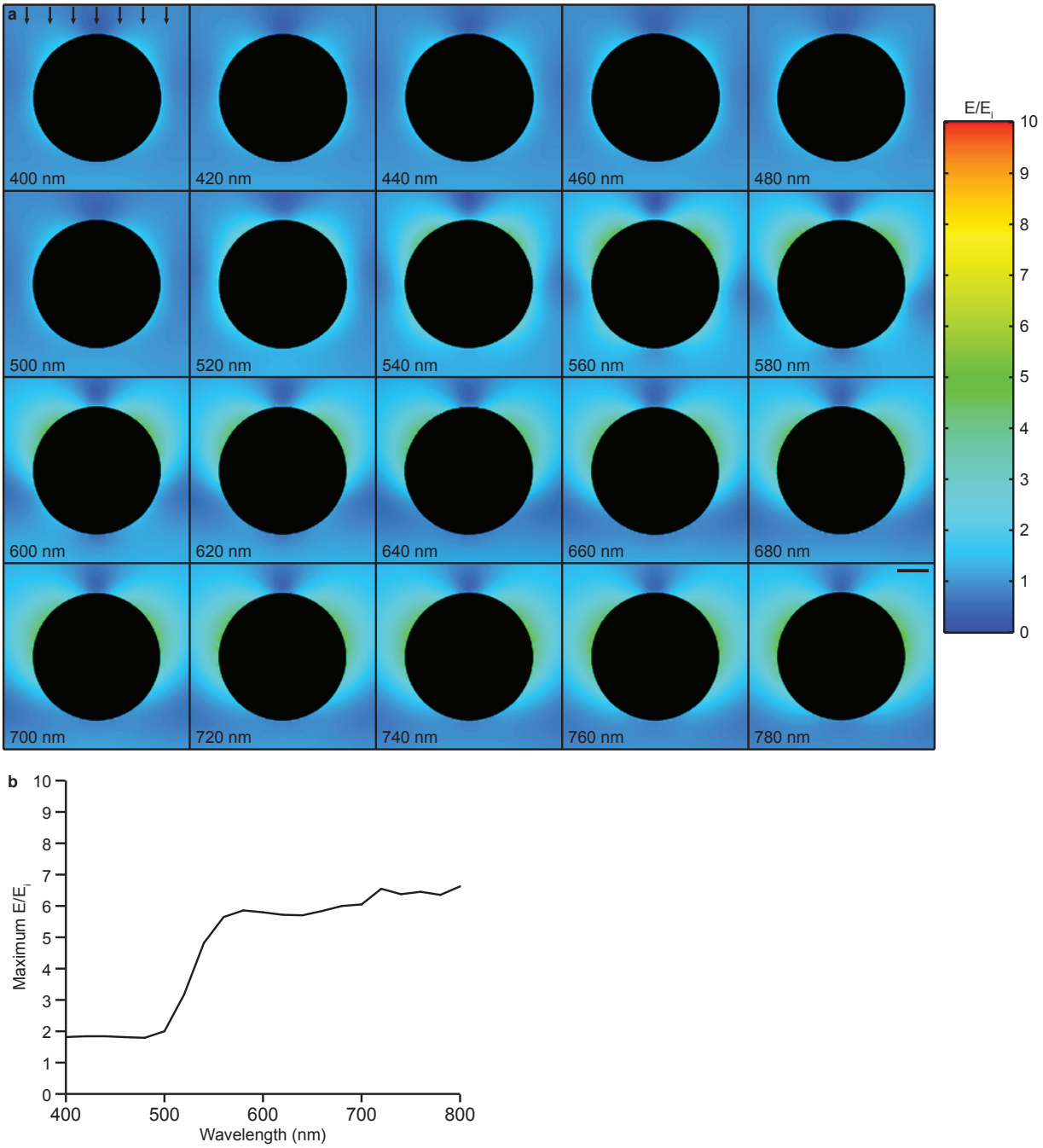


Figure 4 - 5. Electric field enhancement near gold nanoparticles at various wavelengths of illumination. (a) Cross-section of local electric field enhancement (E/E_i) for 164 nm diameter gold particles illuminated by light with various wavelengths from 400 nm to 780 nm in a medium with refractive index 1.39. The scale bar is 40 nm. The black circles are superimposed to indicate the location of the particle. The light propagates from the top of each panel and is polarized in the direction of the page. (b) Peak value of the electric field enhancement calculated at the particle surface at various wavelengths from 400 nm to 800 nm.

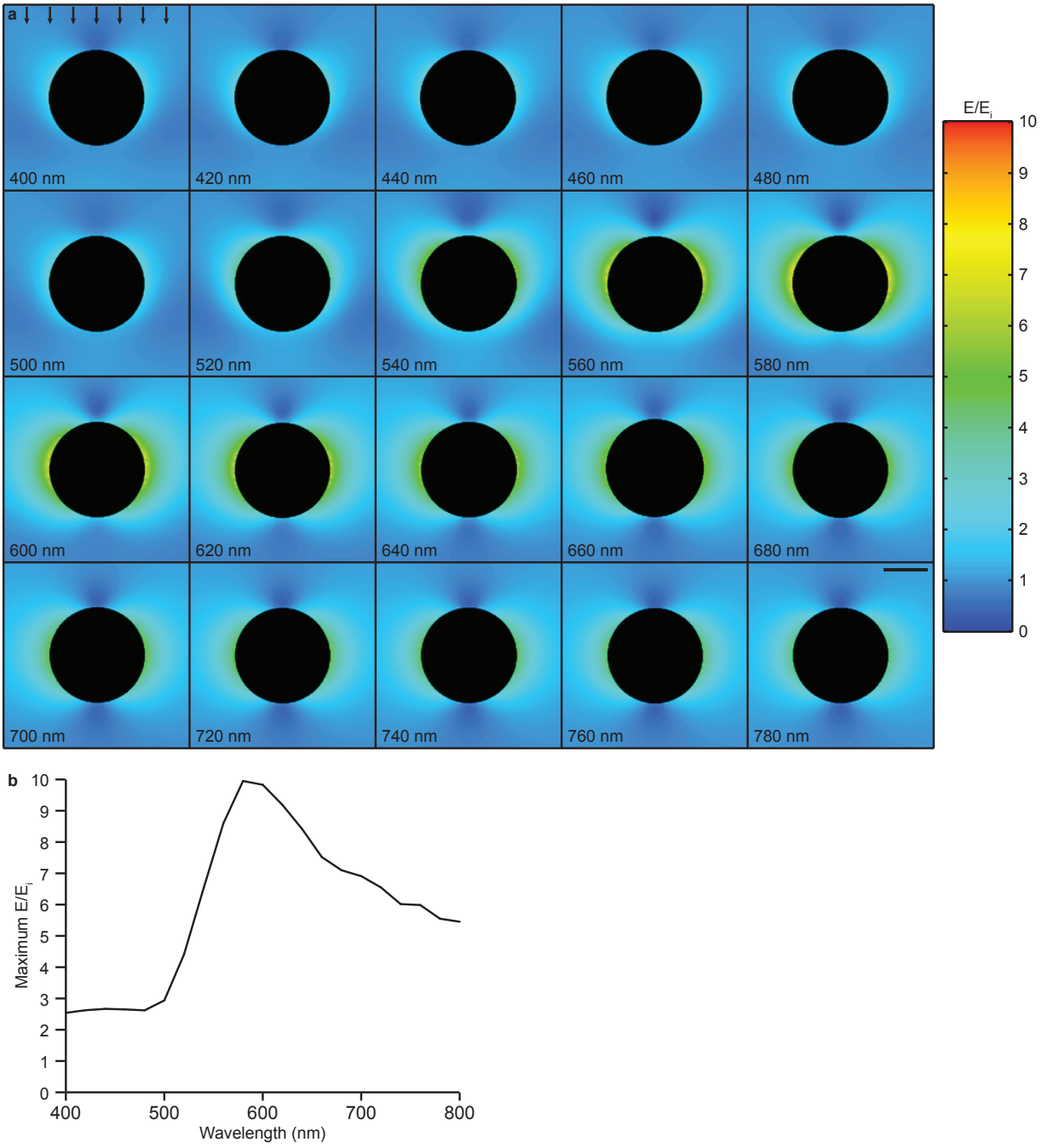


Figure 4 - 6. Electric field enhancement near gold nanoparticles at various wavelengths. (a) Cross-section of local electric field enhancement (E/E_i) for 85 nm diameter gold particles illuminated by light with various wavelengths from 400 nm to 780 nm in a medium with refractive index 1.39. The scale bar is 40 nm. The black circles are superimposed to indicate the location of the particle. The light propagates from the top of each panel and is polarized in the direction of the page. (b) Peak value of the electric field enhancement calculated at the particle surface at various wavelengths from 400 nm to 800 nm.

coherence length, evaluated as $\xi_N = \sqrt{L_1/a_0(T - T^*)}$ (where L_1 is a parameter characterizing the elastic properties of the mesogen, a_0 is a solvent parameter, and T^* is the lowest temperature at which the metastable isotropic phase can exist) and the ratio of L_1/W_s is the surface extrapolation length with W_s defined as the anchoring energy. In addition $\gamma_E = \varepsilon_a/3L_1$ is a constant proportional to the dielectric anisotropy, E_0 is the electric field at $z = 0$, and ξ_E is the characteristic screening length for the electric field. For 5CB, we used $a_0 = 8.7\text{x}10^5$ erg/K cm^3, $L_1 = 10^{-6}$ dyne $T^* = 307.15$K, $\varepsilon_a = 1.59\text{x}10^{-5}$ dyne/V^2 (19, 20). Guided by past studies, we assumed $W_s = 0.1$ μJ/cm^2 and $S_0 = 0.28$, although the conclusions below are not sensitive to these assumed values (21). As detailed in the Section 4.8, for green light with an intensity of 300 W/cm^2 (equivalent to 340 V/cm) incident on nanoparticles with a diameter of 85 nm, we calculated the change in the scalar order parameter of the solvent due to the interfacial electric field generated by the LSPR to be negligibly small (order of 10^{-6}). We also considered that faceting (evident in Figure 4-1) on the surfaces of the nanoparticles may lead to local field enhancements. Our estimates, however, lead us to conclude that the magnitude of such effects are not likely to underlie our experimental observations (see Section 4.8). Overall, we conclude that LSPR alone cannot provide an account of the light-induced changes in solvation that we have documented in our experiments. As detailed below, however, LSPR does play an indirect role in our observations via the generation of hot electron-hole pairs.

Next we explored the proposal that light-induced formation of hot electron-hole pairs within the gold nanoparticles generates interfacial electric fields that cause the changes in solvation shown in Figure 4-2 and 4-3. A hot electron is formed when a bound electron is excited into the conduction band of the gold nanoparticle (22). Once in the conduction band of the gold, the electron is not bound to the nucleus and thus is free to move about the metal. A positively

charged hole is also formed, but it has a mobility that is much lower than the hot electron. Specifically, we calculate the diffusion coefficients of hot electrons and holes in gold to be 41.4 cm^2/s and 1.01 cm^2/s, respectively (see Section 4.9). We hypothesized that this difference in mobility leads to a light-induced separation of charge within the gold nanoparticles, and thus the generation of interfacial electric fields that influence the solvation of the nanoparticles. As noted above, this interband transition can occur when a photon of energy greater than the band gap of the material is absorbed by the nanoparticle. For gold, the band gap is 2.38-2.45 eV (22), which corresponds to the energy of a photon with a wavelength of 520 nm. Our observation that the large gold nanoparticles illuminated by blue but not green or red light (Figure 4-3) acquire thick solvation shells is thus consistent with a mechanism involving the generation of hot electron-hole pairs. Here we emphasize that under blue light illumination, the photons incident on the gold nanoparticles generate electron-hole pairs but do not couple to the LSPR (see Figure 4-4).

While the above-proposed mechanism is consistent with the effects of blue light illumination on the solvation of the gold nanoparticles, we also note, however, that a key observations reported above is that small gold nanoparticles acquire optically enhanced solvation shells when exposed to green light whereas the large nanoparticles do not (Figure 4-3). In this context, we comment that the decay of excited states associated with LSPRs can also lead to the generation of hot electrons, with the probability of formation of hot electrons via this process increasing with decreasing size of the nanoparticle (Figure 4-4a) (23). To evaluate the possible role of LSPRs in the generation of hot electrons in our experiments, we calculated absorption spectra for hot electrons (Figure 4-4a). Inspection of Figure 4-4a reveals that under green light illumination, we indeed calculate the rate of formation of hot electrons per unit cross-sectional area for the smaller particles to be approximately double that of the large particles.

Overall, the calculations and experiments described above provide strong support for our proposal that the optically enhanced solvation of nanoparticles reported in Figure 4-3 correlates with light-induced formation of hot electron-hole pairs. Specifically, we propose that the hot electron-hole pairs generate interfacial electric fields of sufficient strength to form an ordered solvent corona. We note that past studies have shown that semiconductor materials (24) and graphite (25), when illuminated with an intense pulsed laser source, can generate transient electric fields with terahertz frequencies due to the formation and subsequent charge separation of hot electrons and holes (known as the photo-Dember effect) (26, 27). We make two additional comments regarding the role proposed for the photo-Dember effect in our experimental observations. First, we note that hot electron-hole pairs are typically short-lived with lifetimes of the order of 100 fs (28). However, Weiss and coworkers (29) found that the addition of a thiol monolayer to a gold nanoparticle increased hot electron-hot hole lifetimes to about 5 ps. Second, as noted above, the mobility of a hot electron (41.4 cm^2/s) is larger than a hot holes (1.01 cm^2/s). This second point leads us to conclude that a hot electron can travel a characteristic distance of $\sqrt{4D_e t}$ (where D_e is the diffusion coefficient and t is the lifetime of the hot electron) or 290 nm, whereas a hole will travel a characteristic distance of only 40 nm. When combined, these results suggest that hot electrons are able to diffuse throughout the volume of the nanoparticles used in our experiments within their lifetimes (and be stabilized at the surfaces of the thiol-functionalized nanoparticles) whereas hot holes are localized largely to the regions of the nanoparticle in which they are generated. As detailed in Section 4.9, under blue light illumination, we calculate that this optically-induced charge-separated state of the gold nanoparticles can lead to electric fields of 5.2×10^5 V/cm at a distance 10 nm from the surface of the nanoparticles. In contrast to LSPR, we calculate (using Eq. 1) the associated field strength to

be sufficiently large to cause the scalar order parameter characterizing solvent structuring to increase from 0 to 0.27 at $T - T_{NI} = 5^{\circ}C$.

To provide further support for our proposal regarding the role of hot electron-hole pairs on solvation of the nanoparticles, we performed several additional experiments. First, we investigated the effects of illumination on the solvation of silver nanoparticles (diameter of 157±8 nm) functionalized with the mixed monolayers. Silver has a band gap of 3.86-3.90 eV (22) corresponding to photons with a wavelength of about 320 nm. Based on this band gap, we predicted that the illumination of silver nanoparticles with blue light should not generate hot electrons and thus not lead to changes in solvation. Consistent with this prediction, we measured no significant change in the hydrodynamic sizes of silver nanoparticles when illuminated with either red or blue light (Figure 4-7). Second, we investigated the effect of the intensity of irradiance of blue light on the solvation of 164±11 nm-diameter gold nanoparticles (Figure 4-8). We predicted that the solvation of the nanoparticles would change with intensity of illumination when the rate of generation of hot electrons is comparable to their recombination rate. In this experiment, particles were simultaneously illuminated with both blue and red light. The red light was used to track the nanoparticle trajectories when the intensity of the blue light was too weak to permit particle tracking. We observed a change in the solvation of the nanoparticles (of about 20±5 nm) at an intensity of illumination of 80 W/cm^2, a value of irradiance corresponding to one photon per 10 ps incident on the nanoparticles. This rate is comparable to the above-mentioned lifetime of a hot electron, and thus consistent with a mechanism of light-induced solvation that is mediated by the generation of hot electron-hole pairs. Third, our observation that illumination changes the solvation of the nanoparticles by both MBBA and 5CB is consistent with the influence of the high frequency of electric fields

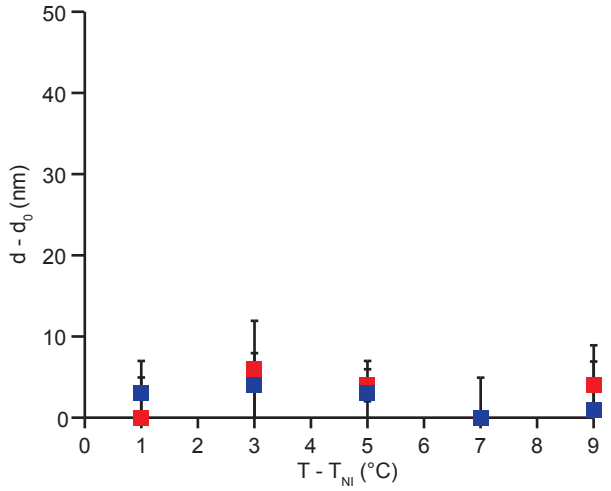


Figure 4 - 7. Difference between the hydrodynamic radius, d, and physical radius, d_0, of 157±8 nm diameter silver nanoparticles illuminated with a blue or red light source as represented by the color of the data points at various temperatures above the bulk clearing temperature of 5CB, T_{NI} (35˚C). Each data point represents an ensemble of 50 particles. The error bar represents the standard error of the measurements. Hydrodynamic size measurements were obtained using 40-50 particle trajectories from 2 independent samples. Data show mean ± s.e.m.

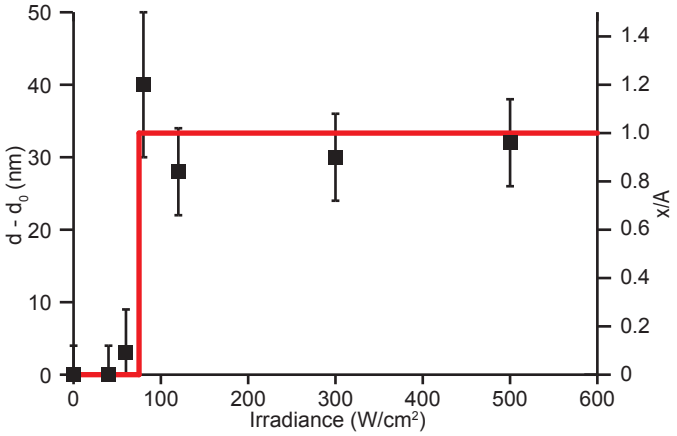


Figure 4 - 8. Increase in hydrodynamic diameter ($d-d_0$) induced by the illumination of 164±11 nm gold particles with various intensities of blue light (black squares; left axis). The red line shows the prediction of a simple model for accumulation of hot electrons (right axis). Hydrodynamic size measurements were obtained using 40-50 particle trajectories. Data show mean ± s.e.m.

generated by hot electrons on the interfacial ordering of these solvents (see Section 4.9 for additional discussion).

We reasoned that light-induced changes in solvation, as detailed above, should influence properties of gold nanoparticles other than hydrodynamic size. Specifically, Koenig *et al*. (30) reported previously that the LSPRs of gold nanoparticles supported on surfaces are sensitive to the local order of nematic phases of 5CB. The wavelength of maximum absorption (WoMA) of light by gold nanoparticles, which arises from LSPRs, was shown to be sensitive to changes in the dielectric environment up to 15 nm from the surfaces of the nanoparticles. We hypothesized that changes in the solvation of the gold nanoparticles, as induced by hot electrons, should also give rise to measurable changes in the WoMA of the gold nanoparticles. To this end, we fabricated surface-supported gold nanoparticles with diameters of 96±37 nm, functionalized them with mixed thiol monolayers of C16SH and C10SH, and measured their WoMAs (a representative optical density measurement is shown in Figure 4-9a). We determined the WoMA by measuring the wavelength-dependent absorption of a probe beam transmitted through our sample. In air, when the sample was co-illuminated with a 430 nm (blue light illumination) source (excitation beam) and the probe beam, we measured the excitation beam to have no effect on the WoMA of four independently prepared batches of gold nanoparticles (a representative measurement is shown in Figure 4-10). When immersed in 5CB and heated from 33˚C to 37˚C (thus triggering bulk phase transition from a nematic phase to an isotropic phase), the temperature-induced change in solvent ordering caused a red-shift in the WoMA of 1.40±0.16 nm (four independent samples), the magnitude of which is consistent with the prior observations of Koenig *et al*. (30). To determine if blue light illumination increased solvent ordering, we measured the WoMA before and after blue light illumination. At 37˚C, upon

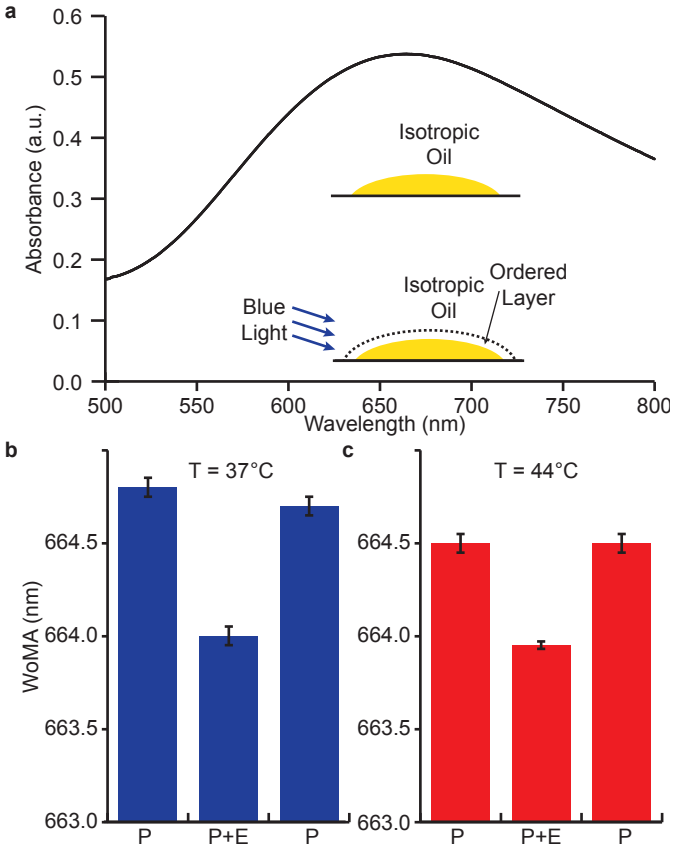


Figure 4 - 9. Influence of optically excited changes in solvation on plasmon resonances of gold nanoparticles (96±37 nm-diameter) functionalized with mixed monolayers supported on a glass surface. (a) Absorbance of a probe beam (P) of light by the gold nanoparticles in contact with isotropic 5CB at 37˚C. (b,c) WoMA of the sample in (a) with (P+E) or without (P) co-illumination of an excitation beam (E) of blue light at (b) 37˚C (T - T_{NI} = 2˚C) and (c) 44˚C (T - T_{NI} = 9˚C). The WoMA for each sample was measured before (left bar, P), during (center bar, P+E), or after (right bar, P) illumination with the excitation beam. Error bars represent the error in the mean of a Gaussian function fit to the data.

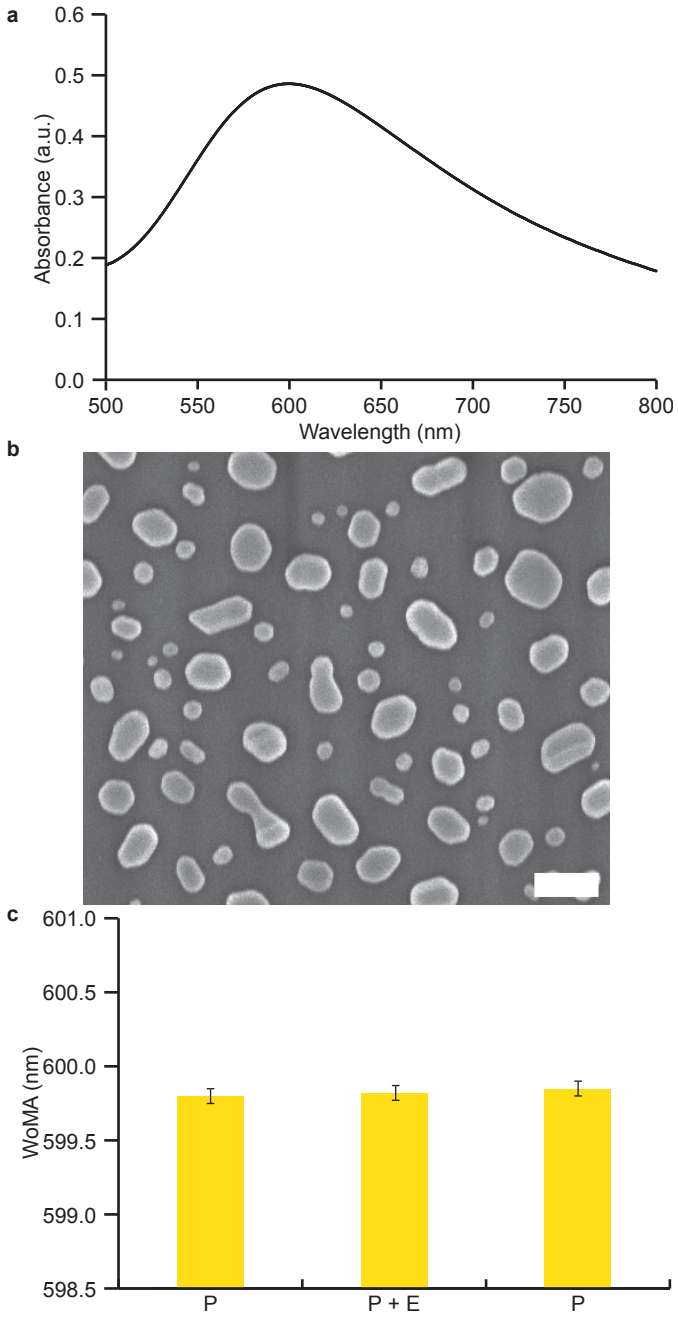


Figure 4 - 10. (a) Absorbance of a probe beam (P) of light by the gold nanoparticles in air at 37˚C. The curve is representative of an ensemble of similar measurements used in this study. (b) SEM measurements of the gold nanoparticles used in this study. The scale bar is 100 nm (c) WoMA of the sample in (a) with (P+E) or without (P) co-illumination of an excitation beam (E) of blue light at (b) 37˚C (T - T_{NI} = 2˚C) and (c) 44˚C (T - T_{NI} = 9˚C). The WoMA for each sample was measured before (left bar, P), during (center bar, P+E), or after (right bar, P) illumination with the excitation beam. Error bars represent the error in the mean of a Gaussian function fit to the data.

illumination with the blue excitation beam, we measured a blue shift in the WoMA of 0.73±0.06 nm. At 44˚C (9˚C above T_{NI}), a blue shift in the WoMA of 0.60±0.05 nm was measured (see Figure 4-9b and 4-9c for representative measurements). Significantly, these shifts in the WoMA are opposite to that observed when heating 5CB from an ordered to a disordered phase and thus consistent with blue light illumination of the nanoparticles leading to an increase in ordering of 5CB. The magnitude of the shift in the WoMA, when co-illuminated with the blue light excitation beam, is about half of that associated with the nematic to isotropic phase transition, suggesting that the interfacial ordering of 5CB induced by the blue light illumination is comparable to that present when 5CB is in a nematic phase. Overall, these measurements provide independent evidence of light-induced changes in solvation of metal nanoparticles, and thus support our interpretation of the light-triggered changes in hydrodynamic sizes of the nanoparticles.

4.4 Discussion

We make two comments regarding the generality of the observations reported in this paper. First, as noted in the introduction, we utilized isotropic phases of mesogenic solvents to amplify changes in solvation into effects that are readily measured by particle tracking. We emphasize, however, that the mechanism leading to changes in solvation – namely the influence of near surface electric fields generated by hot electron-hole pairs – is not limited to mesogenic solvents and should also lead to changes in the ordering of other polar solvents. Second, the generation of electric fields from hot electron-hole pairs is not limited to gold nanostructures. Many other materials can be optically excited to generate hot electrons, including other metals and semiconductors (31, 32), and thus we predict that optical control of solvent ordering, as demonstrated in this paper, should be broadly applicable to a range of systems. We also comment that the effects of electric fields generated by hot electrons on the near-surface solvent structuring should be measurable by other techniques such as by atomic force microscopy (AFM) (33) or by the surface force apparatus (34). Simulations of electric fields generated by hot electrons have been performed for semiconductor materials (27) and semiconductor materials in contact with thin metallic films (35). However, electric fields generated by hot electrons in isolated and chemically functionalized metal surfaces have not been treated in detail. Detailed simulations of optically-induced electric fields arising from hot electron-hole pairs in metals have the potential to aid in the rational design of systems that permit optical control of solvation near surfaces.

4.5 Materials and Methods

Functionalization of Gold and Silver Nanoparticles

Gold nanoparticles were purchased as suspensions in aqueous solution from Ted Pella (Redding, CA) and silver nanoparticles were purchased as suspensions in aqueous solution from Sigma-Aldrich (Milwaukee, WI). To remove trace salts from the nanoparticle suspensions, we repeatedly diluted the suspensions with deionized water, centrifuged the nanoparticles, and then resuspended the nanoparticles in deionized water.

Gold and silver nanoparticles were functionalized with monolayers of alkanethiols as follows. First, hexadecanethiol (C16SH) (Sigma-Aldrich, Milwaukee, WI) and decanethiol (C10SH) (Sigma-Aldrich, Milwaukee, WI) stocks were passed over activated alumina (Sigma-Aldrich, Milwaukee, WI) to remove oxidized contaminants. Second, thiols were dispersed in degassed ethanol at a total concentration of 4 mM. The thiols solutions comprised 3.2 mM C10SH and 0.8 mM C16SH (to form mixed thiol monolayers) or 4 mM C10SH (to form single thiol monolayers). Third, 200 μL of the washed nanoparticles in water were mixed with 800 μL of the 4 mM thiols in ethanol solution and heated to 50˚C for 2 hr. Fourth, to remove excess thiols, the nanoparticles were washed four times in ethanol as described above. Finally, the particles were dried in vacuum for 2 hours at room temperature and dispersed in 50 μL of 4-*n*-pentyl-4'-cyanobiphenyl (5CB) or n-(4-methoxybenzylidene)-4-butylaniline (MBBA). Some measurements, as indicated in the main text, used particles which were additionally washed in hexanes and dried in vacuum prior to being suspended in 5CB. Nanoparticles in 5CB and MBBA were sonicated for 30 s in a bath sonicator to remove aggregates.

Nanoparticle Tracking Measurements using Dark-Field Microscopy

We used dark-field microscopy to track the motion of individual gold nanoparticles, as described elsewhere (11). The temperatures of the samples were controlled with a precision of $\pm 0.1^{o}$C by forcing heated air into a shroud that encompassed the entire microscope. The set-up was equilibrated at each desired temperature for at least 1 hour prior to performing measurements. Isotropic oils containing nanoparticles were wicked into optical cells fabricated from silanized glass coverslips and microscopes slides separated by 50 μm-thick spacers. The focal plane of the microscope was located at least 10 μm from either of the confining surfaces of each optical cell to ensure that the mobilities of the nanoparticles were not influenced by hydrodynamic interactions with the surfaces. Two-minute movies of nanoparticle motion were taken with a frame rate of 30 s^{-1}.

Nanoparticle trajectories analyzed using ImageJ (36) with the particle tracking plugin Mosaic (37). The mean squared displacement (MSD) versus time delay (τ) was calculated for each particle trajectory in two orthogonal directions in the plane of view, denoted as the x- and y-directions. The diffusion coefficients (D) were calculated in the x- and y-directions by fitting a linear least squares fit to the mean squared displacement data,

$$\mathrm{MSD}(\tau) = 2\mathrm{D}\tau + \epsilon \qquad (2)$$

where ϵ is a finite intercept that accounts for static localization errors introduced by uncertainty in the exact particle position (38). These errors do not affect the measured diffusion coefficient (the slope of the linear least-squares fit). The diffusion coefficients measured in the x- and y-directions did not differ by more than 5%.

Preparation of Surface-Immobilized Gold Nanoparticles

Glass slides (Fisher Scientific, Pittsburgh, PA) were cleaned using a solution of 30% H_2O_2 and 70% H_2SO_4 for 1 hour and washed 10 times with water. The glass slides were dried in

an oven at 120˚C for 1 hour and placed in an electron-beam evaporator under vacuum. At a pressure of $2x10^{-6}$ torr, 10 nm thick films of gold were deposited on the glass surfaces at a rate of 0.02 nm/s. The gold-coated glass slides were placed in a furnace at 560˚C for one hour. The slides were subsequently cooled overnight in the furnace to prevent cracking of the glass.

Gold nanoparticle decorated glass surfaces were functionalized with alkanethiols by immersing gold-nanoparticle-decorated glass pieces in 4 mL of the thiol solutions, as prepared above, at 50˚C for 2 hours. Subsequently, the samples were washed in 4 mL of ethanol 4 times. Nanoparticle-decorated substrates were dried in a vacuum for 2 hours at room temperature.

Scanning Electron Microscopy

We measured the sizes of gold nanoparticles using scanning electron microscopy. For gold nanoparticles in solution, 50 μL of gold or silver nanoparticle sol was washed three times by diluting the solution in 3 mL of ultrapure water, centrifuging at 5,000g to sediment the nanoparticles, and pouring off the supernatant. The nanoparticles were suspended in 100 μL of ultrapure water and sonicated for 10 min in a bath sonicator. 20 μL of solution was placed on a 1 cm x 1 cm piece of single-crystal silicon. The polished side of the silicon wafer had a 20 nm thick layer of gold deposited using electron beam evaporation. The nanoparticles in water were allowed to evaporate under ambient conditions over 5 hours to minimize convective flow and to ensure that gold particles were singly and randomly deposited on the surface. The nanoparticles were imaged with a 2 kV electron beam at random locations on the surface with 75,000x magnification. For gold nanoparticle-decorated surfaces, the glass substrates were imaged without further modification with a 10 kV electron beam and 50,000x magnification to minimize charging of the sample by the electron beam. The gold nanoparticle-decorated surfaces of the glass were grounded with additional conductive tape to further mitigate charging effects.

The sizes of the nanoparticles were analyzed with the software ImageJ (36). Briefly, nanoparticle images were passed through a threshold filter to determine the boundary of each individual particle. The validity of the boundary was verified by superimposing the nanoparticle boundaries over the original images. The diameters of the nanoparticles were determined by measuring the areas of the particles in the images and calculating the diameter of a circle with the equivalent area.

Ultraviolet-Visible Spectrophotometry

We performed ultraviolet-visible spectrophotometry (UV-Vis) on gold nanoparticles dispersed in 5CB. Functionalized gold nanoparticles were dispersed in ethanol and placed in a bath sonicator for 20 min. Next, 15 μL of the nanoparticles in ethanol was dispersed in 285 μL of 5CB and mixed with a glass Pasteur pipette. The final concentration of nanoparticles was $4x10^8$ particles/mL. Measurements were performed using a Varian Cary 100 spectrophotometer and a sealed quartz cell with 1 cm path length. Absorbance data were obtained over a range of wavelengths between 800 nm to 400 nm in 1 nm increments with a 1 s dwell time at each wavelength. Absorbance measurements were converted to extinction efficiencies using the relation adapted from Fernig *et al*. (18)

$$\mathrm{Abs} = \frac{\pi d^2 Q_{ext} l N}{9.212} \qquad (3)$$

where Abs is the measured optical absorbance, d is the average diameter of the gold nanoparticles, l is the path length of the sample cell, N is the number density of the particles, and Q_{ext} is the extinction efficiency of the particles.

UV-Vis measurements were also performed on gold nanoparticle-decorated substrates. Sample cells were prepared as described previously (39). The temperature was controlled using a water jacketed sample holder to a precision of 0.1˚C. The temperature was verified by attaching

a thermocouple to the sample holder. Samples were allowed to equilibrate in the sample holder for 30 min before measurements were performed to remove thermal gradients. The wavelength of maximum absorbance (WoMA) of the substrates was determined by measuring the attenuation of a probe beam transmitted though the substrate. Measurements were performed at wavelengths between 700 and 550 nm at increments of 0.2 nm and a dwell time at each wavelength of 5 s. To measure the effects of blue light on the WoMA of the substrates, a second excitation beam produced by a 430 nm LED (LED groupbuy, St. Louis, MO) illuminated the substrate (in addition to the probe beam). The excitation beam was placed such that it illuminated the sample with an angle of incidence of 72˚ (measured from the surface normal). A pair of stacked optical long pass filters with cut-on wavelengths of 495 nm were placed in front of the detector (Thor Labs, Newton, NJ). We estimated the intensity of the excitation beam to be 90 W/cm^2 which is 1500 times more intense than the probe beam (0.06 W/cm^2).

Calculation of Electric Field Strengths near Gold Nanoparticles

We calculated the optical properties and near-surface electric field strengths using the discrete dipole approximation (DDA) (17). In this method, a metal nanoparticle is approximated as an array of polarizable elements. The polarization of element j at a location $\mathbf{r}_j$ is $\mathbf{p}_j$ and can be determined from the following relation:

$$\mathbf{p}_j = \alpha_j\left(\mathbf{E}^{inc}(\mathbf{r}_j) + \sum_{j'\neq j}\mathbf{E}_{j'}^{scat}(\mathbf{r}_j)\right) \quad (4)$$

where

$$\mathbf{E}_{j'}^{scat}(\mathbf{r}_j) = \frac{e^{ik_m|r_{jj'}|}}{4\pi\varepsilon_m|r_{jj'}|^3}\left(A_{jj'}\mathbf{p}_{j'} - B_{jj'}\frac{\mathbf{r}_{jj'}(\mathbf{r}_{jj'}\cdot\mathbf{p}_j)}{|r_{jj'}|^2}\right) \quad (5)$$

is the electric field scattered by element j' at position $\mathbf{r}_j$ and

$$A_{jj'} = (k_m|\mathbf{r}_{jj'}|)^2 + ik_m|\mathbf{r}_{jj'}| - 1 \quad (6)$$

$$B_{jj'} = \left(k_m \left|\mathbf{r}_{jj'}\right|\right)^2 + i3k_m \left|\mathbf{r}_{jj'}\right| - 3 \quad (7)$$

where α_j is the polarizability of the element at $\mathbf{r}_j$, the polarizability is calculated from the dielectric constant (ε) of the material at that location using the Clausius-Mossotti relation

$$\frac{4}{3}\pi n\alpha_j = \frac{\varepsilon - 1}{\varepsilon + 2} \quad (8)$$

where n is the atomic density of molecules , In Eq. 4, $\mathbf{E}^{inc}(\mathbf{r}_j) = \mathbf{E}_i \exp\{i\mathbf{k}_m \cdot \mathbf{r}_j - i\omega t\}$ is the electric field due to the incident illumination. The dielectric properties of gold and silver, as measured by Johnson and Christy (40), were used in our calculations. $k_m = 2\pi/\lambda_m$ is the wavenumber of light in the ambient medium, $\mathbf{k}_m = k_m \hat{\mathbf{u}}$ ($\hat{\mathbf{u}}$ is defined as the unit vector of direction cosines), and $\mathbf{r}_{jj'} = \mathbf{r}_j - \mathbf{r}_{j'}$ is the coordinate difference. The DDA was solved using the biconjugate gradient with stabilization method (41). Extinction (Q_{ext}) and absorption (Q_{abs}) efficiencies can be determined from the above-calculated electric fields as

$$Q_{ext} = \frac{16\pi k_m}{\pi d^2 |\mathbf{E}_i|^2} \sum_{j=1} \mathrm{Im}\left\{\mathbf{E}^{inc}(r_j)^* \cdot \mathbf{p}_j\right\} \quad (9)$$

$$Q_{abs} = \frac{16\pi k_m}{\pi d^2 |\mathbf{E}_i|^2} \sum_{j=1} \mathrm{Im}\left\{\mathbf{p}_j \cdot \left(\alpha_j^{-1}\right)^* \mathbf{p}_j{}^*\right\} - \frac{2}{3} k_m^3 \left|\mathbf{p}_j\right|^2 \quad (10)$$

The freely-available DDSCAT implementation incorporates all of the above methods without modification.

4.6 Additional Measurements of Nanoparticle Mobility

Mobility of Gold Nanoparticles in MBBA

To investigate the role of the molecular structure of the solvent in our observations, we performed additional measurements in an isotropic liquid phase of n-(4-methoxybenzylidene)-4-butylaniline (MBBA; Figure 4-1e) at temperatures at or above 43˚C. We note that an isotropic liquid of MBBA transforms into an ordered nematic phase below 42˚C. When using MBBA (Figure 4-11) at 43˚C (1˚C above T_{NI}), and gold nanoparticles with diameters of 143±7 nm that were functionalized with mixed C16SH:C10SH monolayers, we measured illumination with blue light to increase the hydrodynamic sizes of the nanoparticles by 54±12 nm relative to their physical size. When illuminated with green or red light at 43˚C, however, we measured the hydrodynamic sizes of nanoparticles to be 42±16 nm smaller than that measured with blue light. These results reveal that illumination of the gold nanoparticles in both 5CB and MBBA lead to comparable changes in hydrodynamic size.

We next sought to investigate the hydrodynamic size of 143±7 nm gold nanoparticles in MBBA over a range of temperatures 1˚C to 9˚C above its bulk clearing temperature (Figure 4-12). One degree above the bulk clearing temperature, nanoparticles functionalized with mixed monolayers, when measured with white light illumination, exhibited hydrodynamic diameters 48±10 nm larger than the physical diameters of the nanoparticles. In comparison, nanoparticles in 5CB one degree above the bulk clearing temperature with mixed monolayers when illuminated with white light, exhibited hydrodynamic diameters that were 41±4 nm larger than their physical diameters, indistinguishable from our result for nanoparticles in MBBA. When the temperature increased to seven degrees above the bulk clearing temperature, 143±7 nm-diameter gold particles with mixed monolayers in MBBA exhibit a hydrodynamic

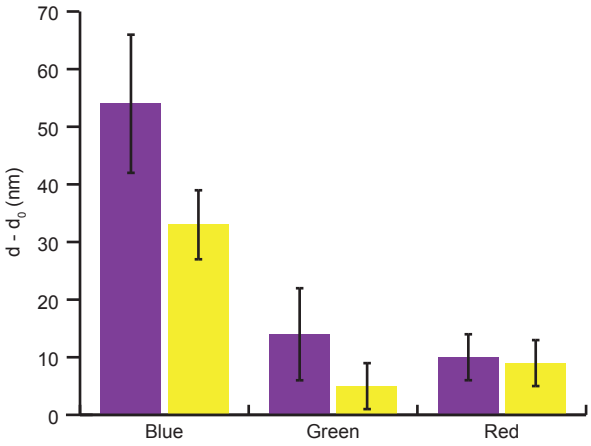


Figure 4 - 11. A comparison between measurements of the hydrodynamic sizes of 143±7 nm gold nanoparticles in MBBA (purple) and 164±11 nm gold particles in 5CB (yellow) with a mixed thiol monolayer and one degree above T_{NI} of each mesogen. Hydrodynamic size measurements were obtained using 40-50 particle trajectories from 3 independent samples. Data show mean ± s.e.m.

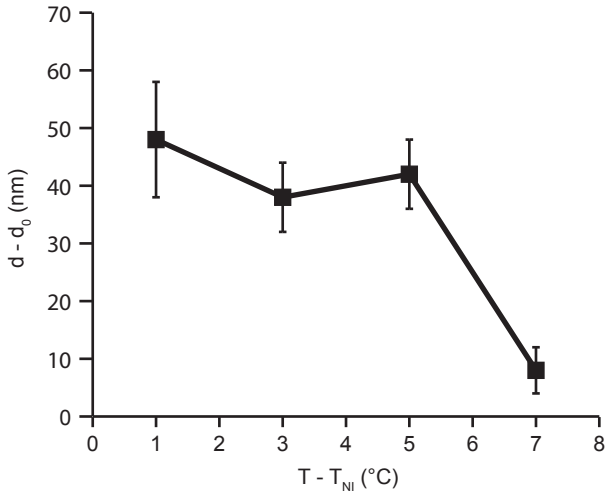


Figure 4 - 12. Hydrodynamic diameter (d) minus physical diameter (d_0) of 143±7 nm gold particles in the isotropic phase of *N*-(4-methoxybenzylidene)-4-butylaniline (MBBA) at temperatures relative to the bulk clearing temperature (T_{NI} = 42°C) for particles functionalized with a mixed thiol monolayer and measured with white light illumination. Hydrodynamic size measurements were obtained using 40-50 particle trajectories from 2 independent samples. Data show mean ± s.e.m.

diameter 8±4 nm larger than the physical diameter of the particles. By comparison, in 5CB seven degrees above the bulk clearing temperature, the 164±11 nm gold nanoparticles functionalized with a mixed thiol monolayer have a hydrodynamic diameter 1±4 nm larger than the physical diameter of the nanoparticles.

The results above establish the qualitative similarity of the behavior of 164±11 nm gold nanoparticles in the isotropic phase of 5CB and 143±7 nm gold particles in the isotropic phase of MBBA. The frequency of electric fields associated with charge dipoles generated from hot electron-hole pairs has previously been characterized to be in the terahertz range (24). As a comparison, 633 nm light has a frequency of 474 THz. For optical frequency electric fields, the response of a mesogen to the presence of an electric field is described by the anisotropy in the refractive indices (birefringence). For 5CB (42) and several liquid crystalline materials with negative dielectric anisotropy (43), optical constants associated with terahertz frequency light have been measured to be invariant over a wide range of frequencies and do not differ significantly from optical constants associated with higher frequency visible light. The birefringence of MBBA is 0.2139 when illuminated with 633 nm light and the birefringence of 5CB is 0.1754 when illuminated with 633 nm light (44). While the static dielectric anisotropy of MBBA is different in both magnitude and sign from the dielectric anisotropy of 5CB, the birefringence of MBBA is similar in both sign and magnitude to the birefringence of 5CB. In the presence of electric fields with terahertz or greater frequency, we expect similar responses to electric fields.

Effect of Illumination and Solvent Refractive Index on Measurement of Nanoparticle Mobility with Dark-Field Microscopy

We performed a series of control experiments using red, green and blue band-pass filters and silica nanoparticles with diameters of 391±35 nm (functionalized with a monolayer of dimethyloctadecyl[3-trimethoxysilyl)propyl]ammonium chloride (DMOAP)) at 5˚C above T_{NI} (as described above, we measured the hydrodynamic diameter of gold nanoparticles to be 28±8 nm larger than the physical size of the nanoparticles 5˚C above T_{NI}). We used silica nanoparticles of this diameter in isotropic 5CB because they have the same scattering cross-section as gold nanoparticles with diameters of 164 nm and thus the silica nanoparticles can be tracked using dark-field microscopy. We measured the silica nanoparticles to have hydrodynamic diameters of 380±10 nm, 400±12 nm, 390±9 nm, and 400±8 nm when using white, red, green, and blue light, respectively, with a sample size of 300 particles. A statistical t-test confirmed that these measured values are indistinguishable.

We also confirmed that neither the addition of the filters nor the changes in refractive index of the 5CB with temperature changed the magnification of the microscope and thus the measured displacement of the particles used to determine the diffusion coefficients. Finally, we measured the hydrodynamic sizes of the gold nanoparticles in solvents such as 30% hexadecane in mineral oil (viscosity of 25.2±2.5 mPa.s) and determined that the diffusion coefficients of the nanoparticles did not change with wavelength of illumination. This result is consistent with our conclusion that proximity of the solvent to a phase transition (isotropic-to-nematic phase transition) predisposes the solvent to ordering in the presence of interfacial fields.

4.7 Additional Experimental Considerations Related to Single-Particle Tracking of Gold Nanoparticles

Investigating the Possible Role of Optical Pressure on the Motion of Nanoparticles

Past studies have reported that gradients in the intensity of light (optical pressure) can lead to forces that act on particles to modify their motion in a solvent (45). Our observations are inconsistent with this mechanism of interaction with light because the displacements of the nanoparticles were not measured to be biased along directions corresponding to gradients in the intensity of light in our experiments.

Formation of a Prenematic Wetting Layer at Surfaces of Dielectric Particles

Several past studies have reported the hydrodynamic diameters of dielectric nanoparticles (e.g., silica nanoparticles) dispersed in isotropic phases of 5CB to increase by ~5 nm as temperature decreases to within one or two degrees above T_{NI} (35°C) (12, 13). It was concluded that the increase in hydrodynamic size was caused by surface-induced ordering of 5CB molecules near the nanoparticles. The thickness of the so-called prenematic solvation layer measured in those past studies (~2.5 nm) is similar in magnitude to the coherence length of 5CB, the distance over which surface-induced order would be expected to propagate into the bulk solvent (the coherence length of 5CB is approximately 8 nm at 1˚C above T_{NI}). In contrast to these measurements, we measured the solvation layer of chemically functionalized gold nanoparticles to increase upon illumination in a wavelength-dependent manner (see Figure 4-3) by up to 33±6 nm at 1˚C above T_{NI}.

Investigating the Possible Role of Desorption of Thiols from Gold Nanoparticles

We performed several additional experiments to eliminate a number of possible origins of the changes in the solvation layer thickness. First, we considered the possibility that the nanoparticles used in our experiments were covered initially in a multilayer of physisorbed

alkanethiols (as observed elsewhere) that caused the larger than expected hydrodynamic diameter just above T_{NI} and that the multilayer dissolved as the temperature was elevated. To test this possibility, the nanoparticles were washed in hexanes after functionalization. Hexanes have previously been shown to remove physisorbed multilayers of alkanethiols from gold surfaces (46). However, we found that gold nanoparticles functionalized with the mixed alkanethiols and washed in hexanes exhibited mobilities that were indistinguishable from nanoparticles that were not washed with hexanes. We additionally performed experiments to determine if the temperature-dependent changes in hydrodynamic diameters reported in Figure 4-2 might be caused by thermal desorption of the chemisorbed alkanethiol monolayers. When using nanoparticles with monolayers deposited at 50˚C, however, we observed no hysteresis upon heating or cooling of our samples, a result that is inconsistent with thermal degradation of the monolayers.

4.8 Discussion of the Role of Electric Fields Generated by Local Surface Plasmon Resonances on the Hydrodynamic Size of Gold Nanoparticles

Evaluating the Accuracy of the DDA Method for Predicting the Absorption and Extinction Efficiencies of Gold Nanoparticles

Figure 4-4a shows the absorbance and extinction efficiency of the gold nanoparticles, plotted as a function of the wavelengths of light, as calculated using the discrete dipole approximation method (DDA) (17) (see Materials and Methods). A solvent with a refractive index of 1.39 was used in these calculations (Fig. 4-4a). For comparison, Fig. 4-4b shows extinction efficiencies obtained from measurements of the optical density (using methods adapted from Fernig *et al*. (18)) using 164±11 nm- and 85±7 nm-diameter gold nanoparticles dispersed in 95% 5CB-5% ethanol solution (ethanol was added to obtain an isotropic phase of 5CB at room temperature. We note that the isotropic refractive index of 5CB is 1.63 which is greater than the refractive index of 1.39 which fits the calculations to the data. The difference between the fitted refractive index and the isotropic refractive index of 5CB can be accounted for by the presence of an alkanethiol monolayer on the gold nanoparticles (the refractive index of decane is 1.41), and the presence of ethanol in our measurements (the refractive index of ethanol is 1.36).

Influence of an Electric Field on the Order Parameter of a LC near a Boundary with Finite Anchoring Energy

To calculate the scalar order parameter, S, of 5CB near the nanoparticle surface in the presence of an electric field caused by the local surface plasmon resonance, we determined S(z) that minimized the free energy density of our mesogenic medium, F. We use the Landau-de Gennes expression for the free energy density (19).

$$F = \int \frac{3}{4} a_0 (T - T^*) S^2 - \frac{1}{4} b S^3 + \frac{9}{16} c S^4 + \frac{3}{4} L_1 (\nabla_i S)^2 + \frac{9}{4} L_1 (\nabla_i n_j) - \frac{\varepsilon_a}{2} S E^2 d^3 r \qquad (11)$$

where a_0, b, c, and L_1 are the Landau parameters for the mesogen. For 5CB, typical values are $a_0 = 8.7\text{x}10^5$ erg/K cm^3, b = $2.13\text{x}10^7$ erg/cm^3, c = $1.73\text{x}10^7$ erg/cm^3, and $L_1 = 10^{-6}$ dyn. Note that we set $L_2 = 0$ to simplify the above expression. A non-zero L_2 would introduce anisotropy into the above expression (19). T^* is the lowest temperature at which a metastable isotropic phase can exist (for 5CB, $T^* = 307.15$K). T is the absolute temperature of the system and n_j is the j^{th} component of a unit vector indicating the direction of the director. The final term in this expression is the free-energy density due to the presence of an electric field. ε_a is the dielectric anisotropy of the mesogen and E is a function that represents the magnitude of the electric field.

Because the particles used in our study are much larger than the mesogen, we approximate the particle surface as an infinite flat surface. The distance from the surface is z with z = 0 being the particle surface. We make the simplifying assumptions that our director field is uniform ($\nabla_i n_j = 0$), S = S(z), and E = E(z), which leads to

$$F = \int \frac{3}{4} a_0 (T - T^*) S(z)^2 - \frac{1}{4} b S(z)^3 + \frac{9}{16} c S(z)^4 + \frac{3}{4} L_1 \left(S'(z)\right)^2 - \frac{\varepsilon_a}{2} S(z) E(z)^2 dz \quad (12)$$

To find function, S(z), which minimizes F, we utilize the Euler-Lagrange equation:

$$\frac{\partial}{\partial \alpha} I(\alpha, \beta, \gamma) - \frac{\partial}{\partial \gamma} \left(\frac{\partial}{\partial \beta} I(\alpha, \beta, \gamma) \right) = 0 \quad (13)$$

where $I(\alpha, \beta, \gamma)$ is the integrand from Eq. 12 and $\alpha = S(z), \beta = S'(z),$ and $\gamma = z$. Substituting $I(\alpha, \beta, \gamma)$ into the Euler-Lagrange expression leads to

$$\frac{3}{2} a_0 (T - T^*) \alpha - \frac{3}{4} b \alpha^2 + \frac{9}{4} c \alpha^3 - \frac{\varepsilon_a}{2} E(\gamma)^2 - \frac{\partial}{\partial \gamma} \left(\frac{3}{2} L_1 \beta \right) = 0 \quad (14)$$

We rearrange and multiply by $-\frac{2}{3L_1}$ to obtain

$$\frac{\partial}{\partial \gamma} \beta - \frac{a_0 (T - T^*)}{L_1} \alpha + \frac{b}{2L_1} \alpha^2 - \frac{3c}{2L_1} \alpha^3 + \frac{\varepsilon_a}{3L_1} E(\gamma)^2 = 0 \quad (15)$$

Finally, we substitute $\alpha = S(z), \beta = S'(z),$ and $\gamma = z$ to arrive at an expression for S(z) which minimizes the free energy density of the medium, namely

$$S''(z) - \frac{1}{\xi_N^2} S(z) + \frac{b}{2L_1} S(z)^2 - \frac{3c}{2L_1} S(z)^3 + \frac{\varepsilon_a}{3L_1} E(z)^2 = 0 \quad (16)$$

where $\xi_N = \sqrt{\frac{L_1}{a_0(T-T^*)}}$ is the nematic coherence length of the LC. To solve the above expression, we assume homotropic anchoring of the mesogen at the surface (z = 0) and introduce the boundary conditions

$$1.\, S'(0) - \frac{1}{\gamma_s \xi_N}(S(0) - S_0) - \frac{3}{2\gamma_n \xi_N} S_0(\Theta(0) - \Theta_0) = 0 \quad (17)$$

$$2.\, \lim_{z\to\infty} S(z) = 0$$

where $\gamma_s = \frac{L_1}{\xi_N W_s}$ and $\gamma_n = \frac{L_1}{\xi_N W_n}$ are the ratios of the nematic coherence length and the surface extrapolation lengths and W_S and W_n are the energetic penalties for S and **n** at the surface not being equal to the preferred S (S_0) and **n** (denoted by Θ_0) of the surface, respectively. The first boundary condition is a generalization of the Rapini–Papoular potential describing anchoring at the particle surface (21). The second boundary condition corresponds to the bulk material being in an isotropic phase far from the particle surface. We assume that the non-harmonic terms are small for small S and that the tilt of the LC is constant. The above expressions can be simplified to:

$$S''(z) - \frac{1}{\xi_N^2} S(z) = -\gamma_E E_0^2 e^{-2\frac{z}{\xi_E}} \quad (18)$$

with boundary conditions:

$$1.\, S'(0) - \frac{1}{\gamma_s \xi_N}(S(0) - S_0) = 0 \quad (19)$$

$$2.\, \lim_{z\to\infty} S(z) = 0$$

where $\gamma_E = \frac{\varepsilon_a}{3L_1}$ is a constant proportional to the dielectric anisotropy of the material and is $\varepsilon_a = 1.59\text{x}10^{-5}$ dyne/V^2 for 5CB (20). From inspection of the electric field strength around a gold

nanoparticle (see Figure 4-5 and 4-6), we approximate the magnitude of the electric field as a decaying exponential with distance from the particle surface.

$$E(z) = E_0 e^{-\frac{z}{\xi_E}} \quad (20)$$

where E_0 is the electric field strength at the surface and ξ_E is the characteristic length scale for the decay of the electric field from the surface. To solve for S, we write the solution as the sum of the homogeneous solution, S_h, and the particular solution, S_p

$$S(z) = S_h(z) + S_p(z) \quad (21)$$

We solve for the homogeneous solution for S(z):

$$S_h(z) = C_2 e^{-\frac{z}{\xi_N}} + C_3 e^{\frac{z}{\xi_N}} \quad (22)$$

where C_2 and C_3 are constants to be determined. The particular solution must have the form:

$$S_p(z) = C_1 e^{-2\frac{z}{\xi_E}} \quad (23)$$

where C_1 is a constant to be determined. The first and second derivatives for S_p are

$$S_p'(z) = -\frac{2C_1}{\xi_E} e^{-2\frac{z}{\xi_E}} \quad (24)$$

$$S_p''(z) = \frac{4C_1}{\xi_E^2} e^{-2\frac{z}{\xi_E}} \quad (25)$$

Substituting for S(z) and S''(z) into the initial expression, we find

$$\frac{4C_1}{\xi_E^2} e^{-2\frac{z}{\xi_E}} - \frac{C_1}{\xi_N^2} e^{-2\frac{z}{\xi_E}} = -\gamma_E E_0^2 e^{-2\frac{z}{\xi_E}} \quad (26)$$

We multiply by $\xi_N^2 \xi_E^2 e^{2\frac{z}{\xi_E}}$

$$4C_1 \xi_N^2 - C_1 \xi_E^2 = -\gamma_E \xi_N^2 \xi_E^2 E_0^2 \quad (27)$$

and solve for C_1

$$C_1 = \frac{\gamma_E \xi_N^2 \xi_E^2 E_0^2}{\xi_E^2 - 4\xi_N^2} \quad (28)$$

Thus, the particular solution is

$$S_p(z) = \frac{\gamma_E \xi_N^2 \xi_E^2 E_0^2}{\xi_E^2 - 4\xi_N^2} e^{-2\frac{z}{\xi_E}} \quad (29)$$

and the general solution is

$$S(z) = C_2 e^{-\frac{z}{\xi_N}} + C_3 e^{\frac{z}{\xi_N}} + \frac{\gamma_E \xi_N^2 \xi_E^2 E_0^2}{\xi_E^2 - 4\xi_N^2} e^{-2\frac{z}{\xi_E}} \quad (30)$$

By inspection, we note that the second boundary condition implies that $C_3 = 0$ and

$$S(z) = C_2 e^{-\frac{z}{\xi_N}} + \frac{\gamma_E \xi_N^2 \xi_E^2 E_0^2}{\xi_E^2 - 4\xi_N^2} e^{-2\frac{z}{\xi_E}} \quad (31)$$

We take the first derivative with respect to z

$$S'(z) = -\frac{C_2}{\xi_N} e^{-\frac{z}{\xi_N}} - \frac{2\gamma_E \xi_N^2 \xi_E E_0^2}{\xi_E^2 - 4\xi_N^2} e^{-2\frac{z}{\xi_E}} \quad (32)$$

and substitute for S'(z) and S(z) in the first boundary condition

$$-\frac{C_2}{\xi_N} e^{-\frac{z}{\xi_N}} - \frac{2}{\xi_E} \frac{\gamma_E \xi_N^2 \xi_E^2 E_0^2}{\xi_E^2 - 4\xi_N^2} e^{-2\frac{z}{\xi_E}} - \frac{1}{\gamma_s \xi_N} \left(C_2 e^{-\frac{z}{\xi_N}} + \frac{\gamma_E \xi_N^2 \xi_E^2 E_0^2}{\xi_E^2 - 4\xi_N^2} e^{-2\frac{z}{\xi_E}} - S_0 \right) = 0 \quad (33)$$

We set z = 0 to satisfy the first boundary condition and multiply by -1

$$\frac{C_2}{\xi_N} + \frac{2}{\xi_E} \frac{\gamma_E \xi_N^2 \xi_E^2 E_0^2}{\xi_E^2 - 4\xi_N^2} + \frac{1}{\gamma_s \xi_N} \left(C_2 + \frac{\gamma_E \xi_N^2 \xi_E^2 E_0^2}{\xi_E^2 - 4\xi_N^2} - S_0 \right) = 0 \quad (34)$$

We multiply by $\gamma_s \xi_N$

$$\gamma_s C_2 + \frac{2\gamma_s \xi_N}{\xi_E} \frac{\gamma_E \xi_N^2 \xi_E^2 E_0^2}{\xi_E^2 - 4\xi_N^2} + C_2 + \frac{\gamma_E \xi_N^2 \xi_E^2 E_0^2}{\xi_E^2 - 4\xi_N^2} - S_0 = 0 \quad (35)$$

And collect like terms

$$(\gamma_s + 1) C_2 = S_0 - \frac{\gamma_E \xi_N^2 \xi_E^2 E_0^2}{\xi_E^2 - 4\xi_N^2} \left(\frac{2\gamma_s \xi_N}{\xi_E} + 1 \right) \quad (36)$$

And find the constant C_2 is

$$C_2 = \frac{S_0}{\gamma_s + 1} - \frac{1}{\gamma_s + 1} \frac{\gamma_E \xi_N^2 \xi_E^2 E_0^2}{\xi_E^2 - 4\xi_N^2} \left(\frac{2\gamma_s \xi_N}{\xi_E} + 1 \right) \quad (37)$$

We substitute for C_2 into our general solution to obtain

$$S(z) = \frac{S_0}{\gamma_s + 1} e^{-\frac{z}{\xi_N}} - \frac{1}{\gamma_s + 1} \frac{\gamma_E \xi_N^2 \xi_E^2 E_0^2}{\xi_E^2 - 4\xi_N^2} \left(\frac{2\gamma_s \xi_N}{\xi_E} + 1 \right) e^{-\frac{z}{\xi_N}} + \frac{\gamma_E \xi_N^2 \xi_E^2 E_0^2}{\xi_E^2 - 4\xi_N^2} e^{-2\frac{z}{\xi_E}} \quad (38)$$

The equation can be written as the sum of an electric field-free contribution and a field-induced contribution. In the case where we set the electric field equal to zero, we arrive at an equation derived by Stark *et al*. (21) for the profile of a surface-induced nematic with no electric field contribution.

$$S(z) = \frac{S_0}{\gamma_s+1} e^{-\frac{z}{\xi_N}} + \frac{\gamma_E \xi_N^2 \xi_E^2 E_0^2}{\xi_E^2 - 4\xi_N^2}\left(e^{-2\frac{z}{\xi_E}} - \frac{1}{\gamma_s+1}\left(\frac{2\gamma_s\xi_N}{\xi_E}+1\right)e^{-\frac{z}{\xi_N}}\right) \quad (39)$$

We note that there is a discontinuity in the above equation when $\xi_E = 2\xi_N$. This is a so-called removable discontinuity as the limit as ξ_E approaches $2\xi_N$ is finite. If S(z) must be calculated at the discontinuity, the limit upon approaching this point should be used instead. The field-induced contribution to S(z) is always positive for reasonable values of the material parameters.

Estimation of the Ordering of Isotropic 5CB due to Electric Fields Associated with LSPR

We sought to estimate the role of electric fields generated from LSPR on ordering of 5CB near 85±7 nm gold nanoparticles illuminated with green light. This combination of size and color filter leads to the strongest predicted field enhancements for this study. To determine the parameters for the electric field (E_0 and ξ_E), we calculated the electric field enhancement near a spherical gold nanoparticle using the DDA (17) (Figure 4-4c-e). We measured the incident intensity of green light to be 300 W/cm^2 (equivalent to 340 V/cm). Combining the measured incident electric field of the green light with the predicted enhancement of the electric field by 85 nm gold nanoparticles, we determined the maximum of the electric field strength due to LSPR around an 85±7 nm gold nanoparticle to be 3000 W/cm^2 (3400 V/cm). Using Eq. 1, the change in the scalar order parameter of 5CB at 36˚C is of the order of 10^{-6}. For comparison, we calculate that the scalar order parameter of 5CB at 36˚C to be 0.16 at a distance of 5 nm from the 85 nm gold nanoparticle surface due to surface induced ordering (At 36˚C, we observe gold nanoparticles with a mixed thiol monolayer to have a surface induced wetting layer of up to

5±2 nm in 5CB when illuminated with red light). Our calculations lead us to conclude that the electric fields associated with LSPR are too weak to cause the formation of an ordered solvent corona around our nanoparticles.

Effect of Morphology of Gold Nanoparticles on the Electric Field Associated with LSPR and Ordering of Isotropic 5CB

Electron micrographs of the nanoparticles used in our experiments reveal (Figure 4-1a and 4-1b) that the particles have facets and edges that are not considered in the above-described DDA calculations performed assuming a spherical geometry. Previous studies of metal nanoparticles with complex shapes including spheroids, trigonal prisms, and rods have reported (47-49) that the electric field enhancement are maximal near regions of high curvature on nanoparticle surfaces. In particular, silver triangular prisms (47) have a maximum enhancement of the electric field intensity at the particle tips of 59 for particles with a side length of 60 nm and thickness 12 nm (49). For comparison, silver spheres with diameters of 60 nm and 120 nm have a calculated maximum field enhancement of 10 and 6, respectively (48). The surface plasmons of silver triangular prisms have been imaged with electron energy-loss spectroscopy and confirm that areas of sharp edges on lead to increased field enhancement local to the edge (50). These studies show that the value of the maximum field enhancement depend on both the size and shape of the particles as well as the sharpness of the edge, however, in all cases particles with areas of high curvature tend to exhibit electric field enhancements several thousand times the applied field intensity. If we assume an enhancement of 69 of the near surface electric field near the edge of a facet on our gold nanoparticle, we predict that the change in the scalar order parameter due to illumination with green light 10 nm from the particle surface is 0.0004 which is still two orders of magnitude smaller than the predicted ordering due to the surface induced nematic. We conclude that the near particle electric fields due to the formation of a LSPR are too

weak to generate the ordered solvent corona around our gold nanoparticles. As discussed in the main text, the wavelength-dependence of the change in hydrodynamic sizes of the nanoparticles also does not support a direct role for LSPR.

4.9 Additional Discussion of the Role of Electric Fields Associated with the Separation of Hot Electrons and Holes

Calculating the Diffusion Coefficients of Hot electrons and Holes in Gold

The velocities of hot electrons and holes due to thermal motion can be calculated as

$$v_{th} = \sqrt{\frac{3kT}{m}} \quad (40)$$

where k is Boltzmann's constant, T is the absolute temperature, and m is the apparent mass of an electron in the conduction or valence band. For the calculation of the velocity of holes, we use the effective mass of an electron located the valence band ($m = 3.7m_e$; m_e is the electron rest mass). For the calculation of the velocity of hot electrons, we use the effective mass of an electron in the conduction band ($m = 0.22m_e$) (51). The flux of electronic charge, $J_{e,diff}$ is given by.

$$J_{e,diff} = qD_e \frac{dn}{dx} \quad (41)$$

where q is the elementary charge, D_e is the diffusion coefficient of the electrons, and $\frac{dn}{dx}$ is the special gradient in the number density, n, of electrons. The diffusion coefficient can be calculated from

$$D_e = \frac{kT}{q}\mu \quad (42)$$

where μ is the mobility of the electrons.

$$\mu = \frac{q\tau}{m} \quad (43)$$

where τ is the average time between collisions which can be related to the mean-free path of the electrons.

$$L = \tau v_{th} \quad (44)$$

The mean free path of a conduction electron has been measured to be 50 nm whereas the mean free path of a hole has been measured to be 5 nm (52, 53). We calculate the diffusion coefficient at T = 310 K for hot electrons to be 41.4 cm^2/s and for holes to be 1.01 cm^2/s.

Calculating the Effect of Hot Electron-Hole Pairs on the Ordering of Isotropic 5CB

We have constructed a simple model to estimate the extent of solvent ordering due to electric fields generated by the charge-separated state of the nanoparticles. Because of the above-calculated differences in diffusivities, on the time-scale of the lifetimes of hot electrons, we calculate that the hot electrons are to distribute uniformly across the particle surface and the hot holes are localized. This process leads to the creation of charge-separated states on the surfaces of the particles. We estimate the electric field generated by these two oppositely charged surfaces of the nanoparticle as a charge dipole. To model the electric field, we assume a sphere with diameter (d_0) bisected by a plane (defined as $\theta = \pi/2$) (Below the plane, the sphere has surface charge density (σ_0) and above the plane, the sphere has the opposite charge density ($-\sigma_0$) (Figure 4-13). The integral of the charge density over the entire surface is 0 in agreement with charge conservation. Due to symmetry, we do not need to consider changes in the r and θ directions. There exists a charge dipole moment (**p**) such that

$$\mathbf{p} = \int \sigma(\theta) r \, dA \quad (45)$$

Where

$$\sigma(\theta) = \left\{\sigma_0, 0 < \theta < \frac{\pi}{2} \textbf{ and } -\sigma_0, \frac{\pi}{2} < \theta < \pi\right\} \quad (46)$$

and

$$dA = \frac{1}{2}\pi d_0^2 \textbf{sin}\theta d\theta \quad (47)$$

This leads to

$$|\mathbf{p}| = \frac{1}{4}\pi d_0^3 \sigma_0 \quad (48)$$

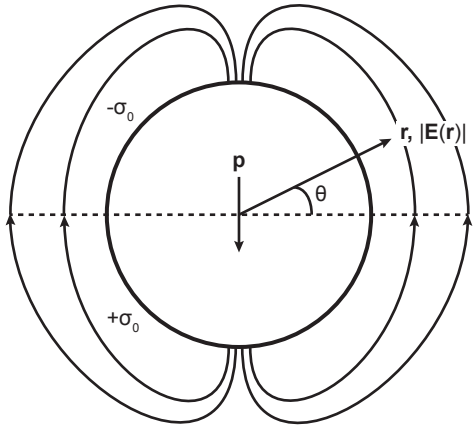


Figure 4 - 13. A sphere with diameter d bisected by a plane (dotted line). The two surfaces of the sphere created separated by the plane have opposite surface charge densities ($\pm\sigma_0$). The two charged surfaces create a dipole moment (**p**) and the electric field due to the charge dipole at some location **r** is **E**(r).

The charge dipole generates an electric field given as

$$\mathbf{E}(\mathrm{r}) = \frac{1}{4\pi\varepsilon_0|\mathbf{r}|^3}\left((3\mathbf{p}\cdot\hat{\mathbf{r}})\hat{\mathbf{r}} - \mathbf{p}\right) \quad (49)$$

where $\hat{\boldsymbol{r}}$ is a unit vector pointing in the direction of **r**. For simplicity, we consider electric fields in a location **r** that is parallel to **p**. Electric fields at this location are expected to have the greatest impact on our measured diffusion coefficients as the location is orthogonal to the measured plane of diffusion (focal plane). The magnitude of the electric field at this location can be calculated as

$$|\mathbf{E}(\mathrm{r})| = \frac{\mathrm{d}_0^3\sigma_0}{8\varepsilon_0|\mathbf{r}|^3} \quad (50)$$

where |**r**| is the distance from the center of the sphere. If we wish to consider electric fields some distance z relative to the sphere surface, Eq. 50 can be rewritten as

$$|\mathbf{E}(\mathrm{r})| = \frac{\mathrm{d}_0^3\sigma_0}{\varepsilon_0(2\mathrm{z}+\mathrm{d}_0)^3} \quad (51)$$

Next, to determine the electric field strength near a 164 nm gold nanoparticle, we first determine the surface charge density σ_0 due to the generation of hot electron-hole pairs. The density of electrons directly excited by an incident blue light illumination can be expressed as

$$\mathrm{c_{he}} = \frac{3\mathrm{I}\lambda\mathrm{Q}_{abs}(\lambda)\mathrm{t}}{2\mathrm{d}_0\mathrm{hc}} \quad (52)$$

where I is the intensity of the incident illumination, λ is the wavelength of light, $Q_{abs}(\lambda)$ is the absorbance cross section of the gold nanoparticle, t is the average lifetimes of the hot electrons, d_0 is the diameter of the nanoparticle, h is Plank's constant, and c is the speed of light. We calculate that blue light (λ = 450 nm) with an intensity of 300 W/cm^2 will excite 2x10^{15} hot electrons/cm^3. These directly excited hot electron-hole pairs will produce additional secondary hot electrons due to the Auger scattering of the holes (31, 54). We estimate the Auger scattering rate for holes in gold to be ~20 fs through a linear interpolation of scattering data from tungsten and mercury (55). By comparing the magnitude of the Auger scattering rate to the hot electron

lifetime, we estimate that Auger scattering will increase the total hot electron density by ~10^2. Assuming that all of the excited hot electrons distribute uniformly along the sphere surface, we calculate a surface charge density of $\sigma_0 = 8.8\text{x}10^{-4}$ C/m^2 (corresponding to 0.0055 electrons/nm^2). From Eq. 52, we calculate that the electric field strength 10 nm from the nanoparticle surface to be $5.2\text{x}10^5$ V/cm. Using Eq. 1, we calculate that this electric field strength at 40˚C (5˚C above T_{NI}) to increase the order parameter of 5CB from 0 to 0.27 at a distance 10 nm from the nanoparticle surface. For comparison, the order parameter of 5CB at a temperature 0.15˚C below the bulk clearing temperature is 0.35 which is similar to the predicted increase in ordering due to an electric field associated with the formation of hot electron-hole pairs (56). From this simple model, we calculate that hot electrons and hot holes in functionalized gold particles can generate electric fields of sufficient strength to create an ordered solvent corona near a gold particle surface.

Calculation of the Wavelength Dependence for the Excitation of Hot Electrons

The total power absorbed by a gold nanoparticle, Q, can be related to the imaginary component of the dielectric constant of gold (57)

$$Q = \frac{\omega}{2\pi} \mathrm{Im}(\varepsilon) \int \mathbf{E} \cdot \mathbf{E} dV \qquad (53)$$

where **E** is the complex electric field within the nanoparticle, V is the volume of the particle, ε is the dielectric constant of gold, and ω is the angular frequency of light. The imaginary component of the dielectric constant can be written as the sum of two contributions,

$$\mathrm{Im}(\varepsilon) = \mathrm{Im}(\varepsilon_{\mathrm{interband}}) + \mathrm{Im}(\varepsilon_{\mathrm{intraband}}) \qquad (54)$$

The two contributions to the dielectric constant of gold represent the two mechanisms by which light is absorbed by a nanoparticle. There is an interband contribution which describes the excitation of hot electrons and an intraband contribution which does not result in the excitation of hot electrons.

$$Q = Q_{interband} + Q_{intraband} = \frac{\omega}{2\pi}\mathrm{Im}(\varepsilon_{interband}) \int \mathbf{E}\cdot\mathbf{E}dV + \frac{\omega}{2\pi}\mathrm{Im}(\varepsilon_{intraband}) \int \mathbf{E}\cdot\mathbf{E}dV \quad (55)$$

Above, we described numerical evaluation of the absorption efficiency, Q_{abs}, of gold nanoparticles of various. The absorption efficiency that results in the formation of hot electrons $Q_{abs,HE}$ is

$$Q_{abs,HE} = Q_{abs}\frac{\mathrm{Im}(\varepsilon_{interband})}{\mathbf{Im}(\varepsilon_{interband})+\mathbf{Im}(\varepsilon_{intraband})} \quad (56)$$

We calculated $\varepsilon_{intraband}$ from a Drude model.

$$\varepsilon_{intraband} = \varepsilon_0 - \frac{\omega_p^2}{\omega(\omega+i\Gamma_{bulk})} \quad (57)$$

where ω_p = 8.9 eV is the plasma frequency of gold and Γ_{bulk} = 0.076 eV is the damping constant of gold. We calculated $\varepsilon_{interband}$ by subtracting $\varepsilon_{intraband}$ from experimentally measured values of the dielectric constant of gold.

A Simple Model for Hot Electron Formation in a Thiol Functionalized Gold Nanoparticle

We can describe the accumulation hot electrons in a gold nanoparticle with the following simple model.

$$\frac{dx}{dt} = P(E,x) - D(x) \quad (58)$$

where x is the number of hot electron-hole pairs, P(E) is the rate of production of hot electrons as a function of irradiance, E, and D(x) is the rate of decay of hot electrons back to the ground state.

As discussed above, the rate of production of hot electrons can be described as the sum of two contributions: (i) direct excitation of hot electrons due to the incident illumination and (ii) the excitation of secondary hot electrons though Auger scattering of the holes (31, 54).

$$P(E,x) = E_{QF}aN_A + 0.05fs^{-1} * \mathrm{floor}(x) \quad (59)$$

where E_{QF} is the quantum flux of photons, a is the extinction cross section of the particle, and N_A is Avogadro's Number. For this calculation, the auger scattering rate (55) is taken to be 0.05 fs^{-1} and the floor(…) function rounds down to the nearest integer. We assume here that each incident photon is able to excite one hot electron.

The lifetime of hot electrons was measured to be ~10-100 fs for gold (28) and by Weiss and coworkers (29) to be 5 ps for an alkane thiol functionalized gold nanoparticle. A value of 10 ps for hot electron lifetimes is used in this calculation as it best fits our experimental measurements shown in Fig. 4. We note that this value is close to the measured value for hot electron lifetime in thiol functionalized gold nanoparticles reported by Weiss et al. (29) We assume that an alkane thiol functionalized gold nanoparticle has a finite number of energy levels which can be occupied by hot electrons (A) and a hot electron will always migrate to the surface if a sight is available because it is a more stable energy level than bulk gold. The lifetime of a hot electron in bulk gold is taken to be 10 fs and the lifetime of a hot electron occupying a surface energy level is 10 ps. Thus D(x) can be written as

$$\begin{gathered} D(x) = 0 \quad \text{if } x = 0 \\ D(x) = 0.0001\ fs^{-1} * \text{ceil}(x) \quad \text{if } 0 < x < A \\ D(x) = 0.1\ fs^{-1} * \text{ceil}(x - A) + 0.0001\ fs^{-1}\, A \quad \text{if } x > A \end{gathered} \tag{60}$$

where the ceil(…) function rounds up to the nearest integer and prevents fractional values of x from producing large lifetimes of hot electrons which is unphysical. The extinction efficiency of a 164 nm gold particle was calculated to be 2.8 with 450 nm light using a discrete dipole approximation. Note that the extinction cross section does not change appreciably between 430 nm light and 470 nm light which is used in our experiments. The selection of a different wavelength in this range does not significantly affect our result. The quantum flux of light is proportional to the irradiance of light in W/cm^2 which can be measured with a light meter. The

results are non-dimensionalized by dividing x by A so our choice for the number of surface binding sights does not affect the result.

We find that above at zero (450 nm) light intensity, there are no hot electrons. As the intensity of 450 nm light is increased, we see no significant accumulation of hot electrons until a threshold light intensity is reached (Fig. 4). The threshold light intensity is 75 W/cm^2 and is governed by the lifetime of hot electrons in the surface absorbed alkane thiol monolayer. Above this threshold, the monolayer is saturated and the number of hot electrons is again independent of the blue light intensity. We project this trend to continue until the light intensity reaches 7500 W/cm^2, where we predict the number of hot electrons to increase beyond the available binding sights on the surface of the particle.

4.10 References

1. Sasaki S (1984) Effect of Simple Electrolytes on the Hydrodynamic Radius of Polystyrene Latex. *Colloid Polym Sci* 262(5):406-408.

2. Lee JC & Timasheff SN (1981) The Stabilization of Proteins by Sucrose. *J Biol Chem* 256(14):7193-7201.

3. Randolph TW, Blanch HW, & Prausnitz JM (1988) Enzyme-Catalyzed Oxidation of Cholesterol in Supercritical Carbon-Dioxide. *Aiche J* 34(8):1354-1360.

4. Wuttke R*, et al.* (2014) Temperature-Dependent Solvation Modulates the Dimensions of Disordered Proteins. *Proc Natl Acad Sci U S A* 111(14):5213-5218.

5. Giovambattista N, Rossky PJ, & Debenedetti PG (2006) Effect of Pressure on the Phase Behavior and Structure of Water Confined Between Nanoscale Hydrophobic and Hydrophilic Plates. *Phys Rev E* 73(4):1-14.

6. Schultz SG & Solomon AK (1961) Determination of the Effective Hydrodynamic Radii of Small Molecules by Viscometry. *J Gen Physiol* 44:1189-1199.

7. Horn RG & Israelachvili JN (1981) Direct Measurement of Structural Forces between 2 Surfaces in a Non-Polar Liquid. *J Chem Phys* 75(3):1400-1411.

8. Velasco-Velez JJ*, et al.* (2014) The Structure of Interfacial Water on Gold Electrodes Studied by X-ray Absorption Spectroscopy. *Science* 346(6211):831-834.

9. Ostroverkhov V, Waychunas GA, & Shen YR (2005) New Information on Water Interfacial Structure Revealed by Phase-Sensitive Surface Spectroscopy. *Phys Rev Lett* 94(4):1-4.

10. Chandler D (2005) Interfaces and the Driving Force of Hydrophobic Assembly. *Nature* 437(7059):640-647.

11. Abras D, Pranami G, & Abbott NL (2012) The Mobilities of Micro- and Nano-Particles at Interfaces of Nematic Liquid Crystals. *Soft Matter* 8(6):2026-2035.

12. Bottger A, Frenkel D, Vanderiet E, & Zijlstra R (1987) Diffusion of Brownian Particles in the Isotropic-Phase of a Nematic Liquid-Crystal. *Liq Cryst* 2(4):539-547.

13. Kocevar K & Musevic I (2001) Forces in the Isotropic Phase of a Confined Nematic Liquid Crystal 5CB. *Phys Rev E* 64(5):1-8.

14. Hogan NJ*, et al.* (2014) Nanoparticles Heat through Light Localization. *Nano Lett* 14(8):4640-4645.

15. Hutter E & Fendler JH (2004) Exploitation of Localized Surface Plasmon Resonance. *Adv Mater* 16(19):1685-1706.

16. Shan J, Shi W, Liu LY, Shen YR, & Xu L (2012) Optical Control of Surface Anchoring and Reorientation of Liquid Crystals via a Plasmon-Enhanced Local Field. *Phys Rev Lett* 109(14):1-5.

17. Draine BT & Flatau PJ (1994) Discrete-Dipole Approximation for Scattering Calculations. *J Opt Soc Am A* 11(4):1491-1499.

18. Haiss W, Thanh NTK, Aveyard J, & Fernig DG (2007) Determination of Size and Concentration of Gold Nanoparticles from UV-Vis Spectra. *Anal Chem* 79(11):4215-4221.

19. de Gennes PG (1974) *The Physics of Liquid Crystals* (Clarendon Press, Oxford Eng.) p 333.

20. Zakharov AV & Dong RY (2001) Dielectric and Elastic Properties of Liquid Crystals. *Phys Rev E* 64(3):1-9.

21. Stark H (2001) Physics of colloidal dispersions in nematic liquid crystals. *Phys Rep* 351(6):387-474.

22. Kreibig U & Vollmer M (1995) *Optical Properties of Metal Clusters* (Springer, Berlin ; New York) p 532.

23. Mukherjee S*, et al.* (2013) Hot Electrons Do the Impossible: Plasmon-Induced Dissociation of H-2 on Au. *Nano Lett* 13(1):240-247.

24. Weiss C, Wallenstein R, & Beigang R (2000) Magnetic-Field-Enhanced Generation of Terahertz Radiation in Semiconductor Surfaces. *Appl Phys Lett* 77(25):4160-4162.

25. Ramakrishnan G, Chakkittakandy R, & Planken PCM (2009) Terahertz Generation from Graphite. *Opt Express* 17(18):16092-16099.

26. Dember H (1931) Uber Eine Photoelektronische Kraft in Kupferoxydul-Kristallen. *Phys. Zeits.* 32:554-557.

27. Held T, Kuhn T, & Mahler G (1991) Influence of Internal Electric-Fields and Surface-Charges on the Transport of an Optically Generated Electron-Hole Plasma. *Phys Rev B* 44(23):12873-12879.

28. Ladstadter F, Hohenester U, Puschnig P, & Ambrosch-Draxl C (2004) First-Principles Calculation of Hot-Electron Scattering in Metals. *Phys Rev B* 70(23):1-10.

29. Aruda KO*, et al.* (2013) Identification of Parameters Through which Surface Chemistry Determines the Lifetimes of Hot Electrons in Small Au Nanoparticles. *P Natl Acad Sci USA* 110(11):4212-4217.

30. Koenig GM, Gettelfinger BT, de Pablo JJ, & Abbott NL (2008) Using localized surface plasmon resonances to probe the nanoscopic origins of adsorbate-driven ordering

transitions of liquid crystals in contact with chemically functionalized gold nanodots. *Nano Lett* 8(8):2362-2368.

31. Knoesel E, Hotzel A, & Wolf M (1998) Ultrafast Dynamics of Hot Electrons and Holes in Copper: Excitation, Energy Relaxation, and Transport Effects. *Phys Rev B* 57(20):12812-12824.

32. Hayes JR, Levi AFJ, & Wiegmann W (1985) Hot-Electron Spectroscopy of GaAs. *Phys Rev Lett* 54(14):1570-1572.

33. Voitchovsky K (2013) Anharmonicity, Solvation Forces, and Resolution in Atomic Force Microscopy at the Solid-Liquid Interface. *Phys Rev E* 88(2):1-6.

34. Idziak SHJ*, et al.* (1994) The X-Ray Surface Forces Apparatus - Structure of a Thin Smectic Liquid-Crystal Film under Confinement. *Science* 264(5167):1915-1918.

35. Apostolopoulos V & Barnes ME (2014) THz Emitters Based on the Photo-Dember Effect. *J Phys D Appl Phys* 47(37):1-16.

36. Schneider CA, Rasband WS, & Eliceiri KW (2012) NIH Image to ImageJ: 25 years of image analysis. *Nat Methods* 9(7):671-675.

37. Sbalzarini IF & Koumoutsakos P (2005) Feature point tracking and trajectory analysis for video imaging in cell biology. *J Struct Biol* 151(2):182-195.

38. Michalet X (2010) Mean Square Displacement Analysis of Single-Particle Trajectories with Localization Error: Brownian Motion in an Isotropic Medium. *Phys Rev E Stat Nonlin Soft Matter Phys* 82(4 Pt 1):1-13.

39. Koenig GM, Meli MV, Park JS, de Pablo JJ, & Abbott NL (2007) Coupling of the plasmon resonances of chemically functionalized gold nanoparticles to local order in thermotropic liquid crystals. *Chem Mater* 19(5):1053-1061.

40. Johnson PB & Christy RW (1972) Optical Constants of Noble Metals. *Phys Rev B* 6(12):4370-4379.

41. Sleijpen GLG & VanderVorst HA (1995) An overview of approaches for the stable computation of hybrid BiCG methods. *Appl Numer Math* 19(3):235-254.

42. Pan RP, Hsieh CF, Pan CL, & Chen CY (2008) Temperature-Dependent Optical Constants and Birefringence of Nematic Liquid Crystal 5CB in the Terahertz Frequency Range. *J Appl Phys* 103(9):1-7.

43. Vieweg N & Koch M (2010) Terahertz Properties of Liquid Crystals with Negative Dielectric Anisotropy. *Appl Optics* 49(30):5764-5767.

44. Blinov LM & Chigrinov VG (1994) *Electrooptic Effects in Liquid Crystal Materials* (Springer-Verlag, New York) p 464.

45. Osborne MA, Balasubramanian S, Furey WS, & Klenerman D (1998) Optically Biased Diffusion of Single Molecules Studied by Confocal Fluorescence Microscopy. *J Phys Chem B* 102(17):3160-3167.

46. Schlenoff JB, Li M, & Ly H (1995) Stability and self-Exchange in Alkanethiol Monolayers. *J Am Chem Soc* 117(50):12528-12536.

47. Hao E & Schatz GC (2004) Electromagnetic Fields around Silver Nanoparticles and Dimers. *J Chem Phys* 120(1):357-366.

48. Kelly KL, Coronado E, Zhao LL, & Schatz GC (2003) The optical properties of metal nanoparticles: The influence of size, shape, and dielectric environment. *J Phys Chem B* 107(3):668-677.

49. Sarid D & Challener WA (2010) *Modern Introduction to Surface Plasmons : Theory, Mathematica modeling, and Applications* (Cambridge University Press, Cambridge ; New York) p 371.

50. Nelayah J*, et al.* (2007) Mapping Surface Plasmons on a Single Metallic Nanoparticle. *Nat Phys* 3(5):348-353.

51. Christensen NE & Seraphin BO (1971) Relativistic Band Calculation and Optical Properties of Gold. *Phys Rev B-Solid St* 4(10):3321-3344.

52. Link S & El-Sayed MA (2000) Shape and Size Dependence of Radiative, Non-Radiative and Photothermal Properties of Gold Nanocrystals. *Int Rev Phys Chem* 19(3):409-453.

53. Motizuki K & Sparks M (1964) Range of Excited Electrons and Holes in Metals and Semiconductors. *Journal of the Physical Society of Japan* 19(4):1-13.

54. Perner M*, et al.* (1997) Optically Induced Damping of the Surface Plasmon resonance in Gold Colloids. *Phys Rev Lett* 78(11):2192-2195.

55. Chen MH, Crasemann B, & Mark H (1979) Relativistic Radiationless Transition Probabilities for Atomic K- and L-shells. *Atom Data Nucl Data* 45(1):13-37.

56. Lelidis I & Durand G (1993) Electric-Field-Induced Isotropic-Nematic Phase-Transition. *Phys Rev E* 48(5):3822-3824.

57. Govorov AO, Zhang H, Demir HV, & Gun'ko YK (2014) Photogeneration of Hot Plasmonic Electrons with Metal Nanocrystals: Quantum Description and Potential Applications. *Nano Today* 9(1):85-101.

Chapter 5

Influence of Size and Surface Chemistry on the Mobility of Nanoparticles Dispersed in Nematic Liquid Crystals

5.1 Abstract

By using single-particle tracking, we report measurements of the size-dependent mobility of chemically functionalized gold and silica nanoparticles in a nematic phase of 4-pentyl-4-cyanobiphenyl (5CB). The measured apparent viscosity of gold nanoparticles in a range of sizes from 85±7 nm to 380±30 nm is substantially different from that of microscale-sized silica particles with the same surface anchoring conditions. We also confirm this change by comparing the apparent viscosities of 391±33 nm and 1.2±0.1 μm silica particles with the same surface chemistry. However, no change in apparent viscosity is observed over the range of nanoscale gold particles with chemical functionality giving rise to either perpendicular or planar anchoring. We do note a change in apparent viscosity between the two populations of gold particles with different surface chemistries. These results can be interpreted as a size dependent change in local ordering of the liquid crystal as particle size decreases from 1.2±0.1 μm to 391±33 nm with no measureable change observed over the range of 391±33 nm down to 85±7 nm. The local ordering of a liquid crystal about nanoscale particles is observed to be influenced by the particle surface chemistry.

5.2 Introduction

A number of studies have reported experimental and theoretical investigations of the dynamic and equilibrium behaviors of colloidal microparticles dispersed in nematic liquid crystals (LCs). In particular, measurements of the mobility of micrometer-sized particles have been found to be in close agreement with theory, confirming the key observation that the mobility of such particles is strongly influenced by surface induced ordering of the LC in the vicinity of the particles. In contrast to micrometer-sized particles, measurements of the diffusion coefficients of nanoscopic particles have yielded values that are higher than predicted by theory (1). The experimental investigation reported here was performed to provide further characterization of the mobility of nanoscale particles in LCs and to provide insight into the origins of the deviations between theory and experiment on the nanoscale.

For micrometer-sized particles dispersed in a nematic phase, the local ordering of liquid crystal in the vicinity of the particle can be directly characterized by bright-field and polarized light microscopy. This ordering can also be predicted by the minimization of the free energy of the LC under the constraints presented by the boundary conditions at the particle surface and in the far field. These ordered states are characterized by the presence of topological defects, a consequence of the fact that the boundary conditions cannot be satisfied by continuous strain of the director. For micrometer-sized particles with weak, homeotropic anchoring, line defects (so-called disclinations of strength -1/2) form off the equator of the particle (similar to a ring of the planet Saturn; Figure 5-1b), leading to an ordered state of the LC that possesses quadrupolar symmetry. In contrast, when the anchoring of the LC at the surface corresponds to strong, homeotropic anchoring, a point defect (strength -1) is formed (a so-called Hedgehog defect; Figure 5-1a), leading to an ordered state of the LC with dipolar symmetry. Alternatively, surface-

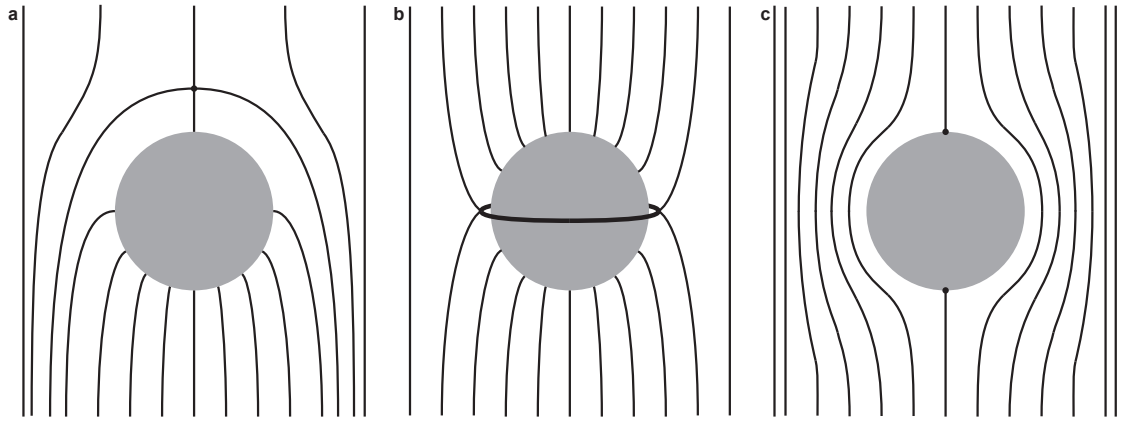


Figure 5 - 1. Diagram of various defect structures for micrometer-scaled particles. The far-field director is shown (right). (a) Hedgehog defect for strong, perpendicular anchoring of the liquid crystal at the particle surface. It is dipolar in nature and contains a single point defect. (b) Saturn ring defect for weak, perpendicular anchoring at the particle surface. The structure is quadrupolar in nature and contains a line disclination. (c) Boojum defect for planar anchoring of the liquid crystal at the particle surface. It is quadrupolar in nature and contains two point defects.

associated defects, so-called Boojums (strength -1/2) are formed when the particle surface causes planar anchoring of the LC, leading overall to an ordered state of the LC with quadrupolar symmetry (Figure 5-1c). In contrast to these rather well-understood states of the ordering of LCs about micrometer-sized particles, because direct imaging is not possible, relatively little is known from experiments about the ordering of LCs about nanoparticles.

Although direct imaging of the ordering of LCs about nanoscopic particles is not possible, measurements of the mobilities of particles can be used to infer information about the local ordering of LCs. For example, on the micrometer-scale, the mobility of particles dispersed in liquid crystal phases have been characterized in experimental studies of surfactant-stabilized oil droplets (2) and solid particles (3-8) and theoretical studies of solid microparticles with different types of surface anchoring (9-13). These studies, when combined, established that the ordering of the LC about the particles, including the type of defect structure formed, directly influences particle motion. Interpretation of measurements of mobility of particles in LCs requires consideration of the anisotropic viscosity of an LC, which is commonly described in terms of three Miesowicz shear viscosities. The largest of the viscosities (ν_c) corresponds to shear perpendicular to the director, whereas the smallest (ν_b) corresponds to shear parallel to the director. The intermediate viscosity (ν_a) corresponds to shear perpendicular to shear in the plane of the director field. We expect that different sized particles will have different diffusion coefficients. However, if there is no change in the defect structure, differently sized microparticles should have the same apparent viscosity since the defect scales with the particle size. The influence of the director on the apparent viscosity can be understood from Figure 5-1 considering a particle translating perpendicular to the far-field director.

Particle motion will generate a flow field about the particle. The flow field will sample the various Miesowicz shear viscosities depending on the local orientation of the shear with respect to the director. A change in the apparent viscosity of the particle in the medium will indicate a change in the local ordering about the liquid crystal since the shear flow generated by the particle motion will sample different director configurations.

As mentioned above, for nanoscale particles, it is not possible to directly image the defects and ordering of LC surrounding the nanoparticles. It is, however, possible to probe the local ordering of the LCs indirectly via measurement of the mobility of the particles and pairwise interactions between nanoparticles. In particular, Koenig *et al.* have reported experimental measurements of the mobility of gold nanoparticles with diameters of 169±16 nm and surface chemical functionalization leading to either perpendicular or parallel anchoring of nematic 5CB (1). These measurements revealed that (i) the surface chemistry of the nanoparticles strongly influenced their mobility, consistent with the surface-induced ordering of LCs of some type on nanoparticles mobility, and that (ii) the values of the measured mobilities were not in agreement with the above-mentioned theoretical predictions of particles in LCs, suggesting that the ordering of LCs about the nanoparticles may differ significantly from the micrometer-scale particles.

The study described in this paper was motivated by the goal of providing further insight into the differences between the mobilities of nanometer-scale and micrometer-sized particles in LCs. Specifically, we aimed to determine how the mobilities of the particles changed with size and surface chemistry, and thus infer the size-dependent ordering of LC about particles in the crossover between the micrometer and nanometer regimes. In this context, we comment that Musevic and coworkers (3) have reported the size-dependent diffusion coefficients of silica

particles with a dimethyloctadecyl [3-(trimethoxysily) propyl] ammonium chloride (DMOAP)-functionalized surface in LCs. They interpret their measurements to indicate that the diffusion coefficient of the DMOAP-functionalized silica particles does not change with size for particles with diameters between 125 nm and 500 nm and that particles with diameters between 500 nm and 2 μm follow the Stokes-Einstein relation. Our measurements obtained using single-particle tracking of chemically functionalized gold particles suggest, in contrast, that diffusion coefficients of nanometer-sized particles do change continuously down to sizes of 85±7 nm (smallest investigated in our study).

5.3 Materials and Methods

Materials

Gold particles with diameters ranging from 80nm to 250nm were obtained from Ted Pella. Gold-coated silica core shell particles 380nm and larger were provided by N. Kotov and were produced using the method described by Halas *et al.* (14). Hexadecanethiol and decanethiol were purchased from Aldrich and used as received. The mesogen, 4-pentyl-4-cyanobiphenyl (5CB) was purchased from EMD chemicals. Glass microscope slides, cover slips, dimethyloctadecyl [3-(trimethoxysily) propyl] ammonium chloride (DMOAP; 60% in methanol), hydrochloric acid, and hydrogen peroxide were purchased from Fisher. Absolute ethanol was obtained from AAPER Alcohol.

Preparation of Nanoparticles

Gold nanoparticles were functionalized with thiol monolayers to determine the surface anchoring of the 5CB. Briefly, 200 μL of gold nanoparticle suspension were washed 3 times by diluting with 2 mL MilliQ water, sedimenting at 5000g for 15 min, and removing the supernatent. Particles are redispersed in 200 μL MilliQ water. Particles were then mixed with either 800 μL 4 mM decanethiol in ethanol or 640 μL 4 mM decanethiol in ethanol/160 μL 4 mM hexadecanethiol in ethanol for 1hr. Gold nanoparticles are sedimented at 5000g for 30 min and redispersed in 2 mL ethanol three times. Particles were then dried in a vacuum for 1 hr and dispersed in 50 μL 5CB.

Preparation of Surfaces

Glass microscope slides were cleaned with an acidic piranha solution for 30min. Slides were rinsed with 18.2 MΩ deionized water ethanol. Substrates were stored in ethanol until use. Substrates were dried with compressed nitrogen and immersed in 45 mL of 18.2 MΩ deionized

water. 1.7 mL of DMOAP was dispersed. The slides in solution were sonicated for 30 min, rinsed with deionized water, and dried with compressed nitrogen. An optical cell was formed with a glass slide and a cover slip separated by a 12 μm thick Mylar film at the periphery of two sided of the cover slip. The cell was held together with an epoxy. The particle suspension in 5CB was heated to the isotropic phase and allowed to flow into the cell through capillary action.

Single-Particle Tracking

We utilized dark-field microscopy to visualize the particle diffusion. A schematic diagram of the experimental setup is provided in Figure 5-2. Incident light enters the sample at an oblique angle such that it does not enter the objective. The sample consists of a 12 μm film of 5CB liquid crystal dispersed with gold nanoparticles. The film is sandwiched between two glass plates with a DMOAP monolayer leading to homeotropic anchoring. When the incident light interacts with a nanoparticle, the light is scattered. The scattering cross section of the particle can be observed as a bright spot on a dark background.

The motion of the particle was tracked with a monochrome camera at a rate of 30 images per second. The motion of the particles undergoing Brownian motion with motion in each direction considered independently follows the function:

$$\mathrm{MSD} = 2D\tau \qquad (1)$$

where MSD is the mean squared displacement of a particle after waiting at time τ, and D is the diffusion coefficient of the particle. The sampling rate for our experiments is 30 Hz.

The effective viscosity of the particle in the medium can be determined from the Stokes-Einstein relation:

$$D = \frac{kT}{3\pi\eta d} \qquad (2)$$

where η is the apparent viscosity of the particle in the medium, k is Boltzmann's constant, T is temperature, d is the particle diameter.

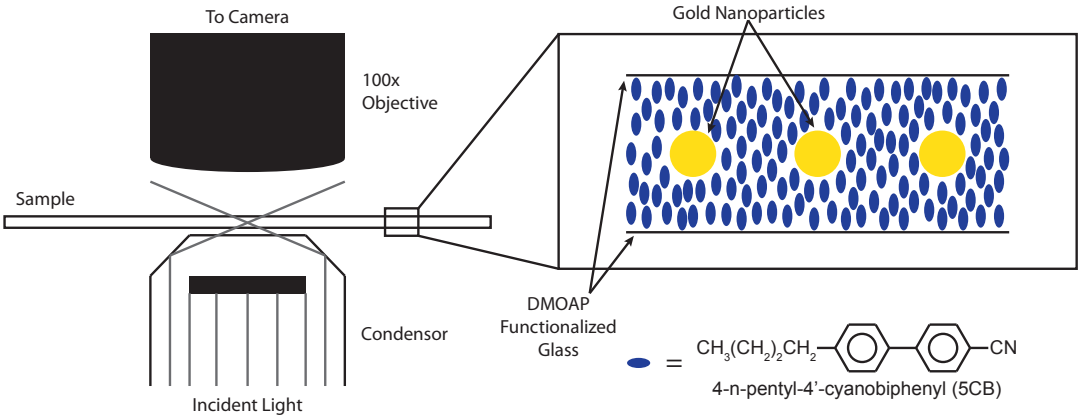


Figure 5 - 2. Experimental set-up for dark-field microscopy and single-particle tracking in nematic liquid crystals.

5.4 Results

Synthesis and Characterization of Particles

We used gold nanoparticles in our experiments aimed at measurement of the size-dependent diffusion of nanoparticles in LCs because (i) the surface properties of the gold nanoparticles can be systematically controlled using monolayers formed from organothiols and (ii) the gold nanoparticles have a large scattering cross-section and are therefore easy to track for particles with sizes less than 400 nm. Gold particles have a range of sizes from 85±7 nm to 380±30 nm. 85±7 nm was the minimum size of the particles with a sufficiently large scattering cross-section that can be reliably tracked with our experimental setup. Gold particles can be purchased in nominal sizes up to 250 nm in sol form. Larger sizes of gold particles are available for purchase but have a comparably large distribution of sizes (approx. ±40%) and have a large amount of amorphous molecules. Gold particles 380±30 nm and larger are gold shelled particles (10 nm shell) with a silica core.

In order to interrogate the mobility of larger molecules and confirm that the size effects are not specific for particles with an organothiol monolayer, we utilize silica particles with a DMOAP monolayer. Silica particles with DMOAP monolayers have homeotropic anchoring at their surface. We measured the mobility of silica particles 1.2±0.1 μm in diameter and 391±33 nm in diameter. Silica particles have a much smaller scattering cross section than similarly sized gold particles. As such, measurements of the particle trajectory with nanometer-sized silica particles were difficult. The 391±33 nm silica particles were the smallest size on which we could perform particle tracking measurements.

We confirmed that the mixed thiol monolayer results in perpendicular anchoring as observed with microscale particles and the single component monolayer results in planar

anchoring with microparticles. As discussed below, it is not possible to image the ordering of the LC about the nanoparticles, and our measurements of diffusion coefficients suggest that the ordering of the LC does change with size of the particles.

Prior to performing single-particle tracking measurements with the gold nanoparticles, we characterized the particles using scanning electron microscopy (SEM) (Figure 5-3). We note that the majority of gold particles are approximately spherical with no discernable eccentricity (Figure 5-3a – 5-3c). The surfaces of the gold nanoparticles are not smooth, but rather contain facets. The facets appear random in both size and shape. We also note the presence of a small population (<5%) of gold particles that appear to have either a triagonal prism or hexagonal prism shape. The particles are approximately the same size as the spheres, however, given the small size of their population, they should not contribute significantly to the results if they exhibit diffusivity different than the spheres. The diameter of each particle was determined by measuring the total cross-sectional area of the particle and calculating the diameter of a circle with equivalent area. The distributions are Gaussian with sizes of 85±7 nm, 140±11 nm, and 239±18 nm, for 80 nm, 150 nm, and 250 nm, respectively. Also of note is the absence of very large and small outliers.

Gold-silica core-shell particles were examined in the same manner as solid gold particles (Figure 5-3d). From the SEM micrographs, we note that these particles do not have a faceted surface like the solid gold particles, but rather have a smooth and featureless surface. There are several particles with a so-called “peanut” morphology where the shells of two particles overlap to form a rod-like structure; however, such aggregates where rare (<0.1%), and will appear as aggregates during mobility measurements.

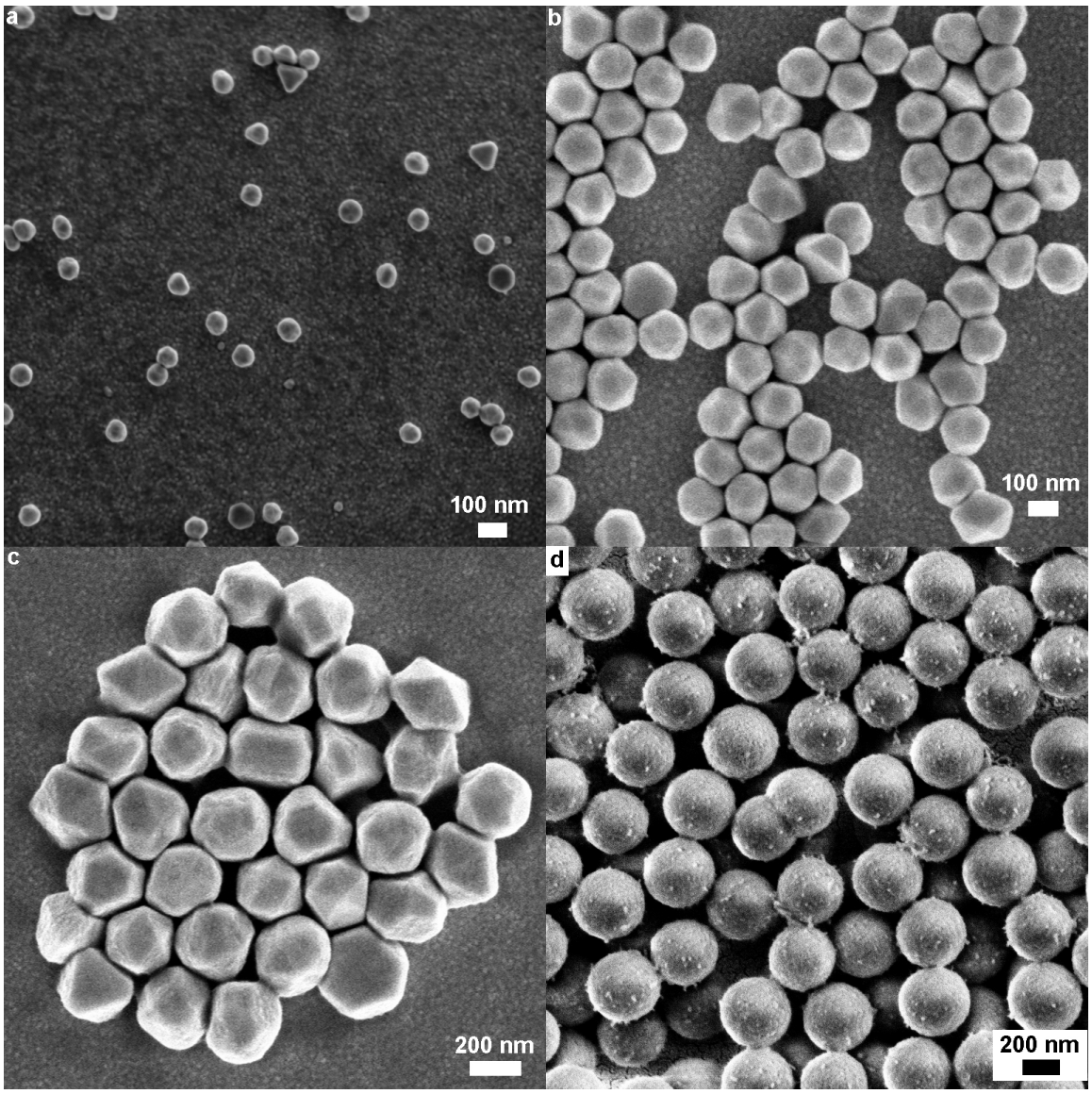


Figure 5 - 3. SEM micrographs of (a) 85±7 nm, (b) 140±11 nm, and (c) 239±18 nm gold nanoparticles. (d) 380±30 nm silica core gold shell nanoparticles.

Silica particles do not exhibit Oswald ripening like we would expect from a gold sol solution. As such, the dimensions of silica particles should be stable over time and we use the manufacturer's measured mean and standard deviation for particle size distribution.

Measurements of Particle Trajectories and Confirmation of Brownian Motion

As described in the Methods section, we used dark field imaging to follow the trajectories of particles in the nematic LCs. To validate our measurement methodology, first we measured the diffusion of 169±16 nm gold particles in water. We measure the diffusion coefficient to be 2.81±0.30 $\mu m^2/s$, which is close to the calculated result from the Stokes-Einstein relation (Equation 2), 2.72±0.16 $\mu m^2/s$. The error bar is consistent with the variation in size of the stock particles.

When measuring the trajectories of the nanoparticles in LCs, we confined the LC between two surfaces that were treated to cause homeotropic anchoring of the LC. In this situation, the particle trajectories are recorded perpendicular to the director. We found that it was necessary to take a number of precautions in order to measure the displacement of the particles due only to Brownian motions. Care must be taken to avoid convective flows in the liquid crystal film. Slow convective flows are often observed when the cell is initially loaded. It takes several hours for these flows to diminish to undetectable levels. In addition, care must be taken not to compress the film with the microscope objective and dark-field condenser during panning and focusing of the microscope. Flows can be readily detected in the case where there is more than one particle in the field of view. If particle motion is due solely to diffusion, the motion of several particles should be completely uncorrelated. If the motion of two or more particles is correlated, that is, they move in approximately the same direction for a large period of time, the presence of convective flows can be inferred. Additionally, particles undergoing Brownian

motion should exhibit mean squared displacement that is linear with the time step. A non-linear result would suggest the particles where under the influence of spurious forces. Figure 5-4 shows the mean squared displacement of the particle, measured for various-sized gold nanoparticles. Results such as these were used to confirm that the particles for which we evaluated diffusion coefficients from particles trajectories were, indeed, undergoing Brownian motion.

The influence of spurious forces can be revealed through the analysis of the MSD versus time step. For example, a small convective flow will cause the MSD to exhibit higher order behavior rather than the expected linear behavior. If the sampling rate is too fast, time step is too small; the particle will not undergo Brownian motion, but rather ballistic motion that manifests as a deviation from linear behavior at very small time steps. Analysis of the MSD provides an objective tool for determining if a particle's motion is due to random fluctuations. Figure 5-4 shows three example measurements of MSD versus time step. The behavior is essentially linear from the experimental time step size of 0.03 s up to 0.5 s showing that the measured diffusion coefficient is free from spurious forces and that the time step is sufficiently large to characterize Brownian motion.

Measurements of Diffusion Coefficients of Single Nanoparticles in LCs.

Figure 5-5 shows the diffusion coefficients and apparent viscosities of single gold nanoparticles in a nematic phase of 5CB for motion perpendicular to the far-field director. For comparison, measurements obtained using micrometer- and nanometer-sized silica particles (DMOAP-treated) are presented. From the results shown in Figure 5-5, we make three principle observations

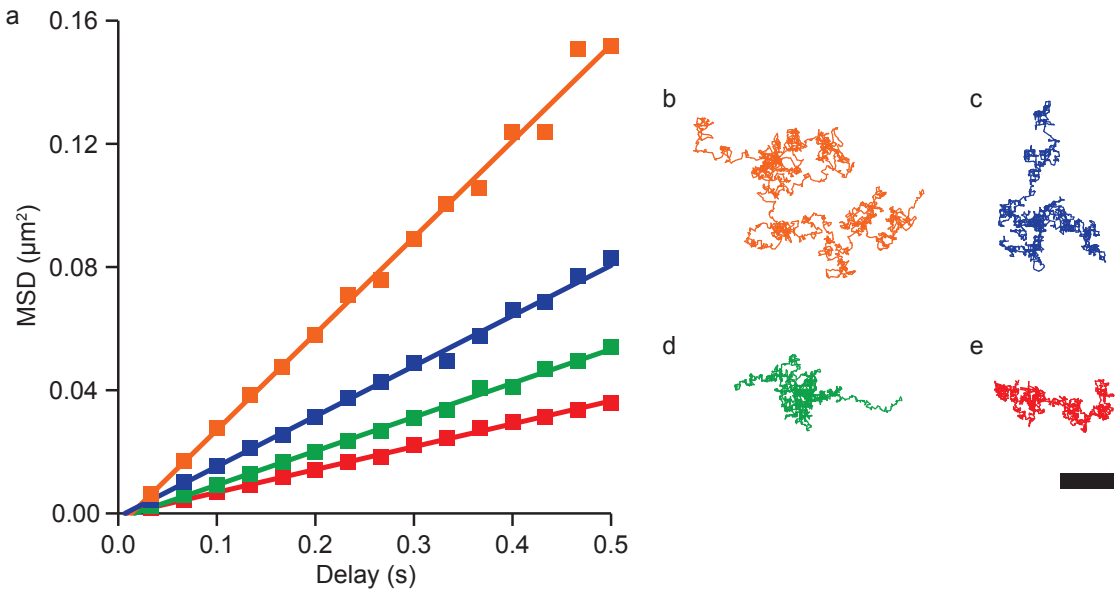


Figure 5 - 4. (a) Representative mean squared displacements (MSD) of nanoparticles with mean diameters (red) 380±10 nm, (green) 239±18 nm, (blue) 140±11 nm, and (orange) 85±7 nm and single component monolayers with respect to delay time. For Brownian diffusion, the MSD with respect to time step to be linear. (b-e) trajectories corresponding to the MSD shown in (a). The scale bar is 2 μm.

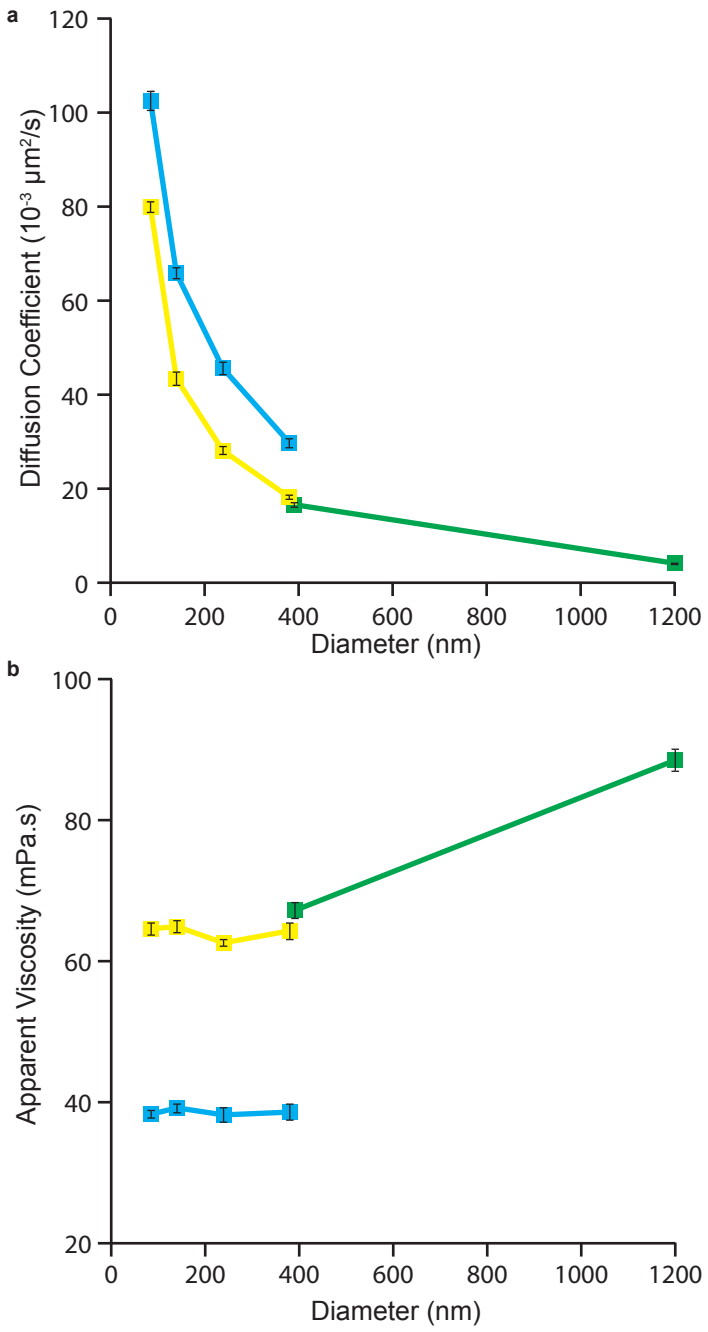


Figure 5 - 5. Diffusion coefficient (a) and apparent viscosity (b) for gold nanopaticles with a mixed thiol monolayer (yellow) and single component monolayer (blue), and silica particles with a DMOAP monolayer (green) of various diameters in 5CB.

First, for the gold nanoparticles functionalized with the mixed monolayer of alkanethiols, we observe the diffusion coefficients to decrease with increase in particle size. The diffusion coefficient is observed to decrease from 0.0799±0.0050 $\mu m^2/s$ for 85.0±6.6 nm particles to 0.0182±0.0020 $\mu m^2/s$ for 380±30 nm particles. When an apparent viscosity is calculated from the measured diffusion coefficient, the apparent viscosity is size-independent for nanoparticles with diameters in the same range. The apparent viscosity is 64.6±4.0 mPa.s for 85.0±6.6 nm particles and 64.3±5.0 mPa.s for 380±10 nm particles. Because the apparent viscosity is dependent on the local ordering of LCs in the vicinity of the nanoparticles, the constant value of the apparent viscosity suggests that the ordering of the LC over this size range does not change with size.

Second, a comparison of apparent viscosity calculated for the gold nanoparticles with the mixed monolayers of alkanethiols to the apparent viscosity of the micrometer-sized DMOAP-treated particles reveals that the apparent viscosity samples by the nanoparticles and the micrometer-sized particles do differ. For the micrometer-scaled DMOAP-treated particles, we observed the optical signature of a Saturn-ring defect. The difference in apparent viscosity sampled by the nanoparticles and microparticles suggests that the Saturn-ring defect is likely perturbed or lost as the size of the particles decreases from 1.2±0.1 μm to 380±30 nm suggesting that the Saturn ring defect has become distorted.

At macroscopic, planar surfaces, both DMOAP-treated silica and gold films treated with mixed alkanethiols will cause homeotropic ordering of the LC. Although the easy axis of the LC is the same at both surfaces, the anchoring energies likely differ and the local ordering of the LC at the particle surface may also differ (the statement that the surfaces cause homeotropic anchoring is regarding the far-field orientation of the LC). We considered it possible, therefore, that the above-mentioned difference between the apparent viscosity sampled by the DMOAP-

treated microparticle and mixed thiol-treated gold particle may arise not from differences in size of the particles but rather differences in the local ordering induced by the surface chemical functionalization. To explore this possibility, we measured the mobility of 391±33 nm diameter silica particles treated with DMOAP. Inspection of Figure 5-5 reveals that (i) the diffusion coefficient of the 391±33 nm DMOAP-treated particle, 0.0166±0.0021 $\mu m^2/s$, is the same as the 380±30 nm diameter gold nanoparticles with a mixed thiol monolayer, 0.0182±0.0020 $\mu m^2/s$, and (ii) the apparent viscosity samples by the 391±33 nm DMOAP-treated particle was significantly different from the micrometer-sized particle. This suggests that the local ordering of LC about the particles does change as the particle size decreases from 1.2±0.1 μm to 391±33 nm, and that the change is seen for both the DMOAP-coated silica and the mixed thiol-treated gold particles.

Here we note also that the apparent viscosity of the 1.20±0.1 μm silica particle is in agreement with numerical results from Stark and coworkers (13). The apparent viscosity of these particles was calculated to be 85.3 mPa.s. This was similar to an experimental result from Poulin and coworkers for 1.1 μm silicon oil droplets with Saturn ring defects in E7 (2). In contrast, as noted above, the apparent viscosity of the nanometer-sized particles is significantly higher than that predicted by the theory of Stark. Stark's simulations calculated particle mobility perpendicular and parallel to the far-field director. Particles had dipole and Saturn ring defects as well as the case of no surface anchoring. Simulations were conducted under the assumption that the Eriksen number (Er) is much less than unity. The Ericksen number is written as:

$$\mathrm{Er} = \frac{\eta v_\infty d}{2K} \qquad (3)$$

were η is the viscosity of the medium, v_∞ is the particle velocity, d is the particle diameter, and K is the one-constant elastic constant for the nematic. Low Ericksen numbers predict that the

viscous forces in the medium are too weak to influence the director in the LC (We calculate for our experiments an Ericksen number of ~10^{-5}). Subsequently, a flow is imposed which considers the viscous stress tensor of the nematic to couple the flow to the liquid crystal. This stress tensor includes information about the Miesowicz shear viscosities. Finally, the friction force is calculated based on the dissipated energy per unit volume. The apparent viscosities both perpendicular and parallel to the far-field director can be determined from the friction force and the diffusion coefficients can be calculated from the respective apparent viscosities. The error in director field from the assumption that it is not influenced by the viscous flow is of the order of Er for the uniform flow field and of the order of the viscous term in the other cases. This method also assumes infinitely strong anchoring at the particle surface which we do not believe to be realistic.

Our third observation, relates to the diffusion coefficients of particles coated with single-component thiol monolayers. Past studies of macroscopic surfaces have established that monolayers formed from a single alkanethiol cause planar anchoring of LCs. Inspection of Figure 5-5 reveals two important conclusions. First, we observe that the mobilities of the gold nanoparticles with single-component thiol monolayers are significantly higher than the nanoparticles of the same size but with mixed thiol monolayers. This result is consistent with past observations reported by Koenig *et al*. (1), and confirms that the local, surface-induced ordering of the LC plays an important role in determining the particle mobility. Using the Stokes-Einstein equation we calculate that particles with the single component monolayer have a smaller apparent viscosity than the multicomponent monolayer. Finally, Figure 5-5 also reveals that there is no change in the apparent viscosity, and thus we infer local ordering of the LC about the nanoparticles as the size of the particle scales from 380±30 nm to 85±7 nm. We comment

here that theoretical predictions have not been performed for this geometry, and thus it is not possible to place our measurements in the context of theories, as is possible for the case of homeotropically anchored LC (as discussed above).

5.5 Discussion

We can interpret changes in apparent viscosity of a particle to be indicative of a modification in the local ordering of the LC near the particle surface. A change in the apparent viscosity of silica particles is observed as particle size decreases from 1.2±0.1 μm to 391±33 nm when functionalized with chemistries which give rise to perpendicular anchoring of the liquid crystal. However, no change in the apparent viscosity is measured for gold nanoparticles as size decreases from 380±30 nm to 85±7 nm for with either of the chemistries which give rise to either homeotropic or planar anchoring of the LC. We do note a change in apparent viscosity for nanoscale particles caused by changes in the surface chemistry that affects the surface anchoring of the liquid crystal which indicates that the rheological properties of the nanoparticles are influenced by surface chemistry. These results hint at a substantial change in the local ordering of the liquid crystal as size decreases from 1.2±0.1 μm to 391±33 nm.

Musevic and coworkers (3) have made similar observations with measurements of silica particles with a DMOAP monolayer ranging from 125 nm to 5 μm in diameter. Their results show that as the size of particles decreases from 5 μm to 500 nm, there is little change in the apparent viscosity of the particles in 5CB. In contrast to our own findings, below 500 nm there is no change in diffusion coefficient with respect to particle size. The apparent viscosities of these particles in 5CB are much higher than any of the Miezowitz shear viscosities; the largest of which is 129.6 mPa.s. Such results are not physically realizable and could be due to the presence of aggregates.

We also considered the possibility that optically induced near-surface electric fields influenced the LC ordering about the nanoparticle surfaces. As discussed in Chapter 4, gold nanoparticles exhibit near-surface electric fields when illuminated with certain wavelengths of

light. When illuminated with blue light, gold nanoparticles with diameters of 85±7 nm or 164±11 nm exhibited an increased hydrodynamic size of up to 54±12 nm relative to their physical diameter in the isotropic phase of LCs near the bulk transition temperature. However, under the same conditions but illuminated with red light, we observe that the gold nanoparticles had a hydrodynamic size consistent with their physical diameter. These observations support the proposition that near surface electric fields associated with the presence of hot electron-hole pairs formed an ordered solvent corona around the nanoparticle. We test the possibility that optically-induced electric fields affect the apparent viscosity of the 143±8 nm gold nanoparticles by performing particle tracking measurements with samples illuminated with different wavelengths of illumination. We track particles by placing red (650 nm (full width at half maximum (FWHM) = 40 nm)), green (550 nm (FWHM = 40 nm)), and blue (450 nm (FWHM = 40 nm)) band-pass filters in the light path of the microscope. Our observations are summarized in Figure 5-6. We observe no significant change in the apparent viscosity of 143±8 nm gold nanoparticles in nematic 5CB with different wavelengths of illumination of light. For gold particles functionalized with a mixed thiol monolayer, we measure apparent viscosities of the gold nanoparticles of 54.6±2.4 mPa.s, 53.9±1.8 mPa.s, and 53.2±1.7 mPa.s, for red, green, and blue illumination, respectively. Similarly, for gold particles functionalized with a single thiol monolayer, we measure apparent viscosities of the gold nanoparticles of 40.2±1.8 mPa.s, 39.9±1.8 mPa.s, and 40.9±1.0 mPa.s, for red, green, and blue illumination, respectively. We note that the measurements of apparent viscosity with the mixed thiol monolayer in Figure 5-6 differ significantly from those presented in Figure 5-5b. These measurements were performed with nanoparticles derived from two different stocks of both thiols and particles. The differences in

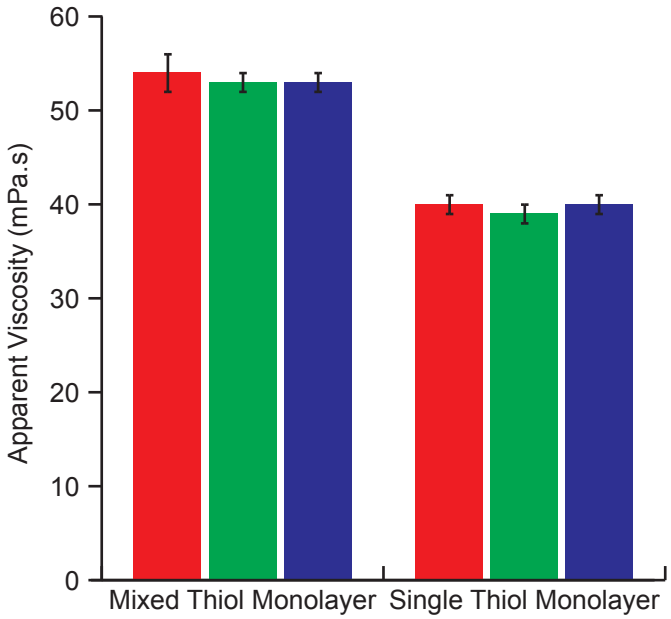


Figure 5 - 6. Apparent viscosity of 143±8 nm gold nanoparticles in nematic 5CB for diffusion perpendicular to the far-field director when illuminated with red (650 nm (FWHM = 40 nm)), green (550 nm (FWHM = 40 nm)), and blue (450 nm (FWHM = 40 nm)) light as indicated by the color of the bar.

the reported apparent viscosities of gold nanoparticles functionalized with mixed thiol monolayers could be caused to variations in their preparation which would lead to differences in the composition of the monolayers and anchoring energy of the LC at the particle surface. The mobilities of nanoparticles in a nematic LC medium are influenced by the anchoring energies of the LC at the particle surface (15).

5.6 References

1. Koenig GM, *et al.* (2009) Single Nanoparticle Tracking Reveals Influence of Chemical Functionality of Nanoparticles on Local Ordering of Liquid Crystals and Nanoparticle Diffusion Coefficients. *Nano Lett* 9(7):2794-2801.

2. Loudet JC, Hanusse P, & Poulin P (2004) Stokes drag on a sphere in a nematic liquid crystal. *Science* 306(5701):1525-1525.

3. Skarabot M & Musevic I (2010) Direct observation of interaction of nanoparticles in a nematic liquid crystal. *Soft Matter* 6(21):5476-5481.

4. Takahashi K, Ichikawa M, & Kimura Y (2008) Direct measurement of force between colloidal particles in a nematic liquid crystal. *J Phys-Condens Mat* 20(7).

5. Skarabot M, *et al.* (2006) Laser trapping of low refractive index colloids in a nematic liquid crystal. *Phys Rev E* 73(2).

6. Smalyukh II, Kachynski AV, Kuzmin AN, & Prasad PN (2006) Laser trapping in anisotropic fluids and polarization-control led particle dynamics. *P Natl Acad Sci USA* 103(48):18048-18053.

7. Kotar J, *et al.* (2006) Interparticle potential and drag coefficient in nematic colloids. *Phys Rev Lett* 96(20).

8. Ognysta U, *et al.* (2008) 2D interactions and binary crystals of dipolar and quadrupolar nematic colloids. *Phys Rev Lett* 100(21).

9. Stark H (2001) Physics of colloidal dispersions in nematic liquid crystals. *Phys Rep* 351(6):387-474.

10. Billeter JL & Pelcovits RA (2000) Defect configurations and dynamical behavior in a Gay-Berne nematic emulsion. *Phys Rev E* 62(1):711-717.

11. Ruhwandl RW & Terentjev EM (1997) Long-range forces and aggregation of colloid particles in a nematic liquid crystal. *Phys Rev E* 55(3):2958-2961.

12. Fukuda J, Stark H, & Yokoyama H (2005) Friction drag of a spherical particle in a liquid crystal above the isotropic-nematic transition. *Phys Rev E* 72(2).

13. Stark H & Ventzki D (2001) Stokes drag of spherical particles in a nematic environment at low Ericksen numbers. *Phys Rev E* 64(3).

14. Oldenburg SJ, Averitt RD, Westcott SL, & Halas NJ (1998) Nanoengineering of optical resonances. *Chem Phys Lett* 288(2-4):243-247.

15. Moreno-Razo JA, *et al.* (2011) Effects of anchoring strength on the diffusivity of nanoparticles in model liquid-crystalline fluids. *Soft Matter* 7(15):6828-6835.

Chapter 6

Conclusions and Closing Remarks

From the work described in this thesis, we draw several conclusions. In Chapter 3, we report on the mobilities of microparticles and nanoparticles at aqueous-liquid crystal (LC) interfaces. We measure the micrometer-sized particles to have mobilities at these interfaces that are significantly higher than mobilities in bulk LC. After giving consideration to both the location of the microparticles on the interface and the mobilities of the particles in the bulk LC, we conclude that the structure of the LC around the microparticles must be perturbed by the environment of the aqueous-LC interface. Significantly, and in contrast to our observations with micrometer-sized particles, the mobilities of nanometer-sized particles at the aqueous-LC interface did not differ significantly from the mobilities nanoparticles measured in bulk LC. The insensitivity of the mobilities of nanometer-sized particles to the interfacial environment is a property unique to the nanoparticles and not observed with the micrometer-sized particles.

In Chapter 4, we report on the mobilities of nanoparticles dispersed in isotropic solvents at temperatures close to those at which the solvent forms ordered phases. We demonstrate light-induced changes in the hydrodynamic sizes of gold nanoparticles under these conditions. Specifically, we measure 164±11 nm gold nanoparticles to have hydrodynamic diameters up to 54±12 nm larger than their physical diameters. By performing experiments designed to test several hypotheses, we determine that the light-induced changes in the hydrodynamic size of nanoparticles are due to the formation of an ordered solvent corona that is induced by interfacial electric fields associated with the presence of hot electron-hole pairs. Although the observations reported in Chapter 4 are of gold nanoparticles in the isotropic phases of mesogenic solvents, the mechanism that leads to the formation of interfacial electric fields associated with the generation

of hot electron-hole pairs suggests that our observations can be applied to a variety of systems. Specifically, the influence of interfacial electric fields on the solvent structure around the nanoparticles is not specific to mesogenic solvents and could be applied to the ordering of a variety of polar solvents. In addition, the mechanism for the generation of these interfacial electric fields – particularly the optical generation of hot electron-hole pairs – is not specific to gold nanoparticles. The generation of hot electron-hole pairs has been demonstrated in a variety of other materials including other metals and semiconductors (1, 2). We predict that the optical control of solvent structure can be achieved in a broad range of systems.

In Chapter 5, we report on the size dependent mobilities of micrometer-sized and nanometer-sized particles in bulk nematic LC. We make three observations. First, we measure the apparent viscosities of gold nanoparticles dispersed in nematic 5CB to be insensitive to the particle size over a range of diameters from 85±7 nm to 380±30 nm when functionalized with surface chemistries that give rise to either homeotropic or planar anchoring of the LC. This result indicates that there is no significant size-dependent change in the ordering of the LC around the nanoparticles. Second, in contrast, silica particles functionalized with chemistries which cause homeotropic anchoring of 5CB exhibit size-dependent apparent viscosities in nematic 5CB as the particle diameter decreases from 1.2 ± 0.1 μm to 391 ± 33 nm. The change in apparent viscosity observed over this size range indicates a size-dependent change in the ordering of the LC around the particles. These results indicate that the LCs structure differently around nanometer-sized particles and micrometer-sized particles. Specifically, there is a size-dependent change in the LC structure as their diameters decrease from 1.2 ± 0.1 μm to 391 ± 33 nm, however, no significant change in LC structure occurs as particle size decreases from 380 ± 30 nm to 85 ± 7 nm.

The work described in this thesis defines principles that permit control of the ordering of mesogenic solvents near the interfaces of particles. Several future directions of research can be envisaged. First, as noted above, we have demonstrated the optical control solvent structure around gold nanoparticles in mesogenic solvents in the isotropic phase. However, our results indicate that optical control of solvent structure could be achieved with a range of systems. Future studies could explore the generality of our findings using nanostructures composed of a range of metals and semiconductor materials dispersed in a range of polar solvents. Second, in this thesis, we measured changes in the structure of solvents around nanoparticles by measuring the mobility and optical properties of the particles. Measurement of the solvent structure can also be measured with other techniques such as by atomic force microscopy (AFM) (3) or by the surface force apparatus (4). Such measurements would also potentially provide additional insight into the structure of the interfacial layers induced by the hot electrons. Finally, we have demonstrated that the chemical functionality of nanoparticle surfaces influences their mobility in nematic LCs. The principles demonstrated by this study might be used in future studies involving devices designed to measure the hydrodynamic properties of the nanoparticles, as a way to test for the presence of targeted chemical species by selecting surfaces chemistries that change the anchoring of the LC in response to the presence of specific chemical analytes (5).

6.1 References

1. Knoesel E, Hotzel A, & Wolf M (1998) Ultrafast Dynamics of Hot Electrons and Holes in Copper: Excitation, Energy Relaxation, and Transport Effects. *Phys Rev B* 57(20):12812-12824.

2. Hayes JR, Levi AFJ, & Wiegmann W (1985) Hot-Electron Spectroscopy of GaAs. *Phys Rev Lett* 54(14):1570-1572.

3. Voitchovsky K (2013) Anharmonicity, Solvation Forces, and Resolution in Atomic Force Microscopy at the Solid-Liquid Interface. *Phys Rev E* 88(2):1-6.

4. Idziak SHJ*, et al.* (1994) The X-Ray Surface Forces Apparatus - Structure of a Thin Smectic Liquid-Crystal Film under Confinement. *Science* 264(5167):1915-1918.

5. Yang KL, Cadwell K, & Abbott NL (2005) Use of self-assembled monolayers, metal ions and smectic liquid crystals to detect organophosphonates. *Sensor Actuat B-Chem* 104(1):50-56.

Appendix A

Silica microparticles treated with dimethyloctadecyl[3-(trimethoxysilyl)propyl]ammonium chloride (DMOAP) to cause homeotropic anchoring of the LC.

Briefly, 5 mg of particles were (i) rinsed twice by diluting in 5 mL of water, centrifuging, and removing the supernatant; (ii) dispersed in 3 mL of 2 M sulfuric acid and sonicated for 30 min; (iii) centrifuged and redispersed in 5 mL of water twice and 2 mL of water once; (iv) stirred (for 25 mins) vigorously while adding 20 μL of DMOAP (60% in methanol); (v) centrifuged and re-dispersed in water four times and finally centrifuged and allowed to dry under vacuum overnight.

Appendix B

Precautions required to obtain reliable measurements of diffusion coefficients

Prior to reporting measurements of the mobilities of particles at the LC-aqueous interface, we comment that several precautions were found to be necessary in order to obtain reliable and reproducible measurements. First, we found it necessary to implement procedures that eliminated the effects of convection on the motion of the particles at the interface. In particular, we observed convection at the interface caused by the motion of the dipping objective. To avoid artifacts, following any motion of the objective, we found it necessary to wait several tens of minutes to allow the convection to dissipate. We also comment that LC interfaces can contain defects, and that defects can act as traps that arrest particle motion. Thus we measured the mobility of the particles in regions of the LC-aqueous interface that were observed optically to be free of defects. With this precaution, we did not observe particles to exhibit trajectories that were biased by interactions of the particles with defects on the interface